ISTANBUL TECHNICAL UNIVERSITY ★ GRADUATE SCHOOL

GRAPHENE CONDUCTIVE INKS FOR AN EFFECTIVE TEXTILE BASED RESPIRATORY SENSOR SYSTEM

M.Sc. THESIS

Kıvanç ÖZIŞIK

Department of Aeronautical and Astronautical Engineering

Aeronautical and Astronautical Engineering Programme

SEPTEMBER 2024

ISTANBUL TECHNICAL UNIVERSITY ★ GRADUATE SCHOOL

GRAPHENE CONDUCTIVE INKS FOR AN EFFECTIVE TEXTILE BASED RESPIRATORY SENSOR SYSTEM

M.Sc. THESIS

Kıvanç ÖZIŞIK
(511221117)

Department of Aeronautical and Astronautical Engineering

Aeronautical and Astronautical Engineering Programme

Thesis Advisor: Prof. Dr. Hülya CEBECİ

SEPTEMBER 2024

İSTANBUL TEKNİK ÜNİVERSİTESİ ★ LİSANSÜSTÜ EĞİTİM ENSTİTÜSÜ

TEKSTİL ESASLI SOLUNUM SENSÖR SİSTEMİ İÇİN GRAFEN İLETKEN MÜREKKEPLER

YÜKSEK LİSANS TEZİ

Kıvanç ÖZIŞIK
(511221117)

Uçak ve Uzay Mühendisliği Anabilim Dalı

Uçak ve Uzay Mühendisliği Programı

Tez Danışmanı: Prof. Dr. Hülya CEBECİ

EYLÜL 2024

Kıvanç ÖZIŞIK, a M.Sc. student of İTU Graduate School student ID 511221117 successfully defended the thesis entitled “GRAPHENE CONDUCTIVE INKS FOR AN EFFECTIVE TEXTILE BASED RESPIRATORY SENSOR SYSTEM”, which he prepared after fulfilling the requirements specified in the associated legislations, before the jury whose signatures are below.

Thesis Advisor :	**Prof. Dr. Hülya CEBECİ** Istanbul Technical University	.....
Jury Members :	**Asst. Prof. Dr. Kaan YILDIZ** Istanbul Technical University	.....
	Assoc. Prof. Dr. Elif Özden YENİGÜN Royal College of Art	.....

Date of Submission : 17 September 2024
Date of Defense : 18 September 2024

Ad astra, per aspera.

FOREWORD

I would like to express my deepest gratitude to Prof. Dr. Hülya CEBECİ for her unwavering support and patience throughout the completion of this work.

This thesis is part of a TUBITAK (Scientific and Technological Research Council of Türkiye) project, undertaken in collaboration with ITU ARC (Istanbul Technical University Aerospace Research Center), RCA (Royal College of Art), and Ertunç Özcan.

I am grateful to Versarien © and Dr. Stephen HODGE for providing the graphene ink and valuable discussions with Assoc. Prof. Elif ÖZDEN YENİGÜN (RCA) related to the material and systems. Having Prof. YENİGÜN as a jury member was also a great contribution to my study.

I also would like to thank to Assist. Prof. Kaan YILDIZ for his time, support and valuable comments on my study whenever I needed.

I am also immensely thankful to my esteemed colleagues, Dilan ARSLAN ÇATAK, for her support and invaluable contributions, and Melisa DİNÇER, for her cherished friendship during our work in our lab. Their existence was indispensable to the success of this research. My thanks extend to Dr. İpek ÖSKEN for her kindness and benevolence throughout this journey, which made a great positive impact.

I wish to convey my heartfelt appreciation to Zeynep ÖĞÜT and Ali ÖĞÜT for their invaluable support during the final phase of this project. A special acknowledgment goes to Loki the Cat.

I am truly grateful to my dear friend and former colleague, Ayşemin TOP, for her unwavering support. Reuniting after so long felt like stepping back in time to our earlier days together — such inspiration and energy!

Balancing this project with professional commitments was no small feat, and I am indebted to those who helped make it possible. I extend my gratitude to my former managers for their understanding and flexibility, as well as to the incredible Pegasus Powerplant Engineering Team of 2019/2024 — it has been an honor and privilege to work with you all.

My sincerest appreciation goes to my beloved cousin, Semih TUNÇ, whose assistance was instrumental in completing this work; without his support, this achievement would not have been possible.

My gratitude to my family, who have always been my unwavering source of support and encouragement.

Lastly, I would like to acknowledge myself a little for the perseverance and resilience I have shown over the years.

September 2024

Kıvanç ÖZIŞIK
(Aeronautical Engineer)

TABLE OF CONTENTS

Page

ABBREVIATIONS

2PP : 2 Point Probe
4PP : 4 Point Probe
AI : Artificial Intelligence
ANOVA : Analysis of Variance
CIJ : Continuous Inkjet
CV : Coefficient of Variation
DL : Deep Learning
DoD : Drop on Demand
ECG : Electrocardiogram
GF : Gauge Factor
GnP : Graphene Nanoplatelet
LVE : Linear Viscoelastic Region
ML : Machine Learning
PC : Personal Computer
PCB : Printed Circuit Board
PCR : Polymerase Chain Reaction
PDMS : Polydimethylsiloxane
RFID : Radio Frequency Identification
SEM : Scanning Electron Microscopy
TEM : Transmission Electron Microscopy
TFT : Thin Film Transistor
TPI : Thread Per Inch
UV : Ultraviolet
WSN : Wireless Sensor Networks

SYMBOLS

ρ	**:** Density
σ	**:** Shear stress
A	**:** Cross-sectional area
C	**:** Cutoff distance
d	**:** Distance between adjacent nanomaterials
e	**:** Single electron charge
G´	**:** Storage modulus
G´´	**:** Loss modulus
h	**:** Plank's constant
J	**:** Tunneling current density
k	: Kilo
L	**:** Length
m	**:** Mass of the electron
M	**:** Mega
Ω	**:** Ohm
Pa	**:** Pascal
R	**:** Resistance
t	**:** Thickness
V	**:** Electrical potential difference
µm	**:** Micrometer
v	**:** Poison's ratio

LIST OF TABLES

Page

LIST OF FIGURES

Page

GRAPHENE CONDUCTIVE INKS FOR AN EFFECTIVE TEXTILE BASED RESPIRATORY SENSOR SYSTEM

SUMMARY

This thesis provides an examination of the development and optimization of graphene-based conductive inks for textile-integrated respiratory sensors, addressing the critical and rising demand for seamless, non-invasive health monitoring solutions embedded within everyday garments. With the proliferation of wearable technology, especially following the COVID-19 pandemic, there is a heightened focus on integrating health monitoring systems into daily life without disrupting user comfort or activities. Positioned at the crossroads of material science, electronics, and healthcare innovation, this research has been performed to advance the wearable health monitoring field. Being part of the Scientific and Technological Research Council of Türkiye (TUBİTAK) project, which consists of several nano-inks, the primary aim of this research is to fabricate a reliable respiratory sensor system embedded within textiles, harnessing the superior electrical and mechanical properties of graphene.

Graphene, a material renowned for its outstanding conductivity, flexibility, and robustness, was chosen due to its unique ability to sustain consistent electrical performance under the repetitive stresses typical of wearable applications. These qualities make graphene particularly well-suited for applications requiring durable, comfortable, and inconspicuous health monitoring solutions, essential for prolonged, daily wear. Moreover, the focus on materials inherently compatible with textile substrates facilitates seamless integration into everyday clothing, enhancing the practicality and accessibility of these health-monitoring devices. The motivation behind this study is rooted in the growing need for unobtrusive, real-time health monitoring systems that eliminate the requirement for bulky, traditional equipment or uncomfortable skin contact sensors. Such devices are often cumbersome, especially in everyday scenarios, limiting their appeal and accessibility. By embedding sensors directly into textile substrates, this research aims to create a health monitoring solution that is as unobtrusive as possible. Such a development could pave the way for greater user compliance, as these wearable sensors are easily incorporated into garments and thus require minimal behavioral adjustments from the user.

The research methodology outlined in this thesis begins with the analysis of graphene-based conductive inks and extends through to their application on textile substrates, followed by a rigorous evaluation of sensor performance. The graphene inks used in this research were sourced from Versarien® and were manufactured through a microfluidization process, which was critical to achieving inks with consistent and controllable rheological properties. The selection and optimization of ink properties, such as viscosity and shear-thinning behavior, were central to this research, as these characteristics directly influence the ink's compatibility with textile printing practical techniques like screen printing. The rheological analysis allows for fine-tuning of the

ink’s properties, ensuring that the inks can be printed onto textiles efficiently without compromising the mechanical integrity of the fabric.

In the fabrication phase, graphene-based inks were applied to polyamide and cotton textile substrates, using screen printing. To optimize the screen-printing process, various mesh openings were tested for identifying the ideal conditions for achieving uniform and durable conductive patterns on the textile surfaces. A variety of printed patterns, including line, serpentine, strain gauge, and omnidirectional designs, were explored to assess the mechanical and electrical performance of the sensors under different conditions. Mechanical testing, in particular, was the cornerstone of this analysis, with samples subjected to extensive stretching and flexing to evaluate their durability and performance stability. This testing was essential in confirming that the sensors could withstand the demands of real-world use while maintaining conductivity and sensitivity. Electromechanical testing further underscored the effectiveness of these graphene-based inks in creating resilient, sensitive respiratory sensors for textiles. The sensors exhibited mechanical stability, consistently maintaining both sensitivity and conductivity even after repeated mechanical stresses. Such resilience is vital for wearable applications, where sensors must endure the rigors of daily life without failing or requiring frequent recalibration.

The research highlighted the critical role of rheological properties in determining the quality and functionality of the printed sensors, emphasizing the need for precise control over ink viscosity and deposition methods to achieve optimal performance. One of the most promising aspects of the developed sensors is their sensitivity to strain, which enables them to accurately monitor respiratory rates and detect irregular breathing patterns. This functionality is particularly valuable in medical applications, as it could provide early warnings of respiratory distress or other health issues that require immediate attention. The sensors generally demonstrated a linear response to changes in strain, allowing for reliable tracking of respiratory activity over time.

However, the thesis also identifies several technical challenges that must be addressed in future work. For instance, achieving precise alignment of the sensor patterns in relation to the textile fibers proved challenging, affecting the sensors' responsiveness to directional forces. Additionally, converting the fabricated sensors into testing specimens presented certain difficulties, especially when testing sensors with layered configurations.

The testing procedure involved both 4x5 and 5x5 layered sensors, each subjected to controlled strains of 5% and 10%. To investigate the effects of pre-strain and increase the robustness of the data, the testing protocol was adjusted in such a way that specimens initially intended for 5% strain measurements were subsequently tested at 10% strain and vice versa. The results showed that pre-straining the sensors generally had a beneficial impact on their performance, as the initial strain appeared to "settle" the sensor structure, yielding smoother and more consistent measurement patterns in subsequent tests. Furthermore, it has been understood that geometry and measurement area are intertwined with a trade-off between sensitivity and stability. For example, for applications that require high sensitivity, line geometry seems to be a suitable candidate. However, their consistency over time can be in question. In contrast, if a more stable and long-term measurement is required, strain gauge sensors might be a better solution. Serpentine and omnidirectional patterns proved both balanced sensitivity and stability, and they are more likely to be used in various areas of the body for respiration sensing.

TEKSTİL ESASLI SOLUNUM SENSÖR SİSTEMİ İÇİN GRAFEN İLETKEN MÜREKKEPLER

ÖZET

Bu tez, günlük giysilere entegre edilmiş, kesintisiz ve non-invaziv sağlık izleme çözümlerine yönelik kritik ve artan talebi ele alarak, tekstile entegre solunum sensörleri için grafen bazlı iletken mürekkeplerin geliştirilmesi ve optimizasyonunu derinlemesine incelemektedir. Özellikle COVID-19 pandemisinin ardından giyilebilir teknolojinin yaygınlaşmasıyla birlikte, sağlık izleme sistemlerinin kullanıcı konforunu veya aktivitelerini bozmadan günlük hayata entegre edilmesine yönelik artan bir odaklanma bulunmaktadır. Malzeme bilimi, elektronik ve sağlık inovasyonunun kesiştiği noktada konumlanan bu araştırma, giyilebilir sağlık izleme alanını ilerletmek amacıyla gerçekleştirilmiştir. Aynı kapsamda çeşitli nano-mürekkeplerden oluşan bir TÜBİTAK projesinin parçası olarak, bu araştırmanın birincil amacı, grafenin üstün elektriksel ve mekanik özelliklerinden yararlanarak tekstillere entegre edilmiş güvenilir bir solunum sensörü sistemi üretmektir.

Olağanüstü iletkenlik, esneklik ve dayanıklılığıyla tanınan grafen, giyilebilir uygulamalara özgü tekrarlanan stresler altında tutarlı elektriksel performansı sürdürebilme yeteneği nedeniyle seçilmiştir. Bu özellikler, grafeni uzun süreli günlük kullanım için gerekli olan dayanıklı, konforlu ve fark edilmeyen sağlık izleme çözümleri gerektiren uygulamalar için özellikle uygun kılmaktadır. Ayrıca, tekstil alt tabakalarıyla doğrudan uyumlu malzemelere odaklanmak, bu sağlık izleme cihazlarının günlük kıyafetlere sorunsuz bir şekilde entegre edilmesini kolaylaştırarak pratiklik ve erişilebilirliği artırmaktadır. Bu çalışmanın motivasyonu, hantal, geleneksel ekipman veya rahatsız edici cilt temaslı sensörlere olan ihtiyacı ortadan kaldıran, göze çarpmayan, gerçek zamanlı sağlık izleme sistemlerine yönelik artan ihtiyaca dayanmaktadır. Böyle cihazlar, özellikle günlük senaryolarda hantal olabilmekte ve çekicilik ve erişilebilirliklerini sınırlamaktadır. Sensörleri doğrudan tekstil alt tabakalarına entegre ederek, bu araştırma mümkün olduğunca göze çarpmayan bir sağlık izleme çözümü yaratmayı hedeflemektedir. Böyle bir gelişme, bu giyilebilir sensörler giysilere kolayca entegre edildiğinden ve kullanıcıdan minimum davranışsal ayarlama gerektirdiğinden, daha büyük kullanıcı uyumu için zemin hazırlayabilir.

Bu tezde açıklanan araştırma metodolojisi, grafen bazlı iletken mürekkeplerin analizinden başlayıp tekstil alt tabakalarına uygulamalarına ve ardından sensör performansının titiz bir şekilde değerlendirilmesine kadar uzanmaktadır. Bu araştırmada kullanılan grafen mürekkepleri Versarien® firmasından temin edilmiş ve mikrofluidizasyon süreciyle üretilmiştir; bu süreç, tutarlı ve kontrol edilebilir reolojik özelliklere sahip mürekkepler elde etmek için kritik öneme sahiptir. Viskozite ve kayma incelmesi davranışı gibi mürekkep özelliklerinin seçimi ve optimizasyonu, bu araştırmanın merkezinde yer almıştır; çünkü bu özellikler, mürekkebin serigrafi gibi tekstil baskı teknikleriyle uyumluluğunu doğrudan etkilemektedir. Reolojik analiz,

mürekkebin özelliklerinin ince ayarlanmasına olanak tanıyarak, mürekkeplerin kumaşın mekanik bütünlüğünü bozmadan tekstillere verimli bir şekilde basılmasını sağlamaktadır.

Üretim aşamasında, grafen bazlı mürekkepler poliamid ve pamuklu tekstil alt tabakalarına serigrafi kullanılarak uygulanmıştır. Serigrafi işlemini optimize etmek için, tekstil yüzeylerinde düzgün ve dayanıklı iletken desenler elde etmek amacıyla çeşitli ağ açıklıkları test edilmiştir. Sensörlerin farklı koşullar altında mekanik ve elektriksel performansını değerlendirmek için çizgi, serpantin, gerinim ölçer ve çok yönlü tasarımlar dahil olmak üzere çeşitli baskılı desenler araştırılmıştır. Özellikle mekanik testler, bu analizin temel taşı olmuştur; örnekler dayanıklılıklarını ve performans istikrarlarını değerlendirmek için kapsamlı gerilme ve bükülmeye tabi tutulmuştur. Bu testler, sensörlerin gerçek dünya kullanımının taleplerine dayanırken iletkenliği ve duyarlılığı koruyabildiğini doğrulamak için esastır. Elektromekanik testler, grafen bazlı bu mürekkeplerin tekstiller için dayanıklı ve hassas solunum sensörleri yaratmadaki etkinliğini daha da vurgulamıştır. Sensörler, tekrarlanan mekanik streslere rağmen hem duyarlılığı hem de iletkenliği tutarlı bir şekilde koruyarak mekanik istikrar sergilemiştir. Böyle bir dayanıklılık, sensörlerin günlük yaşamın zorluklarına dayanması ve arızalanmaması veya sık sık yeniden kalibre edilmesi gerekmeyen giyilebilir uygulamalar için hayati öneme sahiptir.

Araştırma, baskılı sensörlerin kalite ve işlevselliğini belirlemede reolojik özelliklerin kritik rolünü vurgulayarak, optimal performansa ulaşmak için mürekkep viskozitesi ve biriktirme yöntemleri üzerinde hassas kontrol ihtiyacını ortaya koymuştur. Geliştirilen sensörlerin en umut verici yönlerinden biri, gerinime duyarlılıklarıdır; bu da onların solunum hızlarını doğru bir şekilde izlemelerini ve düzensiz solunum modellerini tespit etmelerini sağlar. Bu işlevsellik, solunum sıkıntısı veya acil dikkat gerektiren diğer sağlık sorunlarının erken uyarılarını sağlayabileceğinden tıbbi uygulamalarda özellikle değerlidir. Sensörler genellikle gerinimdeki değişikliklere lineer bir yanıt göstermiş, zaman içinde solunum aktivitesinin güvenilir bir şekilde izlenmesine olanak tanımıştır.

Bununla birlikte, tez ayrıca gelecekteki çalışmalarda ele alınması gereken birkaç teknik zorluğu da belirlemektedir. Örneğin, sensör desenlerinin tekstil liflerine göre hassas hizalanması zorlayıcı olmuş ve sensörlerin yönlü kuvvetlere olan tepkisini etkilemiştir. Ayrıca, üretilen sensörlerin test numunelerine dönüştürülmesi, özellikle katmanlı konfigürasyonlara sahip sensörlerin test edilmesinde belirli zorluklar sunmuştur.

Test prosedürü, farklı gerinim seviyelerinde sensör performansını değerlendirmek amacıyla, %5 ve %10 kontrollü gerinimlere tabi tutulan 4 ve 5 katmanlı sensörlerin sistematik bir şekilde incelenmesini içermiştir. Bu prosedür kapsamında, ön gerinim etkilerini daha iyi anlamak ve elde edilen verilerin sağlamlığını artırmak için, başlangıçta %5 gerinim ölçümleri için tasarlanan numuneler daha sonra %10 gerinim koşullarında test edilmiş ve benzer şekilde, %10 gerinim ölçümleri için ayrılan numuneler de %5 gerinimde değerlendirilmiştir. Bu çift yönlü test yöntemi, sensörlerin mekanik stabilitelerini ve tekrarlanan yüklemelere verdikleri tepkileri detaylı bir şekilde analiz etmeye olanak tanımıştır.

Sonuçlar, ön gerinim uygulanmasının sensör performansı üzerinde genellikle olumlu bir etki yarattığını göstermiştir. İlk gerinimin sensör yapısını "düzenlediği", yani iç yapıyı stabilize ettiği ve bunun sonucunda sonraki testlerde daha düzgün ve tutarlı ölçüm desenleri elde edildiği görülmüştür. Bu durum, sensörlerin gerinim altında nasıl

davrandıklarına dair önemli bilgiler sağlamış ve üretim süreçlerinde olası iyileştirmeler için ipuçları sunmuştur.

Bununla birlikte, geometrinin ve ölçüm alanının sensör duyarlılığı ve istikrarı üzerinde önemli bir rol oynadığı belirlenmiştir. Yüksek duyarlılık gerektiren uygulamalarda, çizgi geometrisi dikkat çekici bir aday olarak öne çıkmıştır. Ancak, bu geometrinin zaman içerisindeki tutarlılığı sorgulanabilir bulunmuş, bu da uzun vadeli kullanımlar için sınırlamalar olabileceğini düşündürmüştür. Öte yandan, daha istikrarlı ve uzun vadeli ölçümler gerektiren uygulamalarda, gerinim ölçer sensörlerin daha uygun bir çözüm sunduğu tespit edilmiştir.

Serpantin ve çok yönlü desenler, hem duyarlılık hem de istikrar açısından dengeli sonuçlar vermiştir. Bu geometriler, özellikle vücudun farklı bölgelerinde solunum algılama gibi çok yönlü hassasiyet gerektiren durumlarda daha elverişli bir kullanım potansiyeline sahiptir. Serpantin deseninin esnek yapısı, geniş bir gerinim aralığında güvenilir ölçümler sağlayabilirken, çok yönlü desenlerin karmaşık kuvvet dağılımlarını algılama yeteneği, bu geometriyi ileri düzey uygulamalar için cazip bir seçenek haline getirmiştir.

Sonuç olarak, bu çalışmada test edilen sensörlerin performans analizleri, farklı geometrilerin belirli uygulamalarda nasıl avantajlar sunduğunu ve bu avantajların kullanıma bağlı olarak nasıl şekillendiğini göstermiştir. Bu bulgular, hem mevcut sensör tasarımlarını optimize etmek hem de gelecekteki uygulamalar için daha sağlam ve duyarlı çözümler geliştirmek adına değerli bir temel sağlamaktadır.

1. INTRODUCTION AND LITERATURE REVIEW

1.1 Prologue

Since the beginning of COVID-19 pandemic [1], SARS-CoV-2 (severe acute respiratory syndrome – Coronavirus – 2) casualties dramatically increased due to severe lung damage, especially for the people who had pre-existing conditions [2]. At that time, all health facilities struggled to deal with the virus and often emphasized the need for more space, equipment, knowledge, and workforce. In another perspective, we all needed the means for diagnosis and health monitoring, with accessibility features, simplicity and accuracy. Despite the numerous challenges, the situation was not entirely without hope. Amongst the coping methods, the nasopharyngeal polymerase chain reaction (PCR) test was a critical and accessible one, albeit its sensitivity was in question [3]. While the number of health facilities could have been considered adequate, it had been observed that many health centers are experiencing significant challenges due to insufficient equipment [4] and imbalanced workloads [5]; particularly in response to the escalating demands brought about by the pandemic. Moreover, some of the equipment required complex set-up procedures and therefore not suitable for transportation, also required trained personnel. Last but not least, post treatment morbidity and mortality prevailed, advising close-up monitoring for comprehensive care [6], [7], [8], unfortunately. All of these events and conditions indicated the necessity and effectivity of point of care and/or point of use devices for precise and rapid data acquisition [9]. While the reasons previously mentioned provide sufficient justification for action, the practice of streamlining health monitoring is not a novel concept. Myriad of applications and studies exist and continue to grow; such as wearable sensors (Figure 1.2), lab/organ/body-on-a-chip (Figure 1.1), paper based analytical devices [10] and so on.

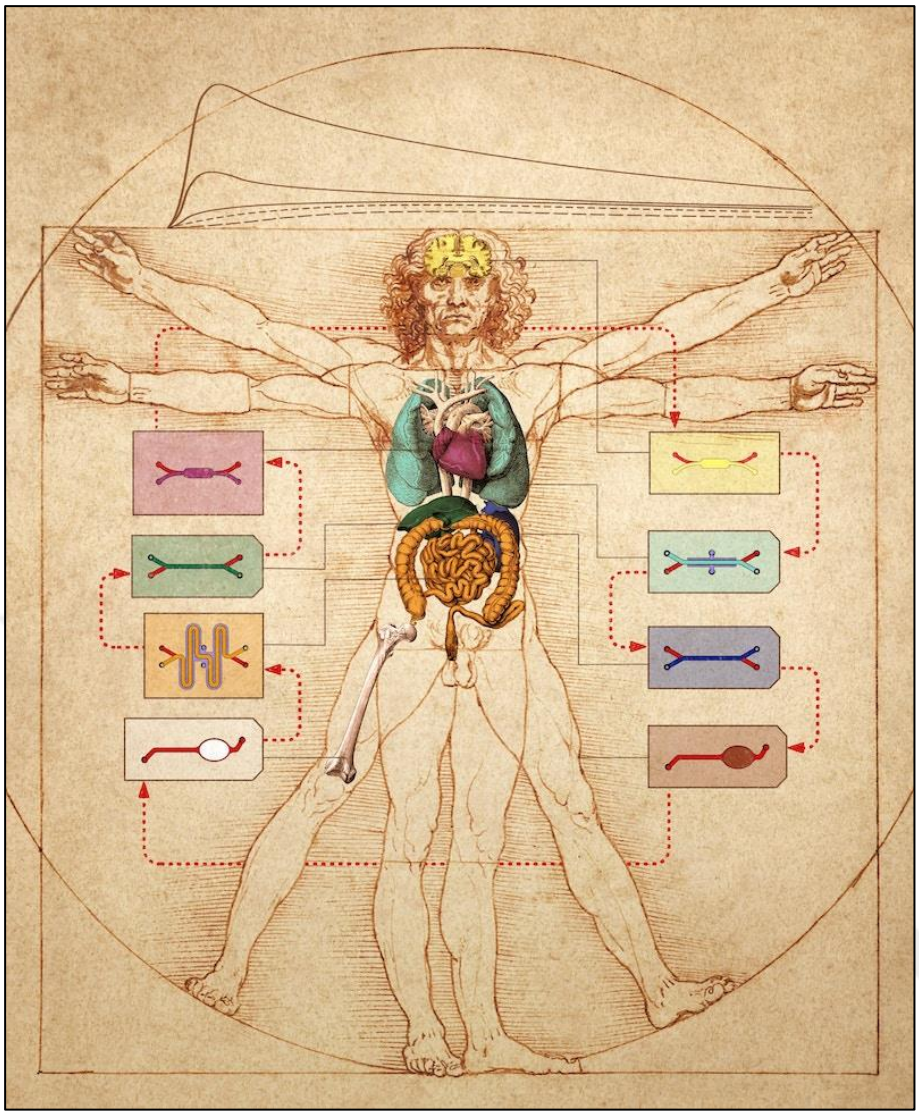

Figure 1.1 : Body-on-a-chip layered system illustrated on the infamous ink-drawed work called Vitruvian Man by Leonardo Da Vinci. (Adapted from Wyss Institute from Harvard University study [11]).

Applications of continuous health monitoring can be categorized into two areas: directed towards the individuals who do not have or have limited background in biology or medicine, for practical purposes (Figure 1.2 a), and as medical, requiring professional education (Figure 1.2 b). Over time, these devices' capabilities dramatically increased. Nowadays, especially the first type is rapidly closing the gap with professional ones [12], [13], [14], [15], [17].

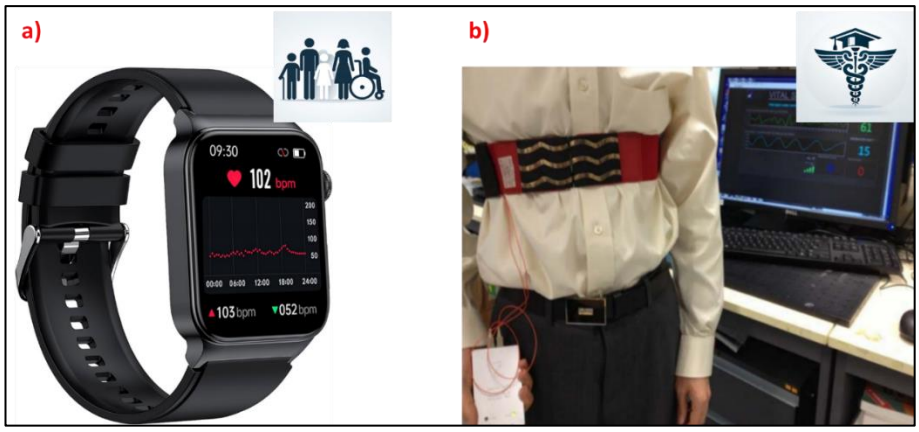

Figure 1.2 : a) Smartwatch image for daily usage with minimum experience, b) fiberoptic sensor requiring more experience and/or training to use (adapted from [18]).

1.2 Respiration Monitoring and Wearable Sensors

Given the fundamental necessity of respiration for sustaining life, research that contributes to a deeper understanding and improved monitoring of breathing patterns holds significant value [19]. Continuous respiration monitoring can greatly aid people with conditions such as sudden infant death syndrome [20], cardiac arrest [21], sleep apnea [22] or can provide vital information about a person's overall well-being, such as measuring the stress levels [23], psychological disorders [24] and elderly care [18]. Amongst these works such as extracting the respiratory rate from an electrocardiogram (ECG) conducted by Orphanidou, C. in 2017 [25], chest impedance by Grenvik, A. et. al in 1972 [26] or a real-time vision-based respiration monitoring by K. S. Tan et. al. in 2010 [27] were studied. In addition, CO_2 variation was measured to track the respiratory system, which was also conducted by Umeda A. et.al in 2021 [28].

Wearable technologies embody substantial potential owing to their expansive applications across various domains [29], [30]. These include, but are not limited to, soft robotics, integration of electronic components into clothing, advancement of intelligent textiles, development of inductive materials for medical applications, and creation of tools for health monitoring [31]. This broad applicability underscores the transformative potential of wearable technologies in these fields [32].

Wearable sensory systems can be defined as apparatuses that can be directly used on the skin [33], [34]. A typical example is smart watches, which are extensively used for obtaining information such as pulse rate, oxygen level monitoring, sleep quality, basically about the user's overall well-being. Another example is continuous blood

glucose monitoring patches. Even though studied in the past, current studies of statistical algorithms such as machine learning (ML) and deep learning (DL) also regained their utility due to advancements in technology [35], [36]. For example, radiological data became digitally interpretable via image processing and machine learning algorithms [37], [38]. Another innovative approach, using graphene textile sensors, is the creation of a silent speech interface where both materials crack mechanism and signal processing are used in harmony with the aid of artificial intelligence (AI) [39]. As a result, a massive potential for portable health data acquisition for swift and accurate health monitoring is revealed, which can provide insight for users to either prevent any severe sickness or increase wellbeing. What is more, these technologies can also be used for personalized medicine for humans [40], [41], [42], [43], [44] or for animals [45].

1.3 Sustainability and Environmental Aspects

Another point in wearable and portable devices is that they come in many shapes and forms, primarily dependent on batteries and printed circuit boards (PCBs). For such demanding technologies, waste production and energy consumption management became a challenge, calling for more eco-friendly processes [46], [47], [31], [48]. Therefore, it is crucial to develop designs with critical sustainability figures such as recyclability, low CO_2 emissions during fabrication, reusability etc. Amongst the desired properties in such devices and methods, being non-invasive, lightweight, comfortable, flexible, bio-compatible, and sustainable are well known. Eventually, a significant amount of research gave design criteria such as ASSURED [49] which is now also rephrased as REASSURED [50], where details are given in APPENDIX B, Table B.1.

1.4 Aim of the Study

Graphene, a two-dimensional carbon material, is known for its excellent electronic and mechanical properties. Its high conductivity makes it ideal for fabricating conducting tracks, while its other unique attributes could optimize energy storage and conversion devices, potentially increasing energy density and efficiency. Moreover, graphene's inherent strength and flexibility offer potential for resilient actuators and advancements in catalysis, underscoring its diverse potential applications [51], [52],

[53], [54], [55]. Since graphene is naturally abundant in the form of graphite, it also presents an economical alternative for addressing the aforementioned challenges.

Along with many applications of wearable health tracking devices such as temperature sensors, strain sensors etc. [34], wearable textile strain sensors fabricated with conductive inks covering the design and performance criteria mentioned previously with a focus on respiration are the interest of this study. Subsequent sections will elaborate on technical details about strain sensors, the importance of sensing performance, conductive inks, and the effect of rheological properties along with printing methods. Later, the materials and methods will be detailed with results and discussions. Finally, conclusions and future studies/recommendations are going to be presented.

1.5 Strain Sensors

Strain sensors transform physical deformations into quantifiable signals [56]. Textile wearable sensors generally differ by combining two elements: an elastomer substrate and a percolating network of conductive material over the substrate [57].

It has been estimated that the human breathing pattern is similar to 5% to 10% of strain via expansion of the chest [58]. Therefore, the exact strain levels are studied. Amongst these studies, it has been demonstrated that on higher levels of strains, effects of brittleness took place; micro-cracks and discontinuities between conductive paths were observed [44].

Overall sensor performance is measured by its sensitivity/gauge factor (GF) given below:

$$GF = \frac{\Delta R - R_0}{\varepsilon} \tag{1.1}$$

Where, ΔR means resistance change, R_0 means initial resistance (resistance in 0% strain) and ε indicates the strain amount.

1.5.1 Sensing mechanisms

Visualizing the movement of electrons between graphene layers and from the point of initiation to the terminal end poses a significant challenge. Fabricated strain sensor consists of a complex three-dimensional conductive pathway formed by graphene ink. This ink is layered and adhered to the textile, which is the insulating substrate. The

arrangement of graphene flakes within the ink is inherently unique for each sensor produced. Furthermore, this arrangement evolves with the application of strain, leading to distinct electrical properties for each sensor instance in operation. These dynamic alterations underscore the complexity of predicting electron movement and sensor performance in such systems. The continuity of the current can be established via connecting networks. The percolation theory also explains this. As depicted in Figure 1.3, a differential element of the substrate in resting conditions where conductive graphene flakes are closer changes during stretching, leading to gaps and giving rise to divergent flake configurations, altering the sensing mechanisms with a generally non-linear resistance change.

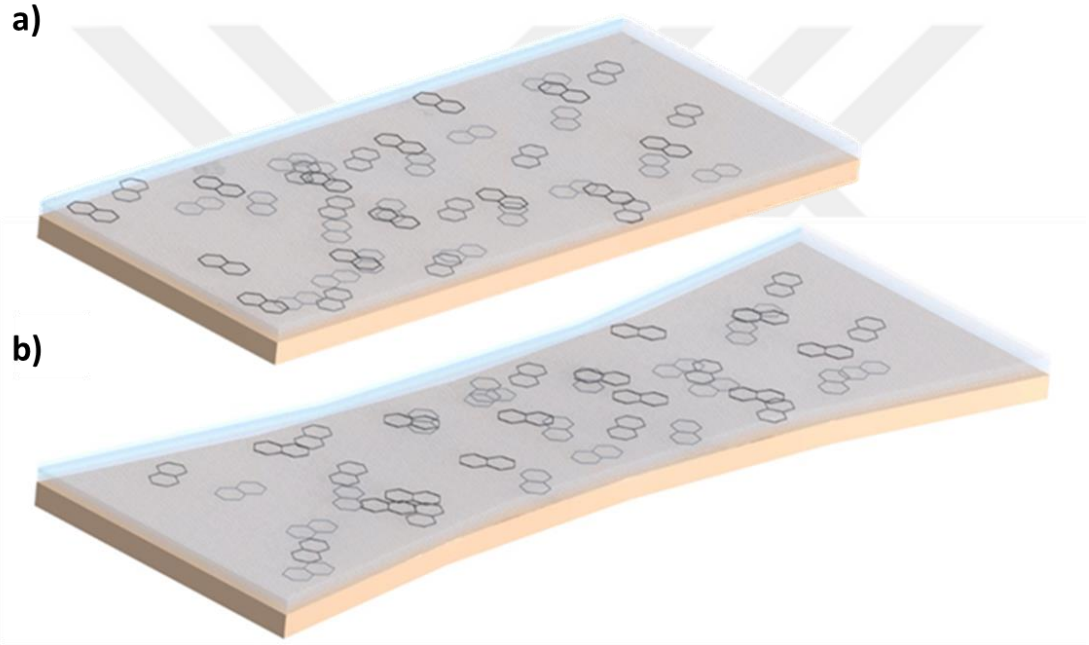

Figure 1.3 : Image of filler composure in a differential substrate element, suspended in layers; a) at resting condition and b) during stretching.

The following sections explain the performance parameters of the strain sensors. Hui Chen et al. review the sensing mechanism and main parameters affecting these mechanisms [55]; categorizing as conventional, which has geometrical and piezoresistive aspects, and adding tunneling effect as a new sensing mechanism.

1.5.1.1 Geometrical effect

Denoted as below, the typical resistance change behavior where L, length is linearly correlated with the resistance and cross-section, A is inversely related. Upon stretching L would increase and the material would shrink in the transverse direction to the

applied force per the Poisson's ratio v. Hence, *A* would decrease. In this model, resistivity is assumed constant. Studies suggest that sensor performance and its length are correlated [59].

$$R = \rho \frac{L}{A} \tag{1.2}$$

While this effect is seemingly linear and straightforward, it is found that the case is not the same for carbon-based materials, attributed to the saturation effect as shown in Figure 1.4 [60] .

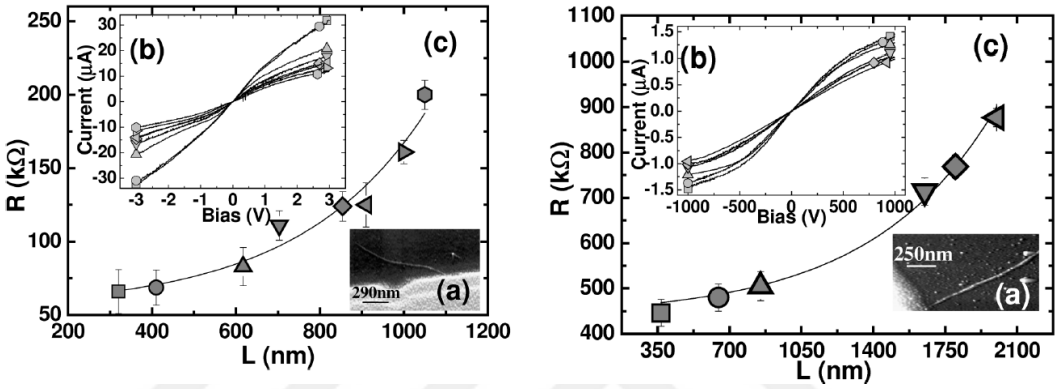

Figure 1.4 : Nonlinear relationship between length and resistance for SWCNTs (adapted from [60]).

1.5.1.2 Piezoresistive effect

The effect of piezoresistivity in germanium and silicon was discovered by C.S. Smith in 1954 [61]. It was found that the resistance of a germanium or silicon filament changed when the material was stressed. The effect of piezoresistivity is similar to the strain gauge effect in a metal material, but the differences between them are quite fundamental and particularly summarized as:

(a) The effect of metal strain gauge is caused by the geometric deformation of the resistor, whereas piezoresistivity is caused by the change of resistivity of the material,

(b) The effect of metal strain gauge is isotropic, whereas the effect of piezoresistivity is generally anisotropic, and

(c) The effect of piezoresistivity can be two orders of magnitude larger than that of the metal strain gauge effect [62].

Resistance model of the piezoresistive effect is formulated as follows:

$$\frac{\Delta R}{R} = (1 + 2v) + \frac{\Delta \rho}{\rho} \quad (1.3)$$

1.5.1.3 Disconnection mechanism

A disconnection mechanism exists in a conductive network mainly due to the separation of overlapped nanomaterials, which move apart from each other upon stretching and re-connecting upon the release of the strain. Generally, in small strain levels (<125%), the disconnection mechanism does not play a significant role as overlapping; hence percolation still exists [63]. Therefore, while effective, it is not considered a dominant contributor to small strain levels.

1.5.1.4 Crack propagation

When sensing materials, such as brittle thin films, are applied to a textile-based substrate, the mechanical property mismatch between the two components can cause the sensing layer to crack during deformation. This mismatch leads to the formation and propagation of cracks under stretching conditions. As microcracks open and expand, the conductive paths significantly diminish, increasing electrical resistance. This phenomenon can also be utilized for strain-sensing applications. Although crack formation results in significant variations in the sensing response and high sensitivity (gauge factor), it generally leads to a limited sensing range, hysteresis, non-linear sensing behavior, and low cyclic stability [64]. Increasing the thickness of the sensing layer, achieved by applying additional layers, is reported as detrimental to the stability of the sensing response because of the uneven formation of microcracks [65].

1.5.1.5 Tunneling effect

The tunneling effect refers to the transmission of electrons through a non-conductive barrier. This phenomenon is a fundamental concept in quantum physics. Within a cutoff distance between the nano materials (shown as c in Figure 1.5 below), electrons can be transmitted. Tunneling resistance can be estimated by Simmon's principle:

$$R_{tunnel} = \frac{V}{AJ} = \frac{h^2 d}{Ae^2 \sqrt{2m\lambda}} \exp\left(\frac{4\pi d}{h}\sqrt{2m\lambda}\right) \quad (1.4)$$

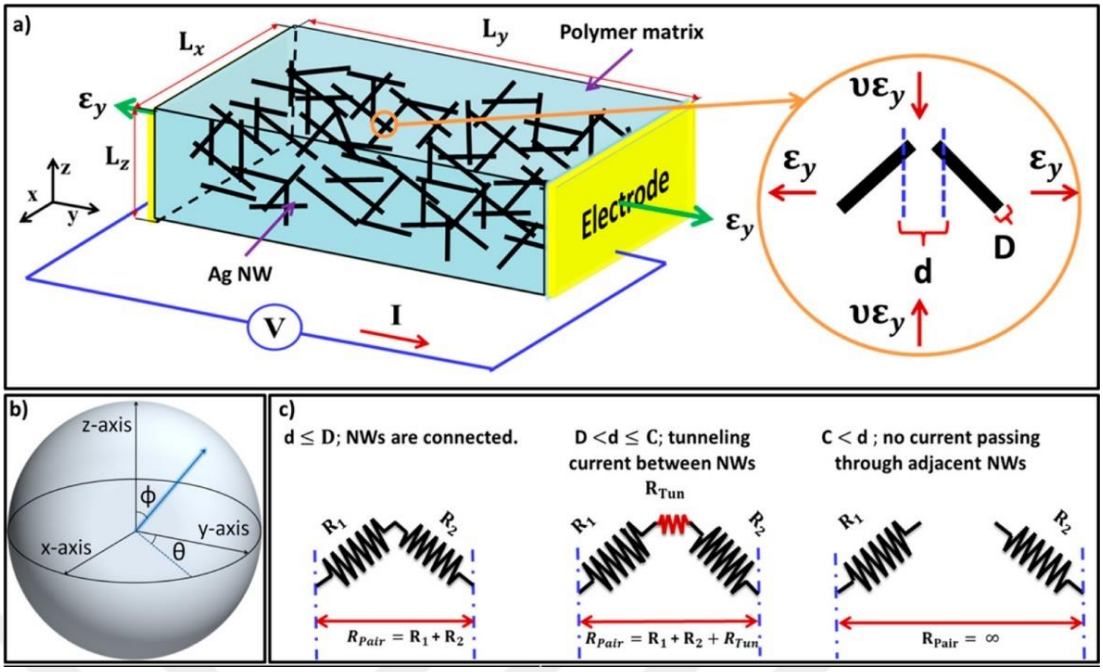

Figure 1.5 : Demonstration of tunneling effect (adapted from [66]).

In this context, V represents the electrical potential difference, A denotes the cross-sectional area of the tunneling junction, J signifies the tunneling current density, e is the charge of a single electron, m refers to the electron's mass, λ indicates the height of the energy barrier for polymers, h is Planck's constant, and d describes the distance between adjacent nanomaterials. The cutoff distance C for graphene flakes is noted to be between 2 and 3 nm [67], [68].

1.6 Conductive Inks

Conductive inks are specialized formulations facilitating electronic components and circuit fabrication through various printing techniques. These inks typically consist of conductive materials, such as silver (Ag), copper (Cu), carbon-based materials like carbon nanotubes (CNTs) or graphene, dispersed within a liquid polymer matrix [69], [70], [71] . The matrix typically has a binder agent for aggregation of the conductive materials and a solvent to suspend the rest of the components [9], and this dispersion enables the application of conductive inks using various printing methods, including screen printing, inkjet printing, and aerosol jet printing. The primary advantage of conductive inks lies in their ability to create flexible electronics, as they can be printed on flexible substrates like paper, plastic, or textiles. As the technology matures, conductive inks are becoming more efficient, cost-effective, and environmentally

friendly, offering a sustainable alternative to conventional electronic manufacturing practices.

Table 1.1 : Ink types and advantages vs disadvantages.

Group	Ink Type	Advantages	Drawbacks
Metal	**Silver-based**	- High conductivity - Stable in various environmental conditions - Ideal for high-frequency applications	- Expensive - Prone to oxidation without passivation layers
	Copper-based	- Lower cost compared to silver - Good conductivity -Widely available.	- Less stable in air compared to silver
Carbon	**CNT based**	- Economical - Flexible -Environmentally friendly - Resistant to oxidation	- Lower conductivity compared to metal-based inks - Not suitable for high-frequency applications
	Graphene-based	- Highly flexible - Transparent (for certain applications) - Good conductivity	- Challenging to produce in large quantities - Expensive manufacturing processes
Other	**Polymer-based**	- Flexible - Printable on various substrates - Can combine conductivity with other properties (e.g., flexibility)	- Lower conductivity compared to metal-based inks. - Often require additional curing steps

Conductive ink formulations vary significantly in their properties, offering distinct advantages and limitations depending on their material composition. Silver-based inks, which employ silver nanoparticles (AgNPs), are renowned for their superior electrical conductivity, chemical stability, and robust resistance to oxidation, making them highly suitable for high-performance flexible and stretchable electronics. However, the necessity for high-temperature sintering to achieve optimal conductivity significantly limits their applicability in low-temperature processes [72]. Copper-based inks, utilizing copper nanoparticles (CuNPs), offer a more cost-effective

alternative to silver due to their lower material costs while maintaining good electrical conductivity. Despite these benefits, copper's tendency to oxidize under heat and humidity poses challenges, such as the need for protective coatings and higher annealing temperatures [9], [73].

Carbon-based inks, particularly those incorporating CNTs, are promising for printed and flexible electronics due to their favorable electrical properties, cost-effectiveness, and environmental benefits. Nonetheless, the stability of CNT dispersions, exacerbated by van der Waals forces, along with concerns over their toxicological impact, restricts their broader application in wearable technology [72], [74]. Graphene-based inks are highly regarded for their exceptional mechanical flexibility, high electrical conductivity, and chemical stability, making them ideal for advanced flexible electronics. However, their practical application faces several challenges. These include achieving consistent conductivity, ensuring proper adhesion to substrates, managing the high annealing temperatures required, and maintaining stable dispersions[75]. Atomic formations of the carbon atom are given in Figure 1.6.

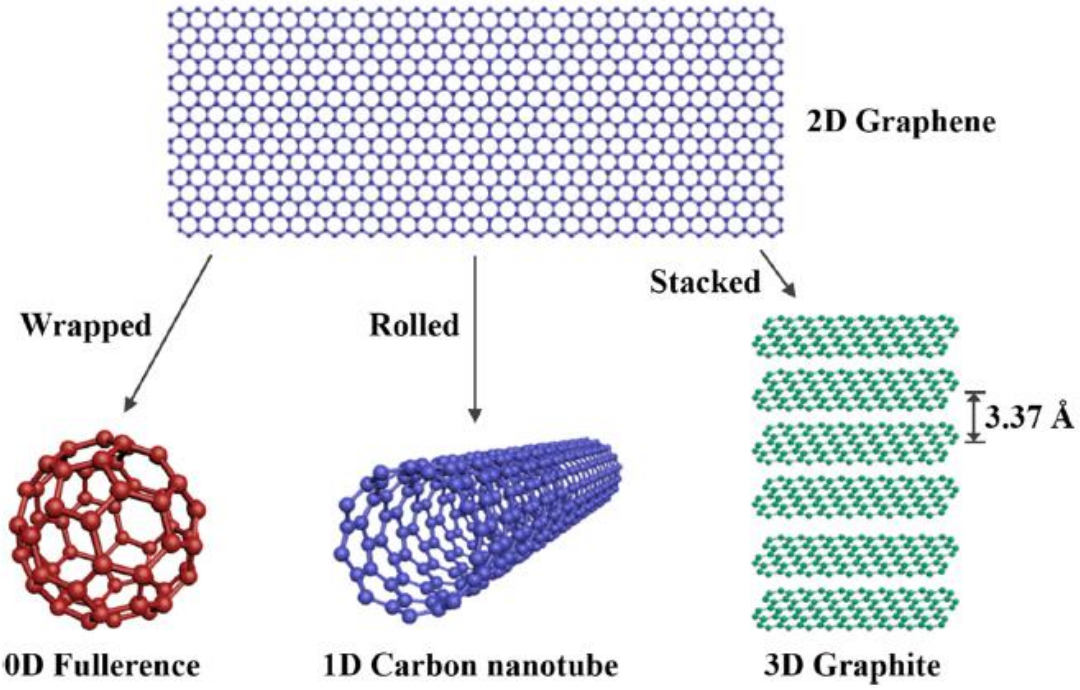

Figure 1.6 : Form of carbon atoms in different dimensions (adapted from [76]).

Polymer-based inks, incorporating materials such as Poly (3,4-ethylenedioxythiophene) called as PEDOT and Polyaniline (PANI), are valued for their flexibility, ease of processing, and low cost. These inks do not require high-temperature annealing, making them suitable for applications involving low-

temperature substrates. However, their relatively low electrical conductivity compared to metal-based inks limits their effectiveness in applications that demand high-performance levels [9], [72], [74]. It is often mentioned that metal-based conductive inks have superior conductivity; however, this comes at the expense of cost and biocompatibility [9] . In addition, it is mentioned that this type of conductive ink is not as stable compared to carbon-based inks, as they are more prone to oxidation [77] and aggregation [78] [9]. Throughout the literature, the most commonly used carbon nanomaterials in conductive ink studies include graphite powder, carbon black, graphene, and carbon nanotubes. First theorized by Wallace [79], graphene was clearly identified and produced by Novoselov and Geim [80]. The method involved exfoliation by repeated peeling, where a flake of graphite is placed in the middle of scotch tape and repeatedly folded and unfolded until a transparent layer of graphite remains, which is then transferred onto a silicon wafer. Observing this wafer under an optical microscope reveals areas where single or multilayered graphene potentially exists.

Graphene possesses four valence electrons, three of which form strong bonds with neighboring atoms. In graphite, while the 2D layer or plane is strongly bonded, the layers in the transverse direction are bonded by weak van der Waals forces. In nature, almost all bonds break the 2D symmetry and form a 3D structure. What makes graphene unique is its ability to exist in a 2D form in the ground state, which is attributed to sp^2 hybridization.

1.6.1 Rheology of carbon-based inks

Achieving high-quality printed patterns using carbon based such as graphene conductive inks in screen printing requires rheological analysis. Graphene's remarkable properties in advanced electronics demand control over ink formulation to optimize printing performance.

Another aspect of successful screen printing is the ink's viscosity and flow characteristics. These properties ensure the ink's smooth passage through the screen mesh, allowing for the creation of precise and fine conductive tracks. Proper rheological tuning aids in avoiding issues like clogging or extensive wetting, which can impair pattern definition.

A critical aspect of rheological optimization involves understanding the ink's shear-thinning behavior, where the viscosity of the ink decreases as shear stress increases. This property enables the ink to reduce viscosity under the shear stress induced by the squeegee's movement, facilitating smooth flow through the screen. Once the stress is removed, the ink rapidly regains its original viscosity, forming stable and well-defined patterns. This complete cycle can be also named as thixotropic behavior [81], [82], [83], which plays a crucial role in maintaining consistent printing quality. This property ensures that the ink preserves its optimal flow characteristics under sustained shear conditions. Such consistency is essential for achieving uniformity in the final printed products.

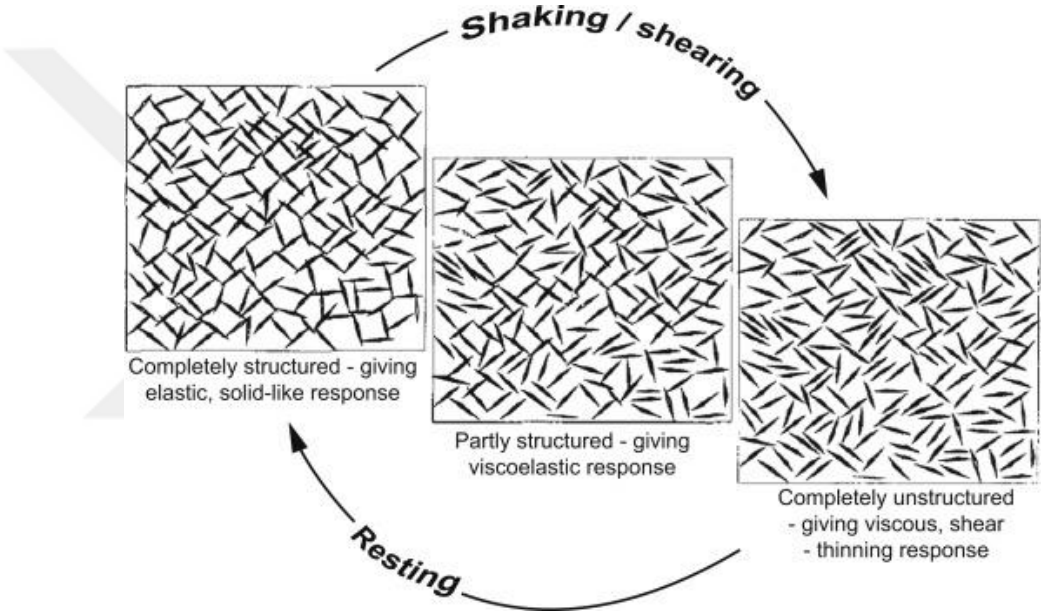

Figure 1.7 : Breakdown of a thixotropic structure (adapted from [83]).

In practical applications, rheological analysis often involves a three-phase approach, as exemplified by a study utilizing a rotary rheometer. This approach encompasses a resting phase, a squeegee behavior phase, and a recovery phase. Initially, the ink is subjected to a low shearing rate of 0.1 s^{-1}, mimicking the resting state. This is followed by a period of increased shearing, up to 200 s^{-1}, simulating the squeegee's action. Finally, the ink undergoes a recovery phase, where the shearing rate is reduced back to 0.1 s^{-1} [57]. This methodical approach enables a comprehensive understanding of the ink's behavior under conditions that closely resemble actual screen-printing processes.

1.7 Printing Technologies

Among several printing techniques as discussed in this section, the necessestiy of fast protoyping and ease of application revealed that screen printing is the viable process on the textile substrates. The summary of all printing techniques is given in Table 1.2. While all printing methods are briefly explained, more details are given for screen printing.

Table 1.2 : Printing techniques and their properties (adapted from [84]).

	Printing speed ($m^2 s^{-1}$)	Minimum dot size (μm)	Minimum layer thickness (μm)	Viscosity of ink (cP)	Ref.
Inkjet printing	10^{-3}–10	1–50	0.5–3	1–20	[85], [86], [87]
Flexographic printing	∼10	20	∼1	50–500	[85],[86]
Gravure printing	0.5–20	30	1–8	102–103	[86],[87]
Offset printing	7–70	10–50	<0.5	102–104	[86],[88]
Screen printing	10^{-3}–5	>20	5–100	500–5000	[86]

1.7.1 Inkjet printing

Inkjet printing includes several techniques where droplets of ink or other liquids are expelled from a tiny nozzle [89]. Inkjet printing operates in two modes: (i) drop-on-demand (DoD) printing, which releases droplets generated by thermal bubbles or a piezoelectric actuator, and (ii) continuous inkjet (CIJ) printing, which creates a continuous stream of ink through a nozzle using an electrostatic or magnetic field [90].

There are some early applications of inkjet technology in the electronics industry, such as a technique to create narrow conductive silver tracks without the need for pre-patterning or altering the surface energy of the substrate [91], using surface-energy patterns that cause the inks to repel and dewet from specific areas of the substrate [92] and creation DoD solder droplet jetting systems [93]. In addition, inkjet printing of all-polymer thin film transistor (TFT) circuits with via-holes and resistors [94] or antennas on substrates for RFID and WSN applications have been established [95]. A schematic of the inkjet printing process is given in Figure 1.8.

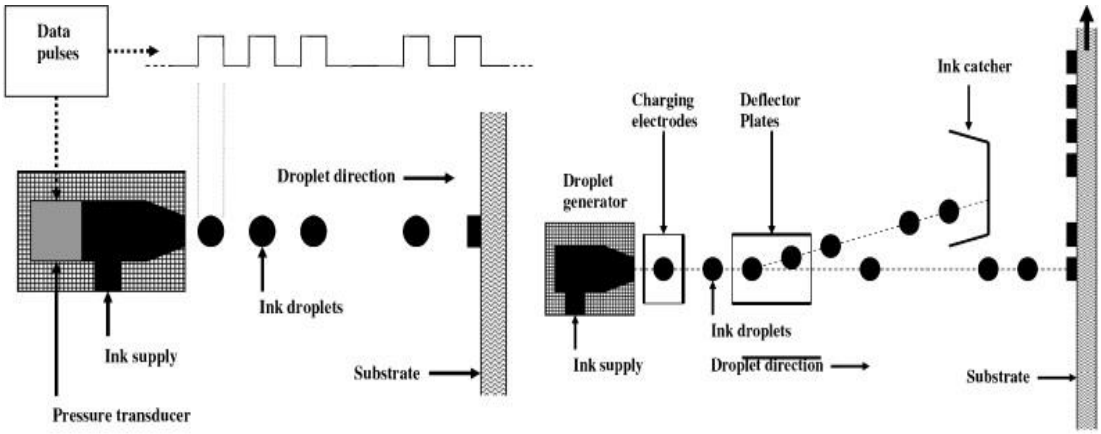

Figure 1.8 : A schematic of the inkjet printing process: (left) uses a data pulse train to generate droplets on demand via a pressure transducer, (right) continuously generates droplets, creating the pattern by deflecting unwanted droplets away from the substrate [96]).

1.7.2 Gravure and flexographic printing

In gravure printing the desired print pattern is inscribed as discrete cavities onto a rotary printing cylinder. During the printing operation, these cavities are filled with ink by passing through an ink bath, and a flexible doctor blade removes any excess ink. For inks with highly volatile solvents, a chambered doctor blade system may be used. The ink from the printing cylinder is then transferred to the substrate when the cylinder makes contact [97].

Flexography (is a continuous high-speed roll-to-roll printing process typically used for graphics printing in packaging applications. In this process, a printing roll coated with patterned flexographic rubber or photopolymer is inked by either direct contact with an ink bath or an intermediate inking roller, creating a uniform ink film on the raised designs. Excess ink is removed by an air-exposed doctor blade, similar to gravure printing. Finally, the image is transferred through direct contact with the substrate, which may consist of coated and uncoated paper, board, or plastic films [97]. Both printing techniques' schematics are shared in Figure 1.9.

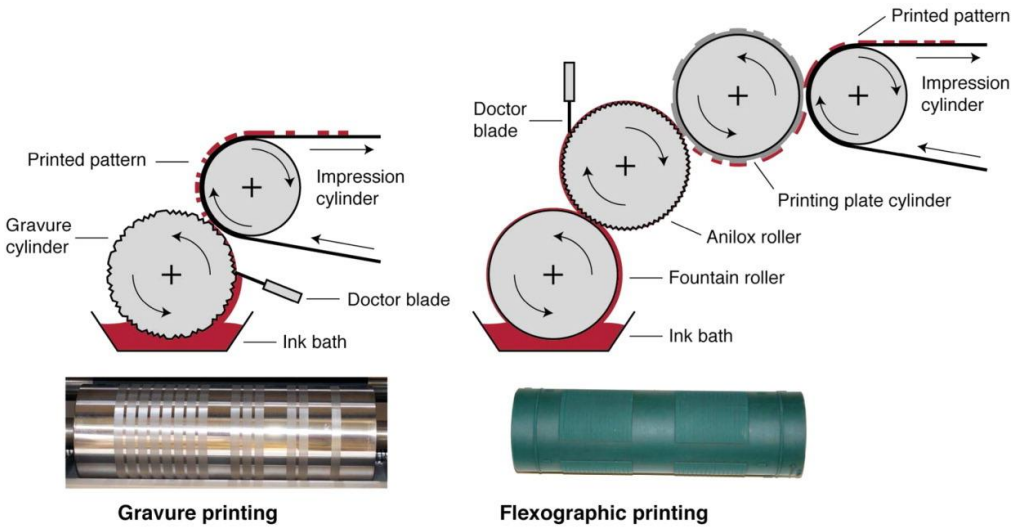

Figure 1.9 : Gravure (left) and flexographic (right) printing methods (adapted from [98]).

1.7.3 Offset printing

Offset printing, also known as offset lithography, is a widely used printing technique in which the inked image is transferred (or "offset") from a plate to a rubber blanket and then to the printing surface, typically paper. It is very well-known and cost-effective for mass printing. Figure 1.10 shows a simple schematic for demonstrating the offset printing process.

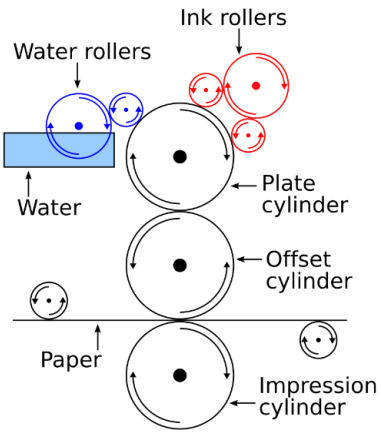

Figure 1.10 : Offset printing process (adapted from [99]).

1.7.4 Screen printing

Two challenges of manufacturing methods are paramount: simplification of the manufacturing process and decreasing costs. Screen printing is one of the key solutions to address both of these challenges owing to its simple process, low cost, ease of pattern implementation, and ability to produce in volume [54], [57], [100], [101], [102]. A major drawback of this process is its resolution size.

Screen printing transfers a liquid with a desired pattern onto a surface, usually onto a textile. The pattern is created with a screen that is adjusted to the surface. After some ink is spilled onto the screen, it is transferred to the textile by using a squeegee. It is important that once the ink is transferred, the pattern is preserved, and ink is well penetrated into the screen and diffused in the textile. For sensory applications, it is additionally important ink is continuous along the pattern to have good conductivity. The process of stencil preparation and screen printing is given in Figure 1.11.

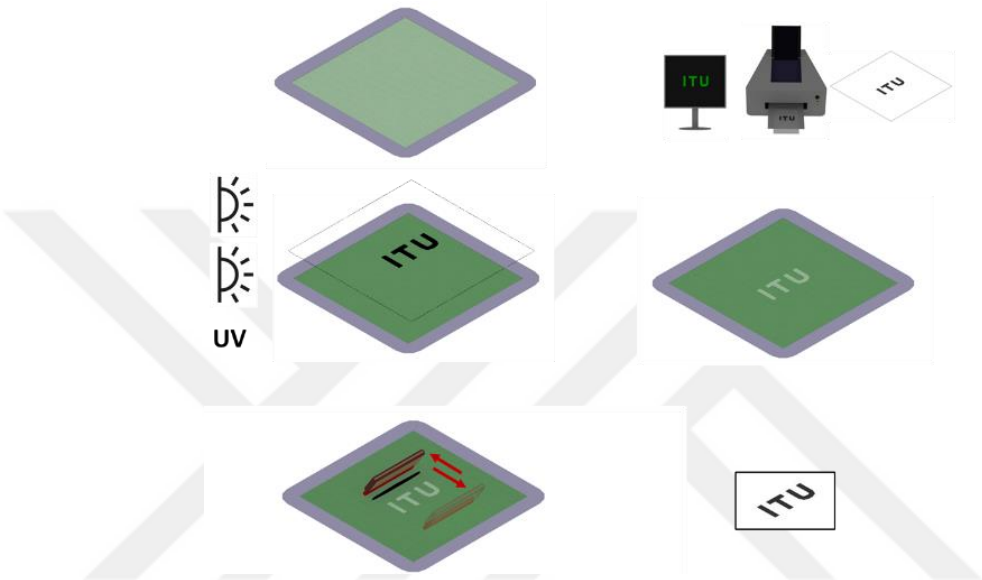

Figure 1.11 : Stencil design and ink application via squeegee. 1) The screen is acquired with the desired dimensions. 2) The pattern is designed and the mask is obtained. 3) The screen is coated with photoresistive emulsion, the mask is positioned, and the screen is developed with UV light. 4) Ink is applied, and the pattern is screen-printed onto the substrate using a squeegee.

In the field of screen printing, the judicious selection of mesh screens is a pivotal determinant of the ultimate quality and fidelity of the printed image. Screens with higher threads per inch (TPI) count, characterized by their finer mesh openings, are particularly well-suited for reproducing intricate graphics and small text. These screens facilitate precise ink deposition, enhancing the print's detail and resolution. Conversely, screens with a lower TPI count, featuring larger mesh openings, are advantageous for printing bold graphics and achieving high opacity on darker substrates due to their increased ink permeation.

The interplay between ink viscosity and mesh size also significantly influences printing. Thicker inks are often paired with coarser mesh screens (lower TPI), allowing for effective passage and deposition. In contrast, finer mesh screens are typically used with lower viscosity inks, which are more fluid and readily pass through the tighter

mesh openings. This harmonious relationship between mesh size and ink properties is essential for optimizing the printing process and achieving the desired print quality. This ensures print quality and prevents issues like clogging or ink bleeding i.e., wetting the textile more than design boundaries [102], [103], [104], [105], [106], [107], [108]. A schematic showing the squeegee movement and how ink is disposed to textile is given at Figure 1.12.

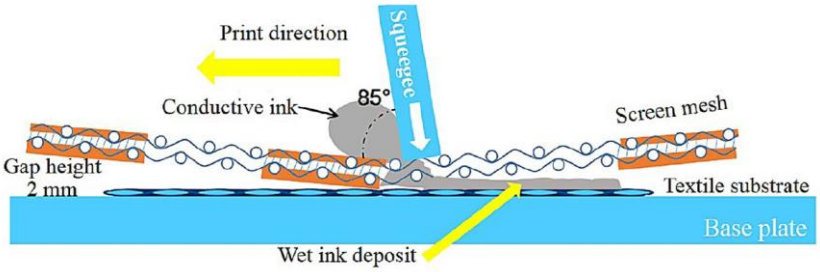

Figure 1.12 : Schematic diagram of screen printing in a cross-sectional view (adapted from [105]).

In terms of representation, US mesh count is represented as TPI, using imperial units and UK mesh count is metric using SI units. For example, 43T is metric and its equivalent is approximately 109 TPI. Elemental mesh geometry and its model are given Figure 1.13.

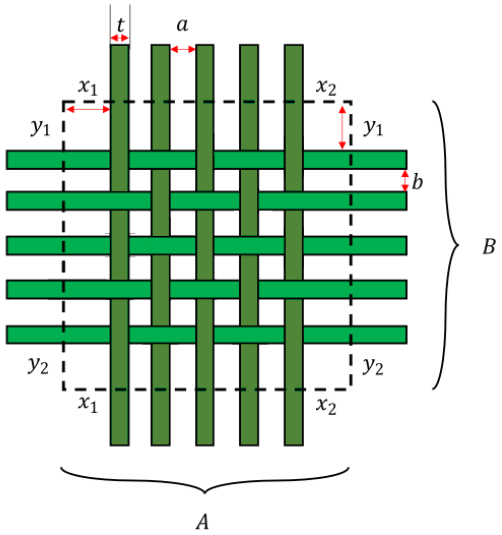

Figure 1.13 : Elemental mesh geometry, vertical lines as warps and horizontal lines as wefts.

$$A = x_1 + x_2 + n.t + (n-1)a \tag{1.5}$$

$$B = y_1 + y_2 + n.t + (n-1)b \tag{1.6}$$

Here, n means the line counts in one direction. By definition of 'T' metric, nT means n lines in 1 cm. In this form, $x < a$ and $y < b$. Otherwise, another line must be settled. $A = B = 1\ cm = 10\ mm$. Assuming $x = y = 0$, the equation takes the following form:

$$10 = n.t + (n-1)a \tag{1.7}$$

$$10 = n.t + (n-1)b \tag{1.8}$$

Taking the assumption of $a = b$, i.e., the meshes form squares as openings and taking $n = 90$ as it was also commercially used in this study; applying various thicknesses to the equation gives the plot represented as Figure 1.14 below.

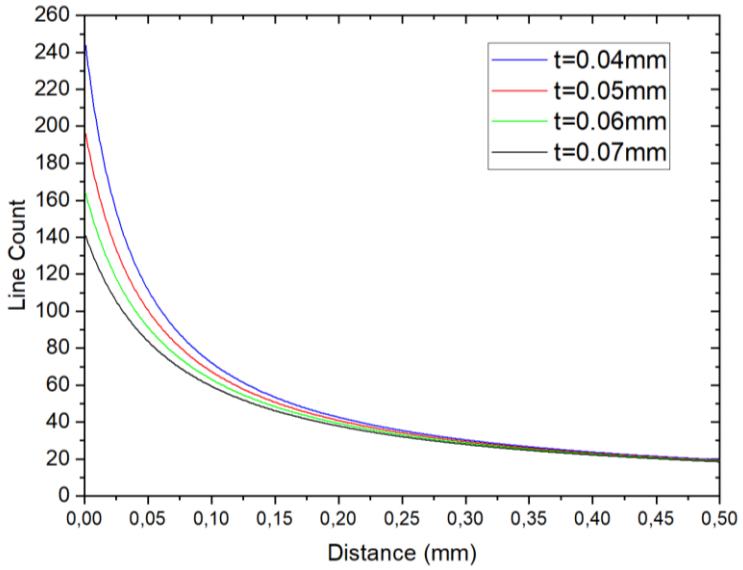

Figure 1.14 : Line counts (n) vs distance between the lines (a, b) in various thicknesses.

2. MATERIALS AND METHODS

2.1 Ink Characterization

Graphene ink was prepared in collaboration with Royal College of Art and with the support of Versarien ©, properties given in Table 2.1. Rheological testing is performed at the Faculty of Aeronautics and Astronautics at Istanbul Technical University using a rheometer (TA Instruments, Discovery Hybrid Rheometer 2). The instrument is configured with parallel plates, each with a radius of 25 mm, and a gap distance of 1 mm.

Table 2.1 : Properties of the graphene ink (with permission of Royal College of Art and Versarien ©).

Graphene content	10 mg/L
Total solid content	~10 wt.%
Flake type	Graphene & Graphene nanoplatelets
Lateral size	1000 ± 500 nm
Thickness	~10 ± 5 nm

The ink is prepared by microfluidization, which is a homogenization technique whereby high pressure (up to 207 MPa) is applied to a fluid, forcing it to pass through a microchannel (diameter, $d < 100$ μm) [109]. The method starts with the preparation of a graphite dispersion in a suitable solvent, which could be water, organic solvents, or surfactant-based solutions. This dispersion is then subjected to high-pressure flow through a microfluidizer, where the graphite is exfoliated. To improve the quality and uniformity of the graphene ink, the dispersion often undergoes multiple cycles through the system. A general look of the of the ink produced can be viewed at Figure 2.1 through SEM and TEM images provided by Versarien©.

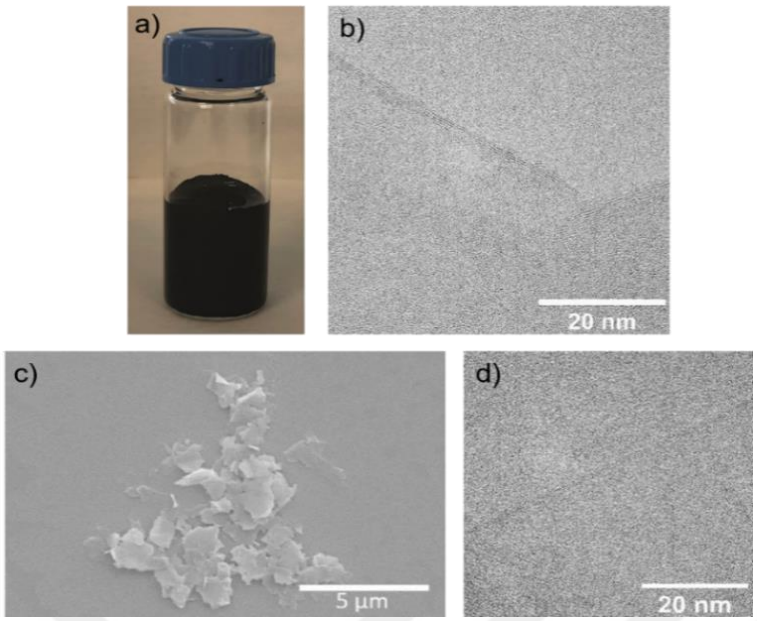

Figure 2.1 : a) General look of the graphene ink in its bottle. b and d) TEM images of the graphene ink. c) SEM image of graphene ink. used via permission of Versarien©.

2.2 Design of Sensor Patterns

Four patterns—line, strain gauge, serpentine, and omnidirectional—were selected for the study. Each geometry is designed to address specific functional requirements, enhancing the sensor's ability to detect mechanical deformation under different conditions. The patterns were drawn via computer with selected dimensions given in Figure 2.2; thus, screens are created commercially. 56% polyamide and 44% elastane fabric have been selected for the substrate.

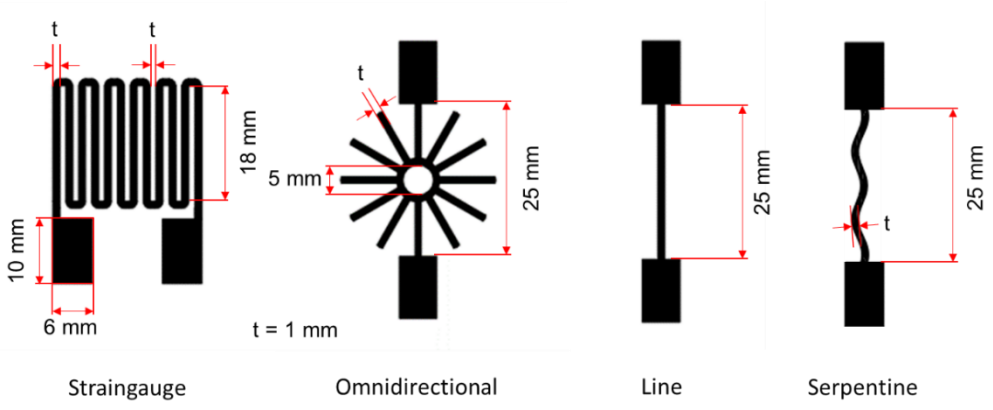

Figure 2.2 : Patterns.

The strain gauge geometry combines flexibility and sensitivity through its alternating curved structure. This design enables the sensor to withstand both tensile and

compressive strains, making it suitable for dynamic environments involving cyclic or repeated deformations. The wavy structure also enhances durability by absorbing mechanical energy, reducing the likelihood of failure in applications such as soft robotics and wearable devices.

The omnidirectional geometry ensures an even strain distribution across the sensor by radiating linear elements outward from a central hub. The central circular area often serves as a strain concentration point, enhancing sensitivity in the radial elements. This geometry is particularly effective for detecting multi-directional or complex strain distributions, making it suitable for applications like structural health monitoring and biomechanics, where strain occurs in various directions.

The line geometry provides a simple and direct path for strain detection, making it ideal for uniaxial strain sensing. Its straightforward design ensures consistent performance and ease of fabrication, making it a common choice for applications requiring precise strain measurements with minimal design complexity.

The serpentine geometry, characterized by its looping and curved structure, is highly flexible and capable of accommodating large strains without mechanical failure. The elongated conductive path within this design amplifies the relative change in electrical resistance when subjected to strain, thereby increasing the gauge factor and improving the sensor's sensitivity. This pattern is particularly useful in applications such as wearable electronics, where flexibility and the ability to detect significant deformations are crucial.

2.3 Screen Printing and Fabrication of the Sensors

The fabrication process of the sensors was methodically executed through a series of sequential steps which is explained in Figure 2.3. Initially, the textiles were prepared, followed by the alignment of the screen above the textile substrate. The first layer was screen printed with 30 mL of graphene ink, uniformly applied across the screen. The squeegee was held at approximately 75 degrees against the mesh and swept through the pattern five times—three strokes in a downward direction and two in an upward direction. The textile was then carefully removed from the screen and visually inspected for any major defects, such as excessive ink spread or insufficient ink coverage due to clogging in the stencil, thus creating the first layer.

Subsequently, the specimen was set to dry in a preheated oven at 50°C for 30 minutes. During this drying period, the screen mesh and squeegee underwent a cleaning process involving thorough washing with a sponge, water, and gentle soap to remove any residual ink and prevent potential clogging of the mesh. To ensure proper cleaning, the mesh was held up to the light to check for any blockages. The screen and squeegee were then dried with a heat gun, ensuring all moisture had evaporated. If there was sufficient time, a second specimen could be created.

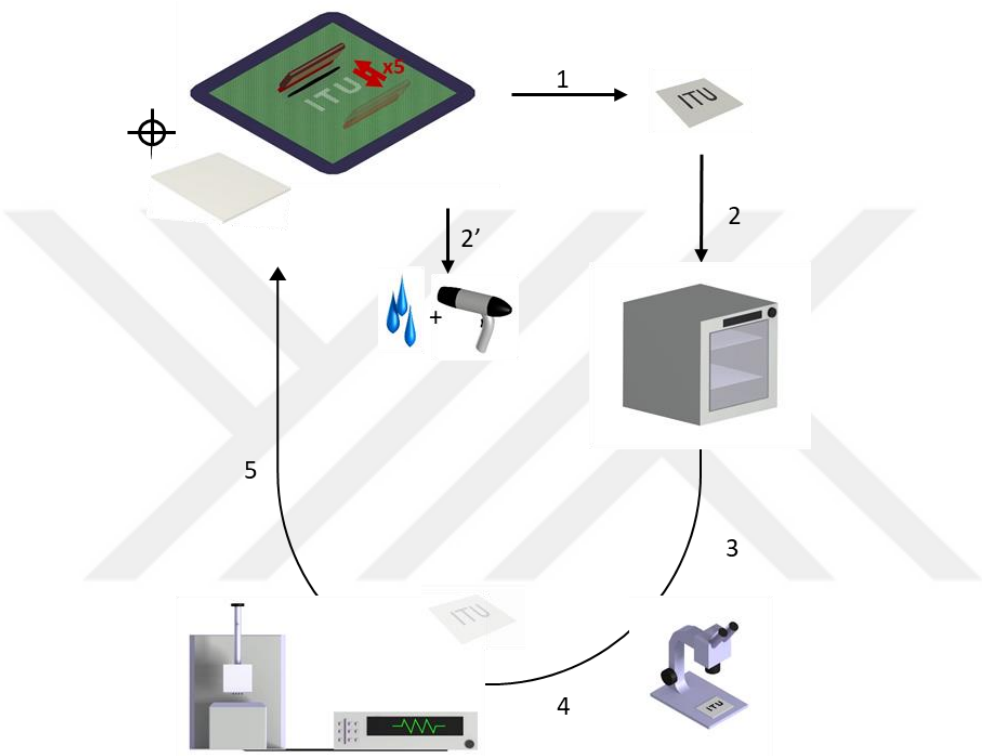

Figure 2.3 : Sensor fabrication process. 1) Textile positioning and screen-printing. 2) Drying the pattern at 50°C for 30 minutes. 2' rinsing and drying of the squeegee and the screen print. 3) Microscope characterization. 4) Electrical characterization. 5) Repositioning of the specimen for the next layer.

After drying, the textile was investigated through microscopic and general imaging techniques to assess the quality and uniformity of the printed layers. This work is focused on the characteristic features of the specimen and the electrolyte areas intended for silver coating. Images were captured at various zoom levels.

The final phase of the sensor preparation involved conducting electrical resistance measurements using a four-point probe (4PP) device as shown in Figure 2.4. Each electrolyte area was measured twice, resulting in four measurements per layer. The measurement process involved positioning the electrolyte area under the probe's projection and gently bringing the probes into contact until a slight resistance was felt.

It was observed that approaching the area too slowly while voltage was applied could cause arcing and burn the textile.

Once all these steps were completed, the specimen was reinserted into the screen-printing setup. The pattern on the textile was carefully aligned with the mesh pattern, using tape to aid in this alignment. These steps were repeated to create up to four layers, thus completing the fabrication process for electromechanical testing.

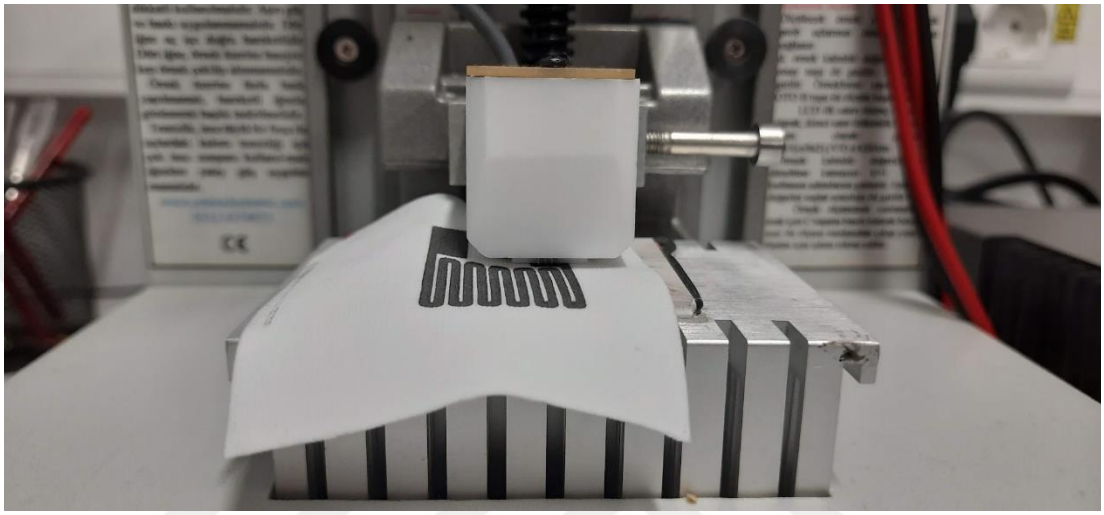

Figure 2.4 : 4PP measurement device.

All fabrication and testing processes are performed at ITU Aerospace Research Center laboratories, under a controlled environment.

2.4 Electromechanical Testing

After fabrication, the sensors were tested using a custom system developed in collaboration with the Ertunç Özcan facilities. The testing process begins by covering the electrolyte areas of the sensors with silver paste to enhance conductivity. Following this, the fabricated sensors were encapsulated with plexiglass for stabilization of their positions on the testing platform as shown in Figure 2.5. To ensure proper contact of the probes, two magnets are utilized, providing additional support during the alignment process. Once the specimens are positioned, they are securely fixed to the platform using screws, ensuring stability and consistent contact throughout the testing procedure. This methodical setup is essential for obtaining reliable and reproducible measurement data from the fabricated sensors.

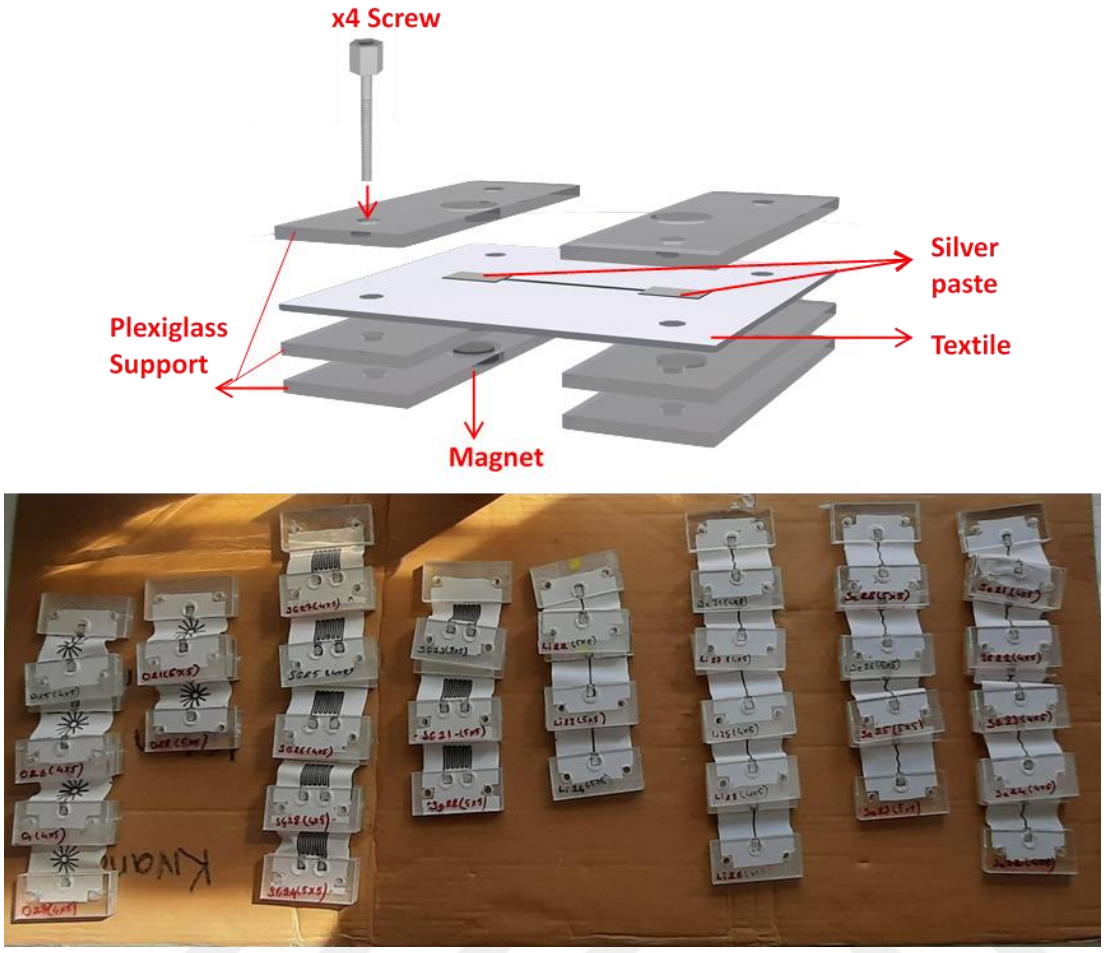

Figure 2.5 : Model for specimen creation (top) and batch of created specimens (bottom).

The experimental setup consists of four main components, as illustrated in Figure 2.6: a data recorder (in this case, a PC), a platform equipped with a motorized stage (Thorlabs) that applies uniaxial loads to the sample, a Keithley 2400 source meter, and software—APT User Program—integrated into the PC and controlled by LabVIEW software, which coordinates the platform's operation. Once the sample is mounted on the platform, the system applies specific strains at a sampling rate of 12 Hz. The applied parameters include acceleration, maximum speed, displacement level, and the number of cycles. These values are selected as 1.5mm/s^2, 0.25 mm/s, 1.25 mm (5% strain), 2.5 mm (10% strain) and 100 cycles, respectively.

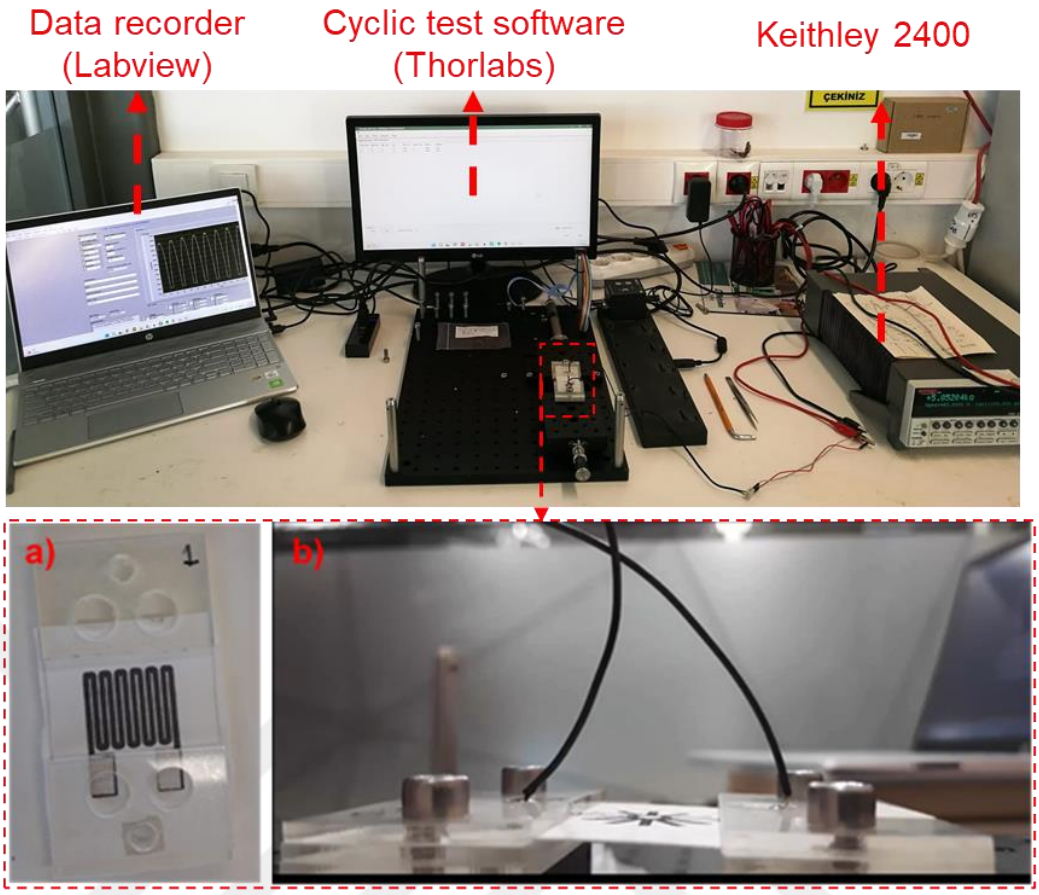

Figure 2.6 : Sample and in-situ testing views. a) prepared sample with silver paste applied. b) side view during testing where 2 electrodes were installed for data transfer.

2 main tests are conducted. Initial category consists of having I/V curves of three states; 0%, 5% and %10. Second one is for obtaining GF, through the cyclic measurement of 5% and 10% strain levels over time.

2.4.1 Testing procedure

For each fabricated specimen, a target strain level is selected for the initial bare measurement. These measurements are used to characterize the response of the selected strain level for a specific geometry. To gain further insight from the available specimens, additional measurements are conducted at the remaining strain levels. For the selected experiment, IV curves are obtained for both zero and the target strain level. After the target strain level is tested under cyclic loading, IV curves are subsequently obtained for zero strain level, the previous target strain level, and the next target strain level. This approach enables an assessment of the effects of both lower and higher strain levels on the target strain level. Additionally, it provides insights into the

variability of respiration, which is characterized by a combination of different strain levels over time. A schematic of protocols is given in Figure 2.7.

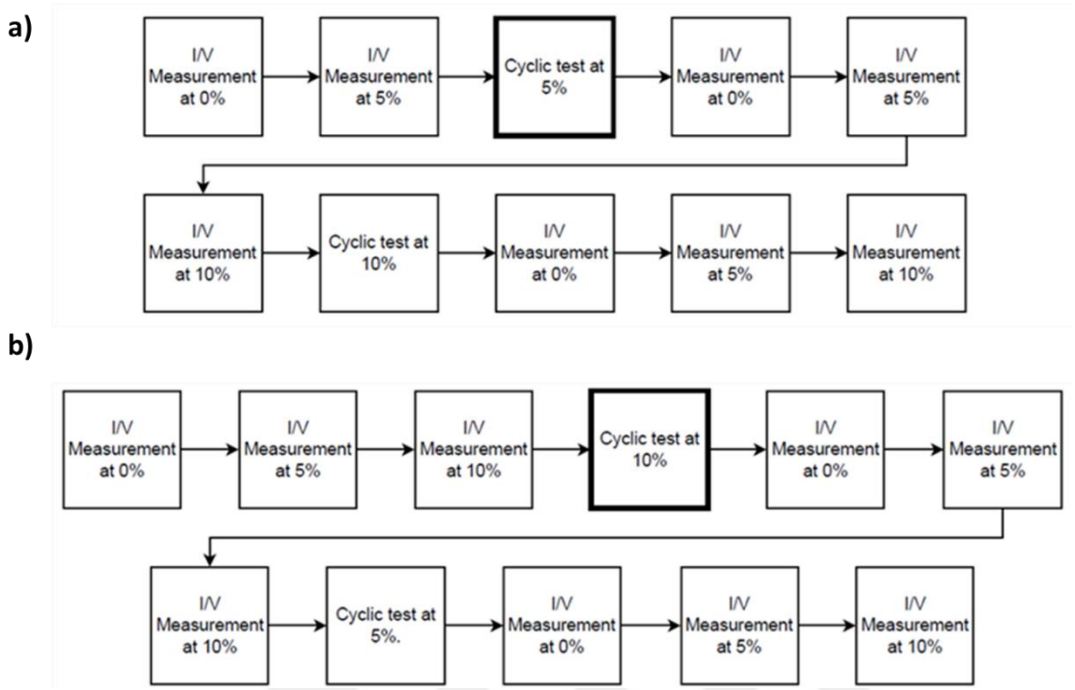

Figure 2.7 : Protocols for a) 5% and b) 10% cyclic tests.

While the main purpose of the measurements is to show the bare behavior as outlined in the black box above, it is viable to check alternative conditions for practical applications. For example, to assess whether the sensor can be used for long-term or one-time use as a disposable one.

2.4.2 Calculation of gauge factor

The MATLAB code provided in Appendix C is utilized for data processing. This code includes a segment dedicated to optimizing smoothing and averaging within specified thresholds for the standard deviation and mean gauge factor. This optimization is critical for accurately characterizing the sensor's general behavior. Specifically, excessively high standard deviations may yield artificial GFs due to momentary peaks, which fail to represent the sensor's overall performance. Conversely, an overly low standard deviation indicates excessive smoothing, resulting in a gauge factor that may underrepresent sensor responsiveness. The code operates based on five key parameters, which are as follows:

Avgnumber : How many data points are averaged. Default interval 2-10.

SmoothFactor : Smoothing factor of the graph. Default interval 0.001-0.06.

GFMEAN : Mean of the gauge factors calculated.

GFSTD : Standard deviation of the GFMEAN.

GFSTD / GFMEAN : Threshold not to exceed by the code, in other words, coefficient of variation (CV). Default value = 0.1.

Default parameter values do not always yield solutions. In this scenario, the CV is incrementally adjusted to identify an optimal solution. The selection of parameter values is critical, as they can significantly influence the GF, as previously discussed. The overarching strategy involves maximizing “GFMEAN” while minimizing the “Avgnumber” and “GFSTD” variables to achieve desirable and realistic performance outcomes.

3. RESULTS AND DISCUSSION

This section encompasses the determination of the mesh size, application of the studied patterns for screen printing, testing the ink using rheological instruments, the fabrication of sensors and execution of electromechanical testing.

3.1 Rheological Analysis

Rheological characterization, where results are shared in Figure 3.1 and Figure 3.2, revealed that the graphene ink displayed shear-thinning behavior as expected. A decrease in viscosity characterizes this as the shear rate increases. Both graphs show the viscoelastic properties of a material as a function of shear rate and oscillation strain, respectively. Both axes use a logarithmic scale, allowing for a detailed view across a broad range of strain percentages, except tan delta.

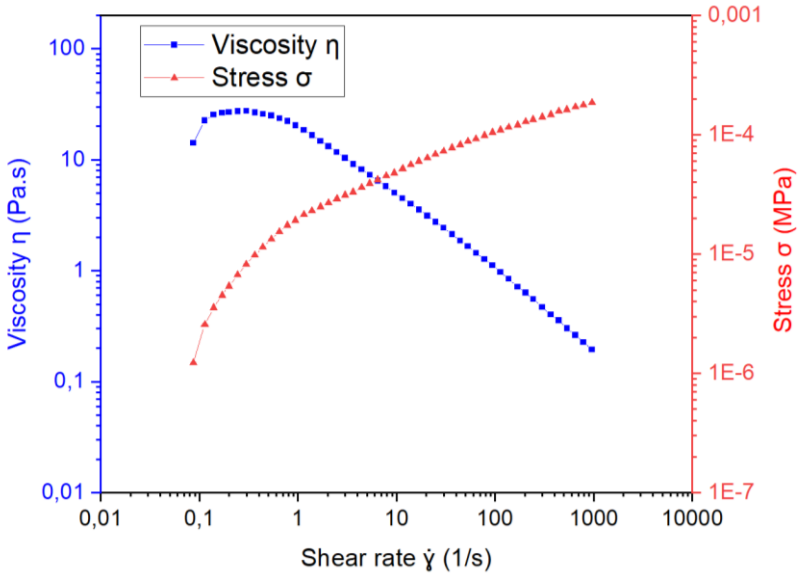

Figure 3.1 : Viscosity and stress behavior per shear rate for graphene ink.

The shear-thinning property facilitates efficient extrusion of the ink through the screen-printing mesh. The elevated force during printing reduces the viscosity, decreasing the resistance to the flow of the ink. Upon removal of shear stress, the ink's viscosity recovers, effectively preventing undesirable spreading within the fabric. This behavior assists in the preservation of the original design.

As summarized in Table 3.1, the storage modulus (G'), represented by the blue curve in Figure 3.2, reflects the material's elastic component, meaning its ability to store energy.

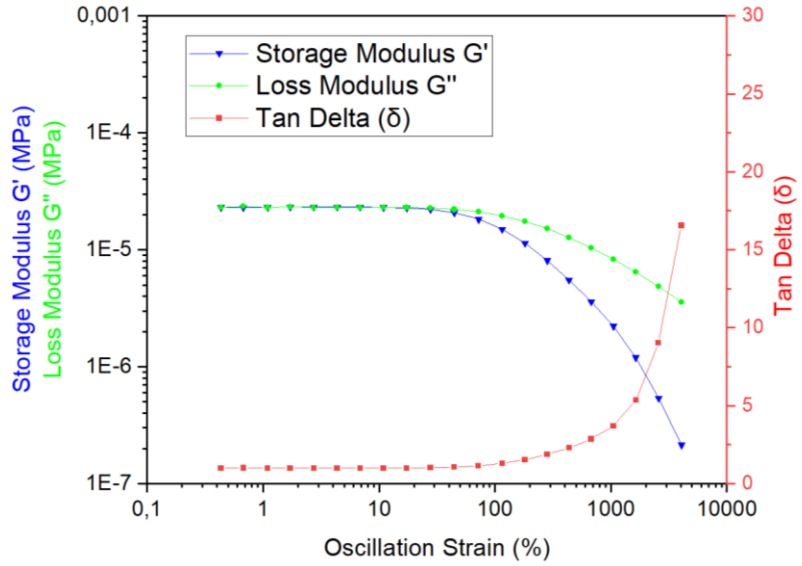

Figure 3.2 : Storage and loss modulus and Tan Delta per oscillation strain.

At lower strain levels, G' remains relatively constant, indicating that the material retains its structural integrity and elastic behavior. However, as strain increases beyond a certain threshold, G’ drops sharply, signaling that the material’s structure begins to break down, resulting in a decreased capacity to store energy elastically. This decrease suggests a shift from a solid-like behavior to a more fluid-like response.

Table 3.1 : Modulus/ink relationship.

Modulus relationship	Behavior of the ink
$G' > G''$ ($\delta < 1$)	Ink shows elasticity: Acts more like a solid, storing more energy than it dissipates.
$G'' = G$ ($\delta = 1$)	The material equally exhibits solid and liquid characteristics, marking a sol-gel transition.
$G'' > G'$ ($\delta > 1$)	Liquidity is more obvious, dissipating more energy than it stores.

The loss modulus (G"), shown by the green curve, represents the viscous component of the material or its ability to dissipate energy. Like G', G" is stable at lower strains but gradually decreases at higher strain levels. This behavior suggests that internal

friction within the material diminishes as its structure weakens, reducing the material's resistance to deformation through viscous effects.

3.2 The Measurement of Resistance

As mentioned, four patterns were selected for analysis: strain gauge, omnidirectional, line, and serpentine. The resistance properties across the layers of the remaining patterns exhibited a notable uniformity. The consistent resistance across different patterns indicates that the electrode areas remain unaffected, which is crucial for accurate measurements.

Once the initial designs were fabricated, as will be discussed in greater detail later, static resistance measurements were conducted using the 4PP method. It was measured that 76.32%, 10.42%, 2.81%, and 1.65% resistance changes are effective to the initial layer. As depicted in Figure 3.3, the differences in resistance measurements between the fourth and fifth layers were relatively small. Consequently, it was decided to investigate sensors in these two categories further to determine whether the GF is affected in a similar manner.

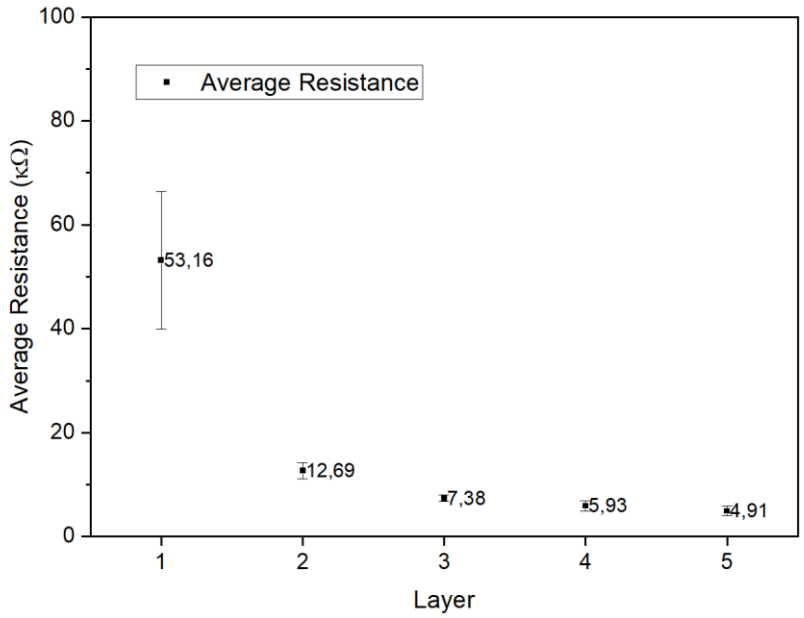

Figure 3.3 : Average resistance changes over the number of layers.

The obtained results were in line with similar research [109] where the resistance decreases in a parabolic manner as the number of layers increases.

3.3 Mesh Verification

Figure 3.4 contains the optical investigation obtained from the stencil. Various mesh sizes have been tested. It was decided that 90T is an optimum choice, as a smaller mesh size tends to dissipate ink over the textile, while a larger mesh size renders the ink difficult to pass through.

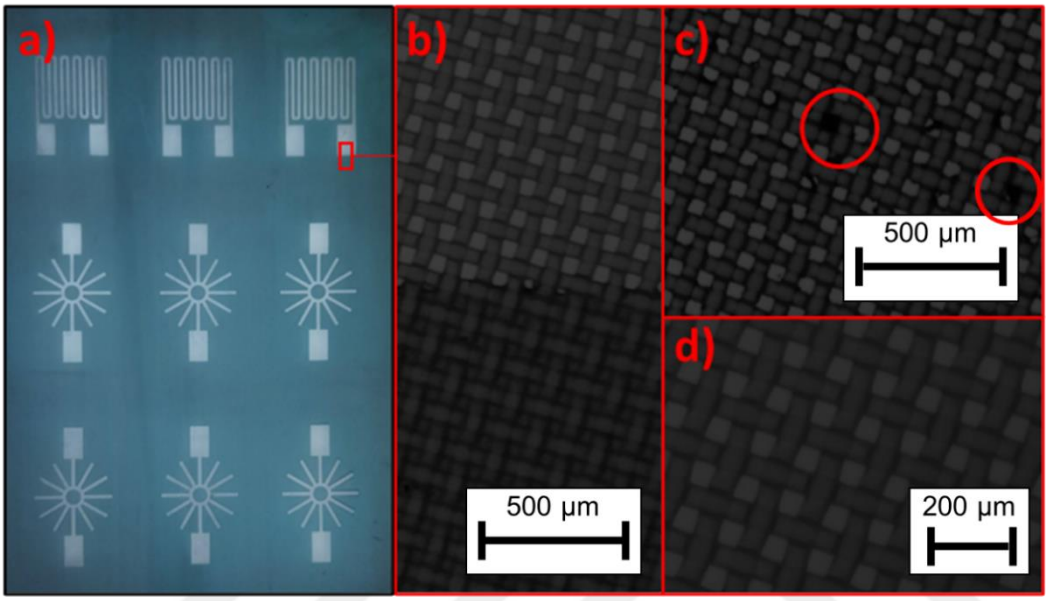

Figure 3.4 : Images from screen print. a) actual screen. b) zoomed image from meshes open and closed with photoresist. c) clogs due to usage encircled in red from mesh. d) enlarged, non-defected open mesh.

Random measurements were taken from the optical microscopic images of a commercial 90T silk screen depicted above. Measurements show line thickness t as 0,06013 ± 0,00100 mm and distance between the threads as 0,05872 ± 0,00322 mm, corresponding to 84T in Figure 1.14, which aligns with the theoretical calculations. Also, it can be observed that there are some defects after usage, as some meshes are still clogged.

3.4 Printing and Sensing Performance

In this section, qualitative comments are made to assess the effect of layer number on the final product. In each design, observations are made to ensure that sensors are fabricated without significant defects and that conductive tracks are continuous. However, especially with the strain gauge and omnidirectional designs, it can be observed that the layers did not overlap precisely with the previous one. Deviations from intended tracks were observed due to slight misalignments, especially in more

complex figures such as omnidirectional. Typical examples can be referred to in Figure 3.5.

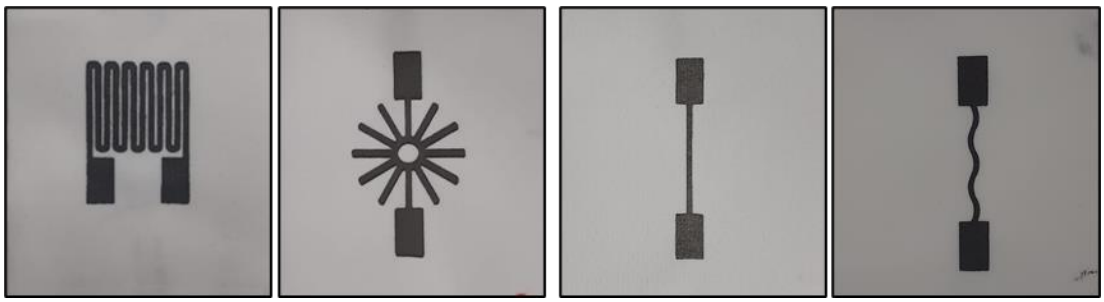

Figure 3.5 : Strain gauge (left), omnidirectional (middle-left), line (middle-right) serpentine (right) sensors, respectively.

3.4.1 Line

This section assesses the performance of the line sensors. The line sensor represents the most fundamental configuration among the selected geometries and is anticipated to exhibit the highest sensitivity, as measured by its GF. This heightened sensitivity arises from the lack of alternative electron pathways, as opposed to more complex geometries that may distribute the strain across multiple conductive channels. Consequently, the line geometry is more directly affected by mechanical strain, significantly influencing its electrical properties.

In addition, due to their simplicity, line sensors are theoretically more prone to noise and measurement variations. This increases their susceptibility to defects and environmental interference. This increased noise is expected to lead to greater measurement deviations compared to more intricate geometries that may offer more stable performance.

As the strain level increases, conductivity is expected to decrease, leading to higher resistance values, as indicated by the slope of the IV curves. This inverse relationship between strain and conductivity aligns with the general behavior of conductive materials under mechanical deformation. Furthermore, the linearity of the IV curve, whether in a resting state or under strain, is more likely to deviate in the line sensor geometry. This is primarily due to the dominance of defects and imperfections in simpler geometries, which can disrupt the uniformity of electron transport, thus affecting both GF and overall sensor performance.

The following sections present the effect of printing quality on the sensor performance of 4x5 and 5x5 layered line sensors. Then, the IV behavior of various strain conditions

is discussed. Finally, similar to IV characteristics, the cyclic performance of the line sensor is evaluated.

3.4.1.1 The effect of printing quality on the sensor performance

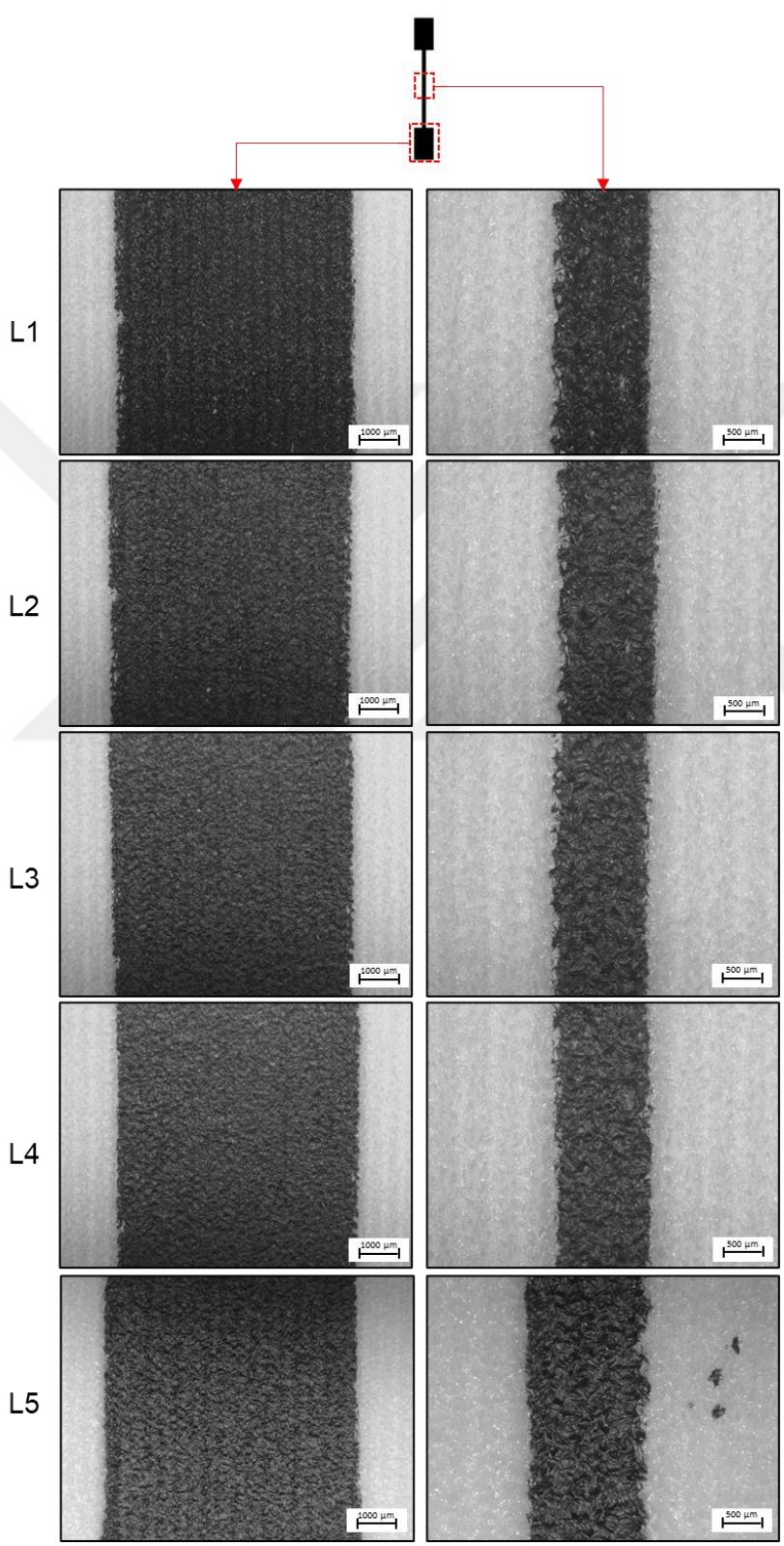

Figure 3.6 : Figures from line sensor, layer 1 to layer 5 (randomly taken).

The images in Figure 3.6 illustrate the progressive enhancement in the uniformity and smoothness of graphene ink dispersion across the textile substrate as the layer count increases. Each layer in the multi-layered line sensor structure is constructed with five strokes (three downward and two upward), encompassing 4x5 and 5x5 configurations. As the number of layers increases, visible irregularities, observed as white areas within the sensing sections, decrease. This reduction in irregularities demonstrates improved control over ink distribution, likely due to the cumulative smoothing effect of successive layers.

However, while additional layers contribute to better boundary definition and pattern fidelity, they also introduce a potential risk of misalignment. This misalignment can manifest as minor deviations along the pattern edges, which may increase the overall thickness along the XY axis. Although misalignments are not substantial enough to compromise the sensor's core conductivity, they could affect sensor performance by disrupting percolation pathways within the graphene network. Disruption in percolation could, theoretically, impair electrical performance by creating areas of higher or lower conductivity.

The cross-sectional imaging in section 3.4.5 reveals that the ink dispersion across layers shows a parabolic distribution, an outcome attributed to two primary factors. First, the textile's intrinsic properties and the graphene ink's viscosity encourage lateral dispersion, which resembles capillary action at the microscopic level. Second, even slight misalignments during successive layer applications may lead to uneven ink printing, with an increased deposition at the side of the pattern’s edges. This effect can impact the conductive layer's overall uniformity, although the core structure's consistency minimizes its significance for practical conductivity.

Repetitive use of the screen-printing mesh and necessary rinsing and drying cycles can also introduce minor defects in the printed patterns. Such defects are occasionally observed as black dots in areas distant from the primary sensing pattern. These extraneous deposits do not interfere with sensor functionality, as they fall outside the conductive pathway. Nonetheless, they underscore the importance of regular maintenance and inspection of the screen-printing apparatus. Over time, wear and tear on the mesh can lead to unintentional ink deposits in non-conductive areas and may even affect the edges of the conductive patterns, highlighting the need for ongoing quality control.

Furthermore, given the smaller area of the line sensor pattern, the degree of ink diffusion into the textile substrate may be more pronounced compared to larger patterns, especially with a uniform ink volume (e.g., 30 mL) applied across different designs. While this observation suggests a potential variability in ink absorption rates based on pattern size, a precise assessment would require more advanced imaging techniques, such as Scanning Electron Microscopy (SEM), to quantify the extent and nature of diffusion.

The findings highlight a generally effective and uniform ink deposition process for the multi-layered graphene-based line sensor, which is suitable for textile applications. However, certain factors—such as potential misalignment during multi-layer printing and minor extraneous deposits—indicate areas where process control could be further optimized. These observations underscore the need for careful management of screen-printing protocols to ensure the durability and consistency of the sensor's conductive pathways, especially for applications in wearable electronics where structural integrity and consistent electrical properties are paramount.

3.4.1.2 Analysis of IV curves

This section examines the IV curves to determine their linearity across different voltages and how these characteristics change after testing in starting with 4x5 patterns. As the procedure evolved, as depicted in Figure 2.7, there were some gaps in the number of measurements collected due to the iterative nature of the experimental process and the challenges associated with handling large volumes of data. Despite these gaps, a sufficient dataset exists to analyze the primary objective: understanding how the IV curve changes at different strain levels. The remaining data provide additional insights that supplement the core findings.

Certain data have been excluded due to substantial deviations from the rest of the dataset, which have been identified as outliers. These deviations are generally attributed to alignment issues of the testing specimen within the test setup, as wrinkles or internal stresses can develop during integration. In some cases, inadequate diffusion of the ink also resulted in unusually high resistance values. Consequently, the revised dataset used for analysis is shown in Table 3.2. For clarity, the term "Strain Alteration" explains what kind of procedure was applied. Bare means the specimen is strained for the first time to the dedicated strain level. Post X% means a 100-cycle test of X% strain

was applied to the specimen. Then, the average resistance at the related strain level was measured. In addition, “Post X% (Post Y%)” means a 100-cycle test of Y% strain was applied first, then a second 100-cycle of X% electromechanical test was applied, and then resistance was measured at the related strain level. This method gathers as much information as possible for both strain levels from each specimen.

Table 3.2 : Line sensor resistance levels per IV curves (4x5).

Max Layer	Strain Level	Strain Alteration	Avg. Resistance (kΩ)	St. Deviation (kΩ)	#
4	0%	Bare	2.92	0.52	5
	5%	Bare	4.24	0.87	3
	10%	Bare	11.31	2.55	3
	0%	Post 5%	1.90	-	1
	5%	Post 5%	4.80	-	1
	10%	Post 5%	13.99	-	1
	0%	Post 10%	2.96	0.82	3
	5%	Post 10%	10.09	0.03	2
	10%	Post 10%	17.38	-	1
	0%	Post 5% (Post 10%)	-	-	-
	5%	Post 5% (Post 10%)	-	-	-
	10%	Post 5% (Post 10%)	-	-	-
	0%	Post 10% (Post 5%)	2.39	0.10	2
	5%	Post 10% (Post 5%)	7.13	-	1
	10%	Post 10% (Post 5%)	16.55	-	1

The 4x5 layered bare tests exhibit the most rudimentary form of the testing along with 5x5 bare tests, leading to elevated standard deviations, which can be considered typical at this stage of development. However, this contrasts with the 4PP measurements, where more consistent data were obtained. This discrepancy may be attributed to silver pastes in the 2PP measurements derived from the current data. Notably, the 4PP measurements lacked silver paste. Furthermore, the IV characteristics were derived from the patterns (sensing geometries) in the 2PP measurements. While the contact measurement areas can be printed with consistent quality, the consistent reproduction

of patterns poses a greater challenge. Therefore, the observed variations in pattern measurements are reasonable compared to the more stable contact resistance values.

For bare strain levels of 0%, 5%, and 10% in the 4x5 layered configuration, the ratios of the standard deviations to the slopes of the IV curves—representing resistance in accordance with Ohm's law—were 0.52, 0.87, and 2.55, respectively. This increase in variability with higher strain levels is expected as the number of cracks and types of cracks rise with increasing strain for each specimen [110].

Observed resistance changes were 45.12% from 0% to 5% strain, 167.09% from 5% to 10% strain, and 287.62% from 0% to 10% strain. While the increase in resistance is proportional to the strain level, indicating reduced conductivity as the sensor stretches, the relationship is non-linear, highlighting suboptimal performance in terms of linearity—an important parameter for sensor functionality. These findings will be examined further in the context of GFs.

The IV measurement results for specimens subjected to pre-testing indicate that prior testing has a notable impact on resistance. Due to the limited number of pre-tested samples relative to the bare ones, making precise conclusions for each strain alteration is challenging. Nonetheless, an increase in resistance was consistently observed for both 5% and 10% strain levels. This increase may be attributed to the formation and maturation of microcracks following testing [111], as suggested by the reduction in standard deviations. A larger sample size and SEM imaging would be necessary to quantify this effect accurately.

Importantly, the IV values at 0% strain remained consistent regardless of prior testing. This suggests that the effects of microcracks are reversible when the textile is unstrained, indicating good repeatability in the manufactured sensors. This characteristic is advantageous, as it reflects the sensor’s capacity to maintain stable baseline measurements after cyclic loading.

The 5x5-layered sensors, whose properties are given in Table 3.3, demonstrate significant variations in performance across different strain levels. This can be attributed to the increased stiffness introduced by the fifth layer, which affects the sensor's mechanical and electrical properties.

Table 3.3 : Line sensor resistance levels per IV curves (5x5).

Max Layer	Strain Level	Strain Alteration	Avg. Resistance (kΩ)	St. Deviation (kΩ)	#
5	0%	Bare	2.47	1.25	4
	5%	Bare	7.77	7.32	4
	10%	Bare	5.33	-	1
	0%	Post 5%	3.29	1.57	3
	5%	Post 5%	12.41	7.81	3
	10%	Post 5%	116.82	19.73	2
	0%	Post 10%	1.96	-	1
	5%	Post 10%	5.54	-	1
	10%	Post 10%	6.50	-	1
	0%	Post 5% (Post 10%)	1.86	-	1
	5%	Post 5% (Post 10%)	5.54	-	1
	10%	Post 5% (Post 10%)	6.73	-	1
	0%	Post 10% (Post 5%)	3.24	1.24	3
	5%	Post 10% (Post 5%)	21.76	11.36	3
	10%	Post 10% (Post 5%)	92.94	28.49	2

The resistance changes observed during bare testing were substantial, with an increase of 213.91% from 0% to 5% strain and 116.06% from 0% to 10%. On the other hand, there is a decrease of 31.17% from 5% to 10%. However, the results related to the 10% strain should be interpreted with caution, as the sample size for this strain level was limited to a single measurement, rendering conclusions about the 10% strain level inconclusive in bare testing mode.

After subjecting the sensors to cyclic testing at 5% strain, a noticeable increase in resistance was observed. This reduction in conductivity can be attributed to the formation of microcracks during repeated strain cycles. However, post-10 % strain application did not alter the resistance values as significantly as the 5% strain. Again, there is only one sample in this mode. Similarly, post-5 % testing following the 10% strain test did not significantly alter the measurements. Nonetheless, while pre-strain is expected and observed in these mods, the magnitude of this effect remains inconclusive.

Applying a 10% cyclic test after the 5% test subjected the sensor to maximum stress, potentially forming additional microcracks and disrupting the conductive network. Notably, conductivity improved at 10% strain, though variability effects remain unclear, and resistance at 5% strain continued to rise.

As shown in Figure 3.7, the IV measurements reveal that 4x5 layered graphene ink sensors exhibit superior linearity across all strain levels compared to 5x5 ones.

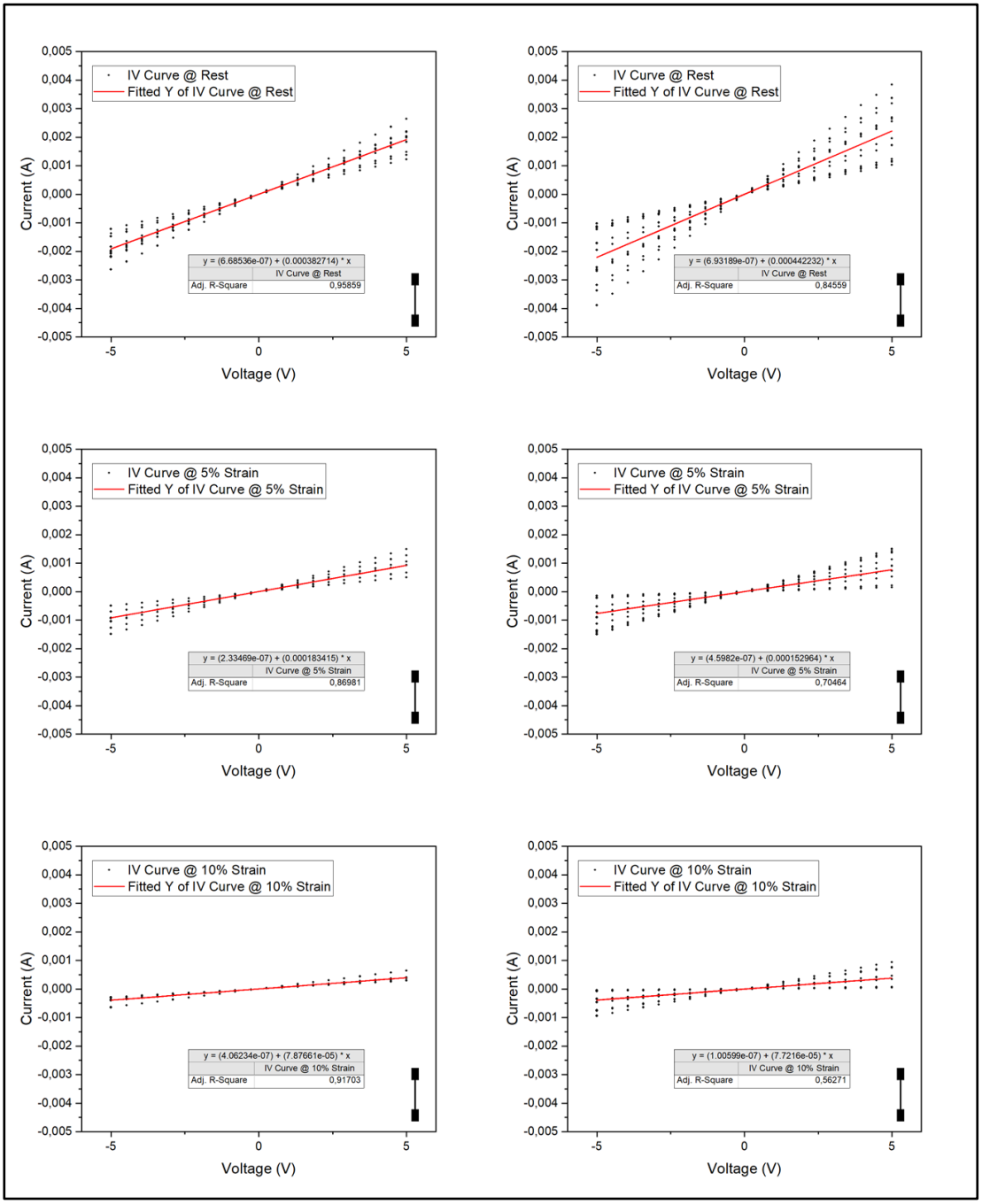

Figure 3.7 : IV measurements of line sensors 4x5 (left), 5x5 (right).

At rest, the 4x5 layered sensor achieves an R-squared value of 0.96 and maintains relatively high linearity under 5% and 10% strain, with R-squared values of 0.87 and 0.92, respectively. This stability suggests that the 4x5 layer configuration provides a reliable and predictable response under varying strain conditions, likely due to an optimal balance between flexibility and conductivity. In contrast, the 5x5 layered sensor demonstrates reduced linearity, with R-squared values of 0.85 at rest, 0.71 at 5% strain, and 0.56 at 10% strain. The added layer increases stiffness and susceptibility to microcracking, which may disrupt conductive pathways and compromise the sensor's linear response under strain. Consequently, for applications requiring consistent linearity in response to strain, the 4x5 layered sensor is likely more suitable, while the 5x5 layered sensor may require design adjustments to reduce the impact of increased stiffness and structural variability.

Table 3.4 presents the resistance behaviors of 4x5 and 5x5 layered sensors under varying strain levels, independent of pre-strain, showing a mixed response of all conditions.

Table 3.4 : Overall resistance levels per IV curves.

Sensor	Max Layer	Strain Level	Avg. Resistance (kΩ)	St. Deviation (kΩ)	#
Line 	4	0%	2.74	0.68	11
		5%	6.40	2.79	7
		10%	13.64	3.42	6
	5	0%	2.77	1.32	12
		5%	12.05	10.55	12
		10%	51.48	54.27	9

Two fundamental changes were observed. First, adding a fifth layer increases resistance across all strain levels, with a minimal increase at 0% strain. This is plausible, as the increased layer count enhances stiffness, which becomes more pronounced under strain. Electrons move over the surface, and adding an extra layer increases the sensor's susceptibility to microcrack formation, potentially disrupting the conductive flow. However, this effect is negligible when the sensor is unstrained.

Second, resistance values consistently correlate with strain levels, which is expected, especially within this geometry, due to its simplicity. This consistency in behavior,

regardless of layer count, demonstrates the sensor's reliability and repeatability under strain, indicating that the observed behaviors are stable across different configurations.

Overall, while adding layers to line sensors increases strain sensitivity, it also introduces variability, especially under higher strain levels. This variability likely arises from structural changes, such as microcracking or separation between layers, which impair the conductive network and lead to fluctuations in resistance. Thus, while 5x5 configurations may offer heightened sensitivity, they may be less suitable for applications requiring precise and repeatable measurements under significant strain due to their structural instability.

3.4.1.3 Cyclic test analysis

Table 3.5 provides the GF measurements for 4x5 layered and 5x5 layered line sensors under various strain levels and conditions. The analysis of these results reveals distinct behaviors based on the layer count and strain conditions, highlighting the trade-offs between sensitivity and stability.

Table 3.5 : GFs per different strain alterations measurements.

Sensor	Max Layer	Strain Level	Strain Alteration	Mean GF	Std GF	#
Line 	4	5%	Bare	25.88	3.82	2
		10%	Bare	40.39	16.87	3
		5%	Post 10% Test	40.81	11.72	3
		10%	Post 5% Test	36.40	40.89	2
	5	5%	Bare	46.84	28.67	3
		10%	Bare	18.42	-	1
		5%	Post 10% Test	78.81	44.91	2
		10%	Post 5% Test	85.63	67.78	3

For the 4x5 layered sensor, the mean GF under bare conditions at 5% strain is 25.88, with a standard deviation 3.82. At 10% strain, the mean GF increases to 40.39 with a standard deviation of 16.87, suggesting enhanced sensitivity to strain. However, the increase in variability, as indicated by the standard deviation, suggests that higher strain levels may induce microstructural effects, influencing measurement consistency. Following the 10% cyclic test, the GF for 5% strain remains similar, with a mean of 40.81 and a standard deviation of 11.72. For 10% strain following the 5%

test, the mean GF decreases slightly to 36.40, with a more significant standard deviation of 40.89, indicating greater variability. Increased variability may stem from cyclic loading, causing minor structural changes that affect the sensor's conductive pathways. The 5x5 layer configuration shows higher GF values than the 4x5, indicating greater sensitivity with increased layer thickness. The bare condition GF at 5% strain reaches 46.84, while it decreases to 18.42 at 10% strain for one sample. After exposure to previous strain conditions, the GFs increase substantially, reaching 78.81 and 85.63 at 5% and 10% strains, respectively, in the post-10% and post-5% test conditions. Elevated values suggest cumulative strain increases sensitivity, but high standard deviations (67.78 post-5% test) indicate structural changes like microcracks or layer separations disrupting conductive pathways.

Figure 3.8 shows the behavior of two test modes: bare strain (top row) and post-strain (bottom row) at 5% strain over 100 cycles. The plots depict resistance over time (left) and percentage resistance change between 600–800 seconds (right).

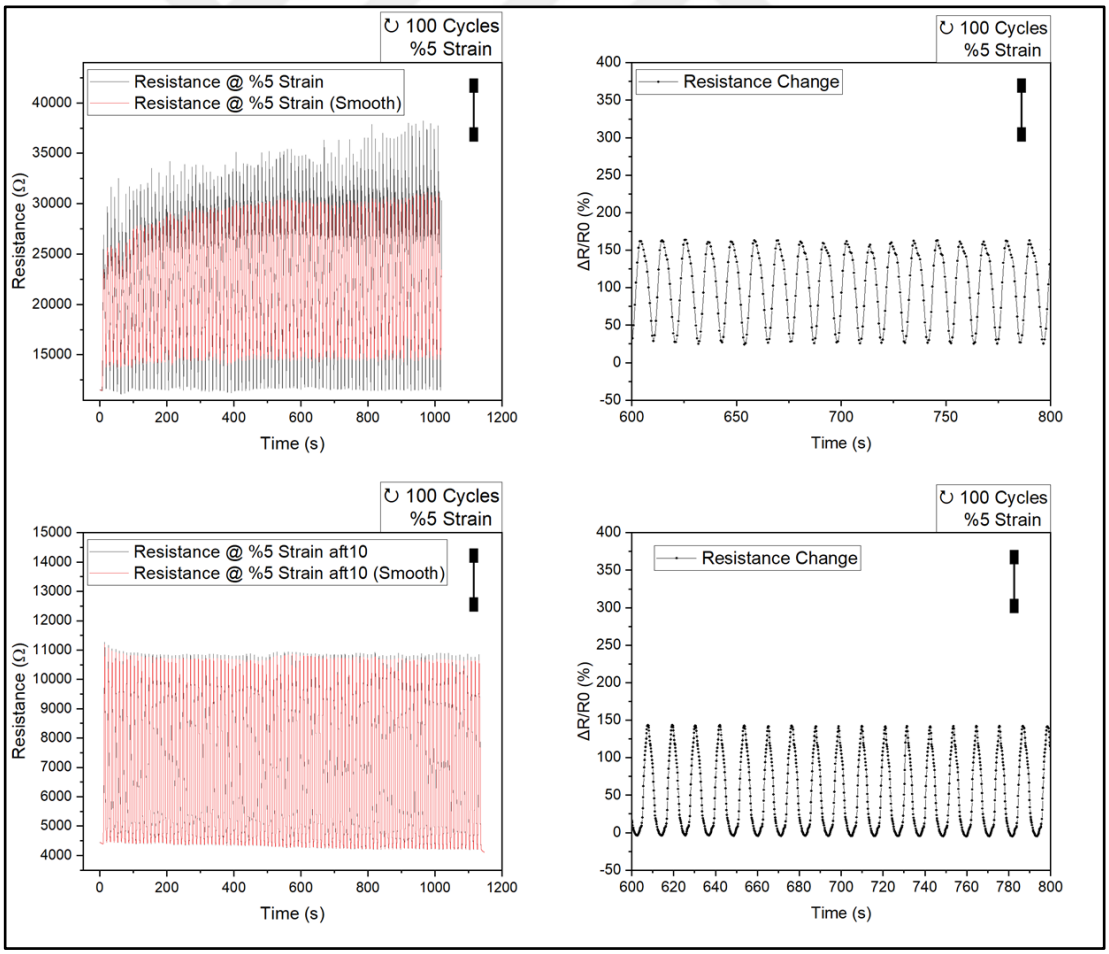

Figure 3.8 : Cyclic behavior of line sensor of 5% strain for 4x5 layers.

For the first sensor category (top row), the raw resistance data gradually increased over the test duration, superimposed with cyclical fluctuations corresponding to each strain cycle. This progressive upward trend suggests that baseline resistance is rising, potentially due to microstructural changes within the sensor material, such as microcrack formation or the gradual degradation of conductive pathways under repeated mechanical loading. Such behavior is consistent with known fatigue mechanisms in conductive composites, where repeated strain can compromise structural integrity, leading to an increase in resistance [112]. The smoothed data highlights this trend more clearly, showing both the cyclical response to each strain event and the gradual baseline increase over time. This pattern indicates that the sensor may be experiencing wear and microstructural adaptation as it undergoes cyclic loading, which could impact its long-term performance.

A closer examination of the resistance changes within the interval between 600 and 800 seconds reveals oscillations ranging from approximately 25% to 160%. These regular peaks and troughs demonstrate stable cyclic performance, with the sensor reaching similar resistance values at each peak and returning to baseline levels despite the gradual resistance increase. Notably, this interval also represents the minimum resistance values in the entire dataset, suggesting that values in subsequent intervals begin from higher baseline points. This behavior implies that the initial cycles might facilitate a "bedding-in" process, where structural stabilization occurs early in the testing period, leading to more consistent responses in subsequent cycles. This aligns with the fatigue behavior observed in many strain-sensitive materials, where early cycles stabilize the material, allowing for more reliable readings in later cycles.

Resistance measurements post an initial 10% strain exposure are shown in the lower-left plot, highlighting a stabilized baseline compared to the initial state, with resistance levels lower than the initial 5% strain condition. This indicates that the prior exposure to higher strain may have structurally adjusted the sensor, resulting in a more consistent baseline under subsequent 5% strain cycles.

During the same interval (600-800 seconds), the resistance change in the second category fluctuates between 0% and 150%, with stable peaks and troughs that indicate consistent cyclic sensitivity. The lower resistance variation in this sensor may imply a more stable internal structure or reduced susceptibility to microstructural disruption under strain. It could also suggest that this sensor operates within a strain range that

does not induce significant structural damage, thereby enhancing the repeatability of measurements.

A key finding is the impact of pre-straining on data smoothness. The pre-strained testing results exhibit reduced noise and more stable readings, likely due to a more settled internal structure following the pre-strain. This effect may result from initial strain aligning or compacting conductive pathways within the graphene network, thus making the material less sensitive to minor deformations and enhancing its sensitivity. The influence of 10% pre-strain on crack formation appears significant, as it leads to greater stability at lower strain levels.

Figure 3.9 represents resistance data for two 5x5 layered testing modes, each subjected to 100 cycles at 5% strain. The top row shows measurements taken during a baseline 5% strain test, while the bottom row displays data for a 5% strain test conducted after an initial 10% strain test.

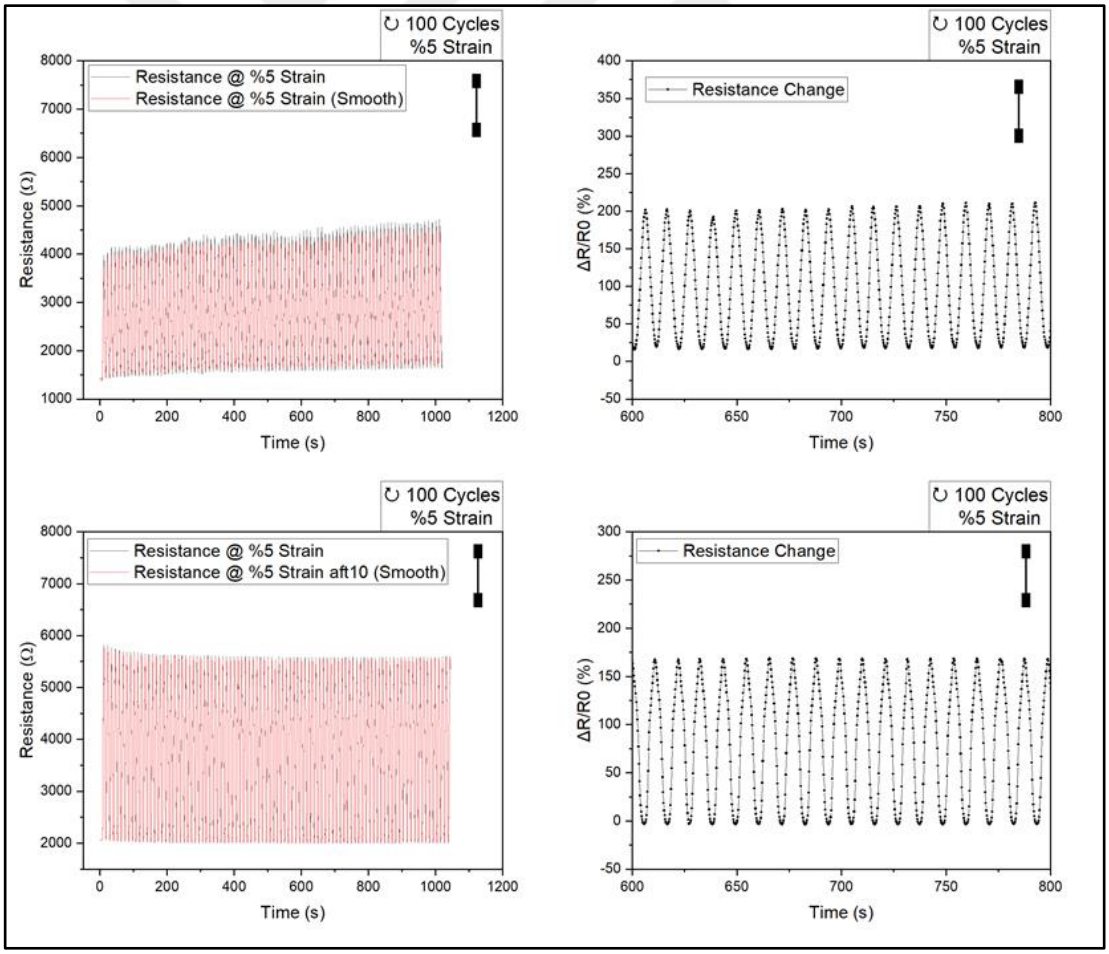

Figure 3.9 : Cyclic behavior of 5x5 line sensors of 5% strain level.

In the top row, which represents the baseline 5% strain test, the resistance data shows cyclic fluctuations and a gradual increase in baseline resistance. The raw data captures detailed fluctuations, while the smoothed data reveals a steady upward trend, indicating that resistance increases slightly over time. This trend likely results from microstructural changes within the 5x5 layered specimen, such as microcracking or slight separations between layers, which increase resistance with each cycle. The interval between 600 and 800 seconds, the percentage resistance change fluctuates between 25% and approximately 200%. This high amplitude suggests that the 5x5 layered specimen is highly sensitive to cyclic strain, as the additional layers enhance strain sensitivity by amplifying the material's response to deformation. The regularity of these peaks and troughs demonstrates a stable and repeatable cyclic response, essential for applications requiring consistent performance under repeated strain.

In the bottom row, representing the 5% strain test after a prior 10% strain test, the resistance data exhibits a more stable baseline with minimal upward drift compared to the baseline test. The raw data shows cyclic fluctuations, while the smoothed data indicates a steady baseline without significant increases over time. This stability suggests that the initial 10% strain may have "settled" the specimen's structure, leading to a more stable configuration. This effect could be due to the realignment of conductive pathways or closure of microcracks, reducing the likelihood of additional resistance changes in subsequent cycles. In the 600 to 800-second interval, the percentage resistance change oscillates between 0% and around 175%, slightly lower than in the baseline test. This reduced amplitude may indicate a decrease in sensitivity after exposure to the higher 10% strain, possibly due to microstructural stabilization that limits further deformation under the lower 5% strain.

When comparing the two tests, the baseline 5% strain test shows a gradual baseline drift, which suggests progressive structural changes in the specimen under cyclic loading. Conversely, the specimen subjected to 5% strain after an initial 10% strain exhibits a more stable baseline, suggesting that the previous exposure to higher strain may have stabilized the structure, reducing further resistance drift. Additionally, the baseline test shows a higher amplitude in resistance change (around 200%), while the 5% strain test following the 10% strain test displays a reduced peak (approximately 175%). This difference implies a form of structural adaptation or strain hardening,

where the specimen becomes less responsive to subsequent cyclic strain after higher strain exposure.

Figure 3.10 presents typical resistance data for two 4x5-layered line sensors subjected to 100 cycles at 10% strain. The top row shows data from a baseline test conducted at 10% strain, while the bottom row displays measurements taken at 10% strain following an initial test at 5% strain. Each row includes plots of resistance over time (left) and percentage resistance change over a focused interval between 600 and 800 seconds (right).

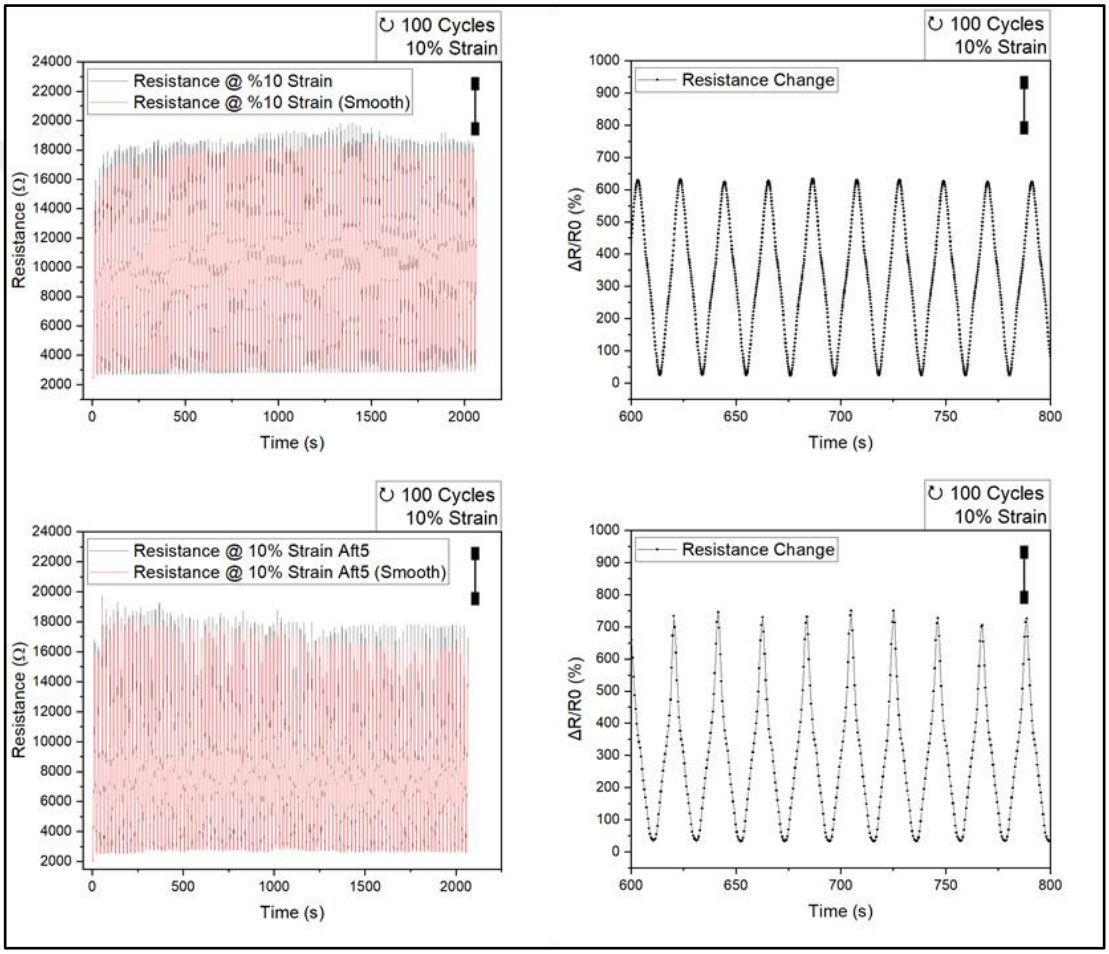

Figure 3.10 : Cyclic behaviors of 4x5 line sensors of 10% strain.

In the baseline 10% strain test (top row), the resistance data exhibits cyclic fluctuations with a gradual upward trend in baseline resistance over time. The raw data captures detailed variations due to cyclic loading, while the smoothed data highlights this subtle upward drift. This progressive increase in baseline resistance likely indicates structural changes within the 4x5-layered specimen, such as microcracking or slight separation

between layers, typically occurring in multi-layered conductive materials under repeated cyclic stress.

The percentage resistance change in the baseline test shows fluctuations ranging from approximately 0% to 650%, indicating high sensitivity to cyclic strain. The consistent peaks and troughs across cycles suggest stable and repeatable performance, an important characteristic for sensors undergoing repetitive loading. The regularity of these cyclic responses suggests that the specimen maintains a resilient response to each load cycle despite the gradual increase in baseline resistance.

For the second test (bottom row), where the specimen was subjected to 10% strain following an initial 5% strain test, the resistance data again shows cyclic fluctuations. However, the baseline appears more stable with minimal upward drift compared to the baseline test. The smoothed data confirms this stabilization, suggesting that the initial 5% strain may have conditioned the specimen's structure, reducing the likelihood of additional microstructural changes under the subsequent 10% strain cycles. This stabilization could result from the realignment of conductive pathways or the closure of minor defects formed during the initial strain cycle.

In the interval between 600 and 800 seconds, the percentage resistance change ranges from 0% to approximately 750%, higher than the 650% observed in the baseline test. This suggests an increased response to cyclic loading after pre-straining, potentially due to structural adjustments within the sensor material. Notably, data points in this interval are less frequent than in previous measurements, indicating a possible reduction in sensitivity due to the altered strain history. The impact of pre-straining is evident, as it modifies the sensor's response in multiple ways, including smoothing fluctuations and altering peak resistance levels. More detailed analyses, such as scanning electron microscopy (SEM) and tests with larger sample sizes, are necessary for this type of sensor to assess these effects thoroughly.

When comparing both tests, the baseline 10% strain test shows a gradual increase in baseline resistance over time, suggesting progressive microstructural changes under cyclic loading. In contrast, the 10% strain test conducted after an initial 5% strain exposure shows a more stable baseline resistance, likely due to stabilization effects from the prior lower strain exposure. Additionally, the baseline test exhibits a lower amplitude of resistance change, reaching up to 650%, while the post-5% strain test

shows an increased peak of approximately 750%. This difference suggests that after the initial 5% strain, the sensor becomes slightly less sensitive to cyclic loading at 10% strain. This reduced sensitivity may result from microstructural adjustments that limit further deformation, enhancing stability but potentially reducing the sensor's dynamic response.

Figure 3.11 depicts the cyclic behavior of 5x5-layered line sensors subjected to 100 cycles at 10% strain. The top row represents a baseline test conducted at 10% strain, while the bottom row shows data for a 10% strain test performed after an initial exposure to 5% strain. Each row includes plots of resistance over time (left) and percentage resistance change over a focused interval between 600 and 800 seconds (right).

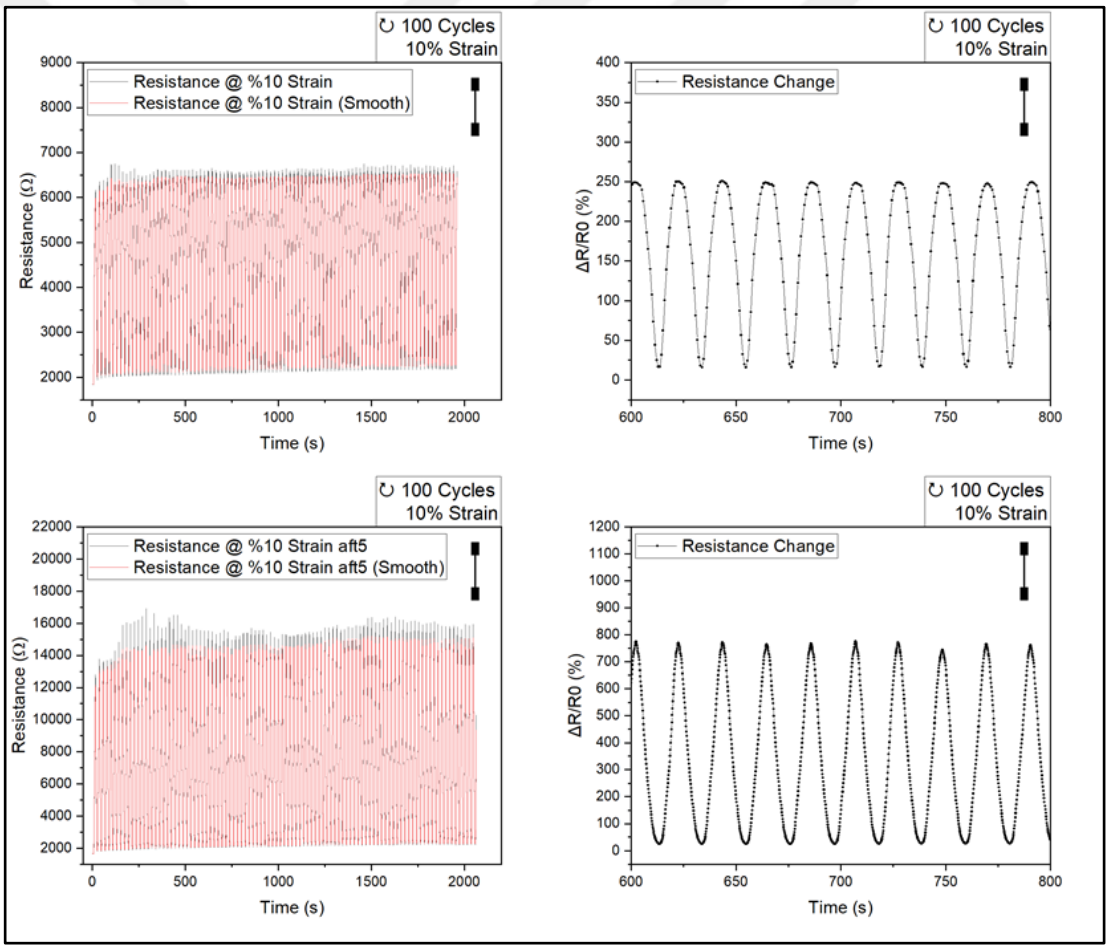

Figure 3.11 : Cyclic behaviors of 5x5 layers line sensors of 10% strain.

In the baseline 10% strain test (top row), the resistance data reveals cyclic fluctuations accompanied by a gradual increase in baseline resistance over time. The raw data captures these fluctuations, while the smoothed data shows a steady upward drift in

baseline resistance. This increase likely reflects structural changes within the 5x5-layered specimen, possibly due to microcracking or separation between conductive layers under repeated loading. Such changes are characteristic of multi-layered conductive structures, where repeated cyclic stress progressively weakens conductive pathways.

The percentage resistance change for this baseline test fluctuates between 10% and approximately 250% across each cycle, indicating high sensitivity to cyclic strain. The regularity of the peaks and troughs demonstrates stable and repeatable cyclic performance, which is critical for sensors used in repetitive loading applications. The consistent amplitude in resistance change suggests that the 5x5-layered sensor maintains its sensitivity over the test duration, responding reliably to each cycle.

In the second test (bottom row), where the specimen was subjected to 10% strain following a prior 5% strain exposure, the resistance data again shows cyclic fluctuations but with a more stable baseline and minimal upward drift compared to the baseline test. The smoothed data confirms this stabilized baseline, indicating that the initial 5% strain may have conditioned the specimen's structure, reducing the likelihood of additional structural changes during subsequent 10% strain cycles. This stabilization effect may be due to the realignment or reinforcement of conductive pathways due to the initial strain exposure.

In the focused interval between 600 and 800 seconds, the percentage resistance change ranges from 0% to approximately 800%, significantly higher than the 250% observed in the baseline test. This increase in amplitude suggests that the sensor's sensitivity may have been enhanced by the initial 5% strain, possibly due to structural adaptations that rendered the conductive pathways more susceptible to deformation under higher strain. The consistent cyclic peaks and troughs in this test indicate a stable response to each cycle, albeit with an increased amplitude in resistance change.

Comparing the two tests, the baseline test at 10% strain exhibits a gradual increase in baseline resistance, which suggests progressive structural changes within the 5x5-layered specimen under cyclic loading. In contrast, the 10% strain test following 5% strain exposure shows a more stable baseline, likely due to structural adaptation from the initial lower strain. Furthermore, the baseline test displays a maximum resistance change of around 250%, whereas the test following 5% strain reaches approximately

800%. This substantial increase in sensitivity implies that the initial 5% strain conditioned the specimen, enhancing its response to subsequent higher strain levels. This conditioning effect may have made the sensor more responsive to deformation due to increased flexibility in the conductive pathways.

Table 3.6 presents GFs for 4x5 and 5x5 layered line sensors under different strain levels, providing insights into the impact of layer count and strain level on sensor sensitivity without considering the pre-straining effects.

Table 3.6 : GFs per different strain levels between 4x5 and 5x5 layers.

Sensor	Max Layer	Strain Level	Mean GF	Std GF	#
Line 	4	5%	29.76	19.03	5
		10%	38.79	21.26	5
	5	5%	59.63	37.16	5
		10%	68.83	65.52	4

Firstly, the data indicates that increasing the number of layers enhances sensor sensitivity, as evidenced by the higher mean GF values in the 5x5 configuration compared to the 4x5 configuration at both 5% and 10% strain levels. This result aligns with the theoretical expectation that additional conductive layers expand the network of conductive pathways, thereby enabling a more substantial change in resistance under applied strain.

Secondly, the effect of strain level on GF is evident. Both configurations exhibit an increase in mean GF when the strain is raised from 5% to 10%, suggesting that higher strain levels amplify the sensor's sensitivity. This trend is consistent with the behavior of strain-sensitive materials, where increased deformation often results in greater resistance changes due to structural shifts within the material.

However, the data also reveals a trade-off in terms of stability. The standard deviation (Std GF) values are considerably higher for the 5x5 layered sensor, especially at 10% strain, where the standard deviation nearly matches the mean GF (65.52 vs. 68.83). This high variability indicates that, while the 5x5 configuration offers enhanced sensitivity, it may be less stable and exhibit greater inconsistency under higher strain levels. This variability could stem from microstructural instabilities or increased susceptibility to alignment issues and microcracking, which tend to become more pronounced with additional layers and elevated strain.

In conclusion, the 4x5 and 5x5-layered line sensors exhibit high sensitivity and stable cyclic behavior under 10% strain, each suited to specific applications. The 4x5 sensors show consistent cyclic peaks and improved baseline stability after an initial 5% strain, indicating enhanced long-term stability with a slight sensitivity trade-off, making them ideal for applications requiring predictable, reliable responses.

The 5x5-layered sensors, while exhibiting stable cyclic behavior, show an increased sensitivity to strain, especially following prior exposure to a 5% strain. This prior conditioning appears to "prime" the sensor, resulting in heightened sensitivity and a greater amplitude of resistance change under subsequent 10% strain cycles. This increased sensitivity is likely due to additional percolation pathways created by the extra layers, amplifying the response to mechanical deformation. Such behavior could be advantageous for applications requiring heightened sensitivity, particularly after an initial settling phase. However, this increased sensitivity also brings higher variability, suggesting that the 5x5 configuration is more suitable for applications prioritizing sensitivity over absolute consistency.

These findings highlight the influence of prior loading history on the performance and durability of multi-layered sensors under cyclic loading. Further research with larger sample sizes, extended cyclic testing, and detailed imaging analyses could deepen understanding of wear mechanisms. Initial 10% strain on 5x5-layered sensors appears to stabilize their structure, reducing variability at lower strain levels, which benefits dynamic applications requiring both sensitivity and stability. While the 4x5 configuration offers consistent performance, the 5x5 design's adaptable sensitivity makes it ideal for strain-sensitive tasks like respiration monitoring.

3.4.2 Serpentine

This section analyzes the performance of serpentine sensors, a geometry that differs from line sensors by incorporating curves in the electron pathway. These curves may slightly reduce directional strain sensitivity. However, the serpentine design effectively captures forces from multiple directions, making it a suitable alternative for wearable textile-based respiration sensors. This improved responsiveness to multidirectional forces enhances the sensor’s ability to accurately capture respiratory movements.

3.4.2.1 The effect of printing quality on the sensor performance

The images in Figure 3.12 showcase the printing performance of a graphene ink-based serpentine sensor, highlighting the progression from Layer 1 (L1) to Layer 5 (L5).

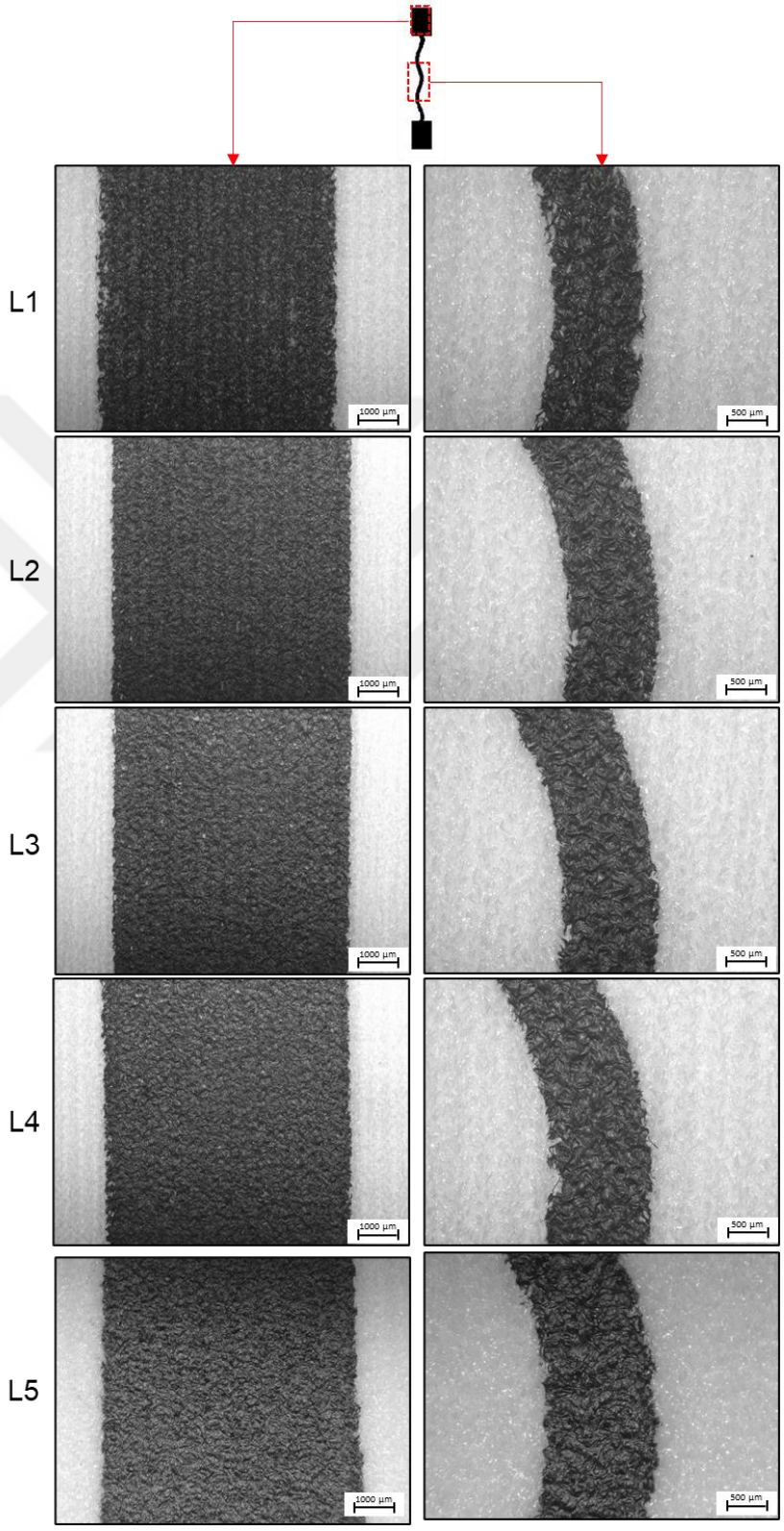

Figure 3.12 : Figures from serpentine sensor, layer 1 to layer 5 (randomly taken).

These images offer insights into the consistency and quality of the printed layers, which are key to determining the sensor's electrical and mechanical performance on a textile substrate.

Overall, the graphene ink application exhibits consistent uniformity across the layers, though slight variations in thickness and edge definition are observed. This consistency is crucial for maintaining stable resistance values across the sensor's surface. In the initial layers (L1 and L2), the ink coverage is dense with minimal gaps, providing a solid conductive pathway. This dense initial adhesion is important for wearable applications, where movement and flexing can disrupt weaker bonds.

With the addition of layers (L3 through L5), there is a gradual increase in texture and potential roughness at the edges, especially within the serpentine curves. This suggests a buildup of material that might introduce minor inconsistencies in conductivity, as irregularities can lead to localized variations in electrical resistance. Moreover, the images highlight the challenges of precision in printing curved structures of the serpentine pattern, as seen in the right column. The serpentine edges display slight spreading and roughness, potentially impacting the sensor's designed sensitivity to strain. This spreading could stem from the capillary action of the textile fibers and minor misalignments in successive layers, causing the ink to extend slightly beyond the intended pattern boundaries.

3.4.2.2 Analysis of IV curves

Table 3.7 presents the average resistance levels and standard deviations for 4x5-layered serpentine sensors under varying strain conditions and strain alteration sequences. The data encompasses resistance measurements at three strain levels—0%, 5%, and 10%—under different conditions, including initial baseline (bare) measurements and subsequent measurements taken after specific strain tests.

In the baseline or bare measurements, the average resistance for the sensor at 0% strain is 2.26 kΩ, which increases to 5.01 kΩ at 5% strain and further to 11.10 kΩ at 10% strain. The standard deviation remains relatively low at 0% (0.21 kΩ) and 5% strain (0.70 kΩ), suggesting consistent resistance values under these conditions. However, at 10% strain, the standard deviation rises to 2.71 kΩ, indicating greater variability in the sensor's response under higher strain levels, likely due to increased structural deformation.

Table 3.7 : Serpentine sensor resistance levels per IV curves (4x5).

Max Layer	Strain Level	Strain Alteration	Avg. Resistance (kΩ)	St. Deviation (kΩ)	#
4	0%	Bare	2.26	0.21	5
	5%	Bare	5.01	0.70	4
	10%	Bare	11.10	2.71	2
	0%	Post 5%	2.39	0.14	3
	5%	Post 5%	6.30	2.09	3
	10%	Post 5%	14.33	6.81	3
	0%	Post 10%	2.77	0.34	2
	5%	Post 10%	8.84	2.49	2
	10%	Post 10%	22.54	-	1
	0%	Post 5% (Post 10%)	2.54	0.31	2
	5%	Post 5% (Post 10%)	8.82	1.67	2
	10%	Post 5% (Post 10%)	17.20	4.46	2
	0%	Post 10% (Post 5%)	2.64	0.37	3
	5%	Post 10% (Post 5%)	10.22	1.18	3
	10%	Post 10% (Post 5%)	18.27	6.47	3

Following a 5% strain test, the resistance at 0% strain decreases slightly to 2.39 kΩ with a low standard deviation of 0.14 kΩ, implying minimal impact on the sensor's baseline resistance. At 5% strain, the resistance increases to 6.30 kΩ, with a moderate standard deviation of 2.09 kΩ. At 10% strain, the resistance reaches 14.33 kΩ with a standard deviation of 6.81 kΩ, indicating that variability increases as strain intensifies.

When a 10% strain test is performed prior to subsequent measurements, the resistance at 0% strain increases to 2.77 kΩ, slightly higher than both the bare and post-5% test values, indicating some structural impact on the sensor's baseline condition. For 5% strain, the resistance reaches 8.84 kΩ with a standard deviation of 2.49 kΩ, while at 10% strain, the resistance significantly increases to 22.54 kΩ. As this measurement was taken only once, a standard deviation could not be calculated, but the substantial increase in resistance following high strain exposure suggests that previous high strain levels impact the sensor's electrical behavior.

Under more complex testing conditions, where resistance is measured after sequential strain levels, the resistance values exhibit varied responses. For instance, at 5% strain following an initial 10% test, the resistance is 8.82 kΩ with a standard deviation of

1.67 kΩ. However, 5% strain post 10% and post 5% straining show a decrease in variability. This could mean that values gathered around an average, showing stability. These sequential testing conditions highlight the influence of strain history on resistance behavior, generally resulting in increased resistance and greater variability. It must be highlighted that the coefficient of variation (CV), which is calculated as the ratio of the standard deviation to the mean, is still quite low for 4x5 measurements.

Table 3.8 summarizes the average resistance levels and standard deviations for 5x5-layered serpentine sensors under various strain conditions and strain alteration sequences. This data includes resistance measurements at strain levels of 0%, 5%, and 10%, taken under baseline (bare) conditions and after specific strain tests, to analyze how previous strain affects the sensor's electrical characteristics.

Table 3.8 : Serpentine sensor resistance levels per IV curves (5x5).

Max Layer	Strain Level	Strain Alteration	Avg. Resistance (kΩ)	St. Deviation (kΩ)	#
5	0%	Bare	1.92	0.70	5
	5%	Bare	3.75	1.16	5
	10%	Bare	6.30	0.59	2
	0%	Post 5%	2.05	0.76	3
	5%	Post 5%	5.31	0.41	2
	10%	Post 5%	7.70	0.89	3
	0%	Post 10%	2.18	0.15	2
	5%	Post 10%	6.19	0.60	2
	10%	Post 10%	9.92	-	1
	0%	Post 5% (Post 10%)	2.10	0.42	2
	5%	Post 5% (Post 10%)	6.24	0.56	2
	10%	Post 5% (Post 10%)	8.29	2.33	2
	0%	Post 10% (Post 5%)	2.45	0.69	3
	5%	Post 10% (Post 5%)	7.94	2.50	3
	10%	Post 10% (Post 5%)	18.15	4.69	3

In the baseline (bare) measurements, the average resistance at 0% strain is recorded as 1.92 kΩ, increasing to 3.75 kΩ at 5% strain and further to 6.30 kΩ at 10% strain. The standard deviations for these measurements are relatively low, with values of 0.70 kΩ,

1.16 kΩ, and 0.59 kΩ, respectively, indicating generally consistent performance across samples without prior strain.

After an initial 5% strain test, the resistance at 0% strain is recorded as 2.05 kΩ, nearly identical to the bare condition, implying minimal impact on baseline resistance. At 5% strain, the resistance is 5.31 kΩ, though a minimal standard deviation of 0.41. At 10% strain, the resistance reaches 7.70 kΩ with a standard deviation of 0.89 kΩ, indicating slightly increased variability, nonetheless consistent.

In cases with sequential strain testing (e.g., testing at 5% after a 10% strain test), resistance values vary, but not to a great extent, except for 10% strain, reflecting the influence of strain history. For example, after performing a 5% and a 10% test, resistance at 0% is 2.45 kΩ with a standard deviation of 0.69 kΩ. Checking all resistance values at rest, all values are quite similar. Likewise, 0% and 5% strain values are also similar in post-testing configuration. This might mean that in moderate strain levels, sensor microcrack formation is well settled. At 10% strain after multiple previous tests, resistance reaches up to 18.15 kΩ with a standard deviation of 4.69 kΩ, showing that cumulative strain exposure impacts both resistance levels and variability. In addition, this can be commented on as serpentine geometry is still adapting to higher strains and longer durations.

The IV curves presented in Figure 3.13 provide a comparison of the electrical performance of 4x5 layered and 5-layered serpentine sensors under different strain conditions. The left column illustrates the response of the 4x5 layered sensor, while the right column shows the 5-layered sensor. The rows represent the sensor states: resting, under 5% strain, and under 10% strain from top to bottom.

In the resting state, both the 4x5 layered and 5-layered sensors exhibit linear IV characteristics, with high R-squared values (0.99 for the 4x5 layered and 0.86 for the 5-layered), indicating stable and predictable current-voltage relationships in the absence of strain. The slope of the linear fit in the 5-layered sensor is slightly higher than in the 4x5 layered sensor, suggesting a marginally lower baseline resistance, possibly due to the additional conductive pathways introduced by the extra layer.

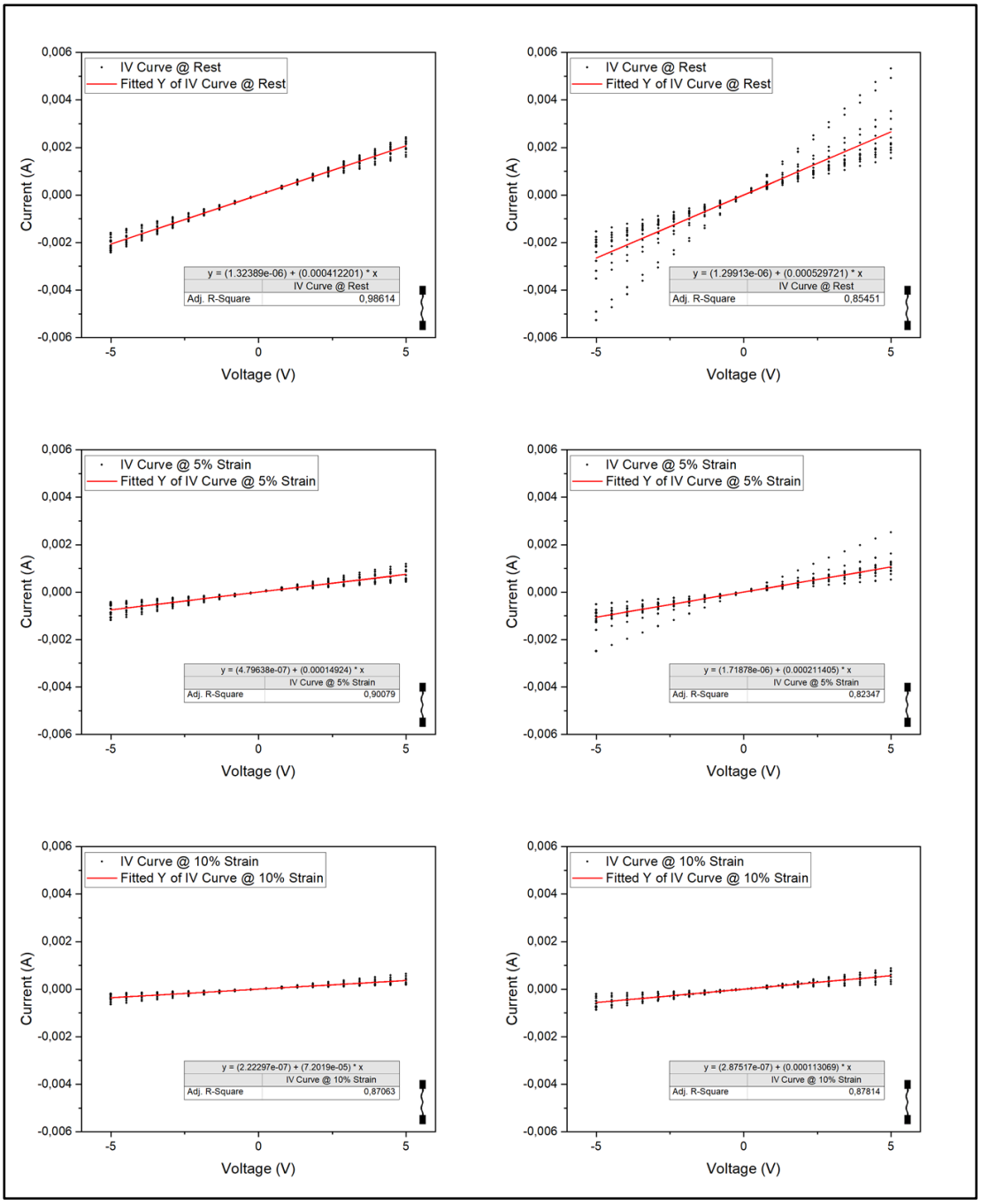

Figure 3.13 : IV measurements of serpentine sensors 4x5 (left), 5x5 (right).

Under 5% strain, both sensors maintain a linear response, but there is a noticeable difference in slope reduction. The 4x5 layered sensor's slope decreases less significantly than the 5-layered sensor, indicating a more stable resistance response under this strain level. The R-squared values drop slightly for both sensors; however, the 4x5 layered sensor retains a higher R-squared value (0.90) than the 5x5 layered sensor (0.82), suggesting that the 4x5 layered sensor displays more consistent performance with less deviation. The steeper reduction in slope for the 5x5 layered

sensor under 5% strain implies that it may be more sensitive to minor structural changes induced by strain, leading to increased resistance.

At 10% strain, both sensors show further reductions in slope, reflecting increased resistance due to the applied strain. This outcome is expected, as mechanical deformation generally disrupts conductive pathways, especially in flexible or layered materials. The 4x5 layered sensors maintain a relatively higher R-squared value (0.87). A similar is also observed for the 5x5 layered sensors (0.88), suggesting greater linearity and a more stable electron transport. The 5x5 layered sensor, however, exhibits a larger reduction in slope than the 4x5 layered sensor, highlighting its increased sensitivity to strain.

Table 3.9 presents an overview of the average resistance levels and standard deviations for serpentine sensors with 4 and 5 layers across different strain levels (0%, 5%, and 10%). This summary captures the general resistance characteristics of each configuration under varying strain conditions.

Table 3.9 : Overall resistance levels per IV curves.

Sensor	Max Layer	Strain Level	Avg. Resistance (kΩ)	St. Deviation (kΩ)	#
Serpentine 	4	0%	2.43	0.31	15
		5%	7.50	2.46	14
		10%	16.08	5.90	11
	5	0%	2.14	0.64	15
		5%	5.57	2.10	14
		10%	10.60	5.39	11

For the 4x5 layer serpentine sensor, the average resistance at 0% strain is 2.43 kΩ with a low standard deviation of 0.31 kΩ, indicating high consistency across the 15 measurements. At 5% strain, the resistance increases to 7.50 kΩ, accompanied by a standard deviation of 2.46 kΩ over 14 measurements, suggesting an increase in resistance with moderate variability. At 10% strain, the average resistance reaches 16.08 kΩ with a standard deviation of 5.90 kΩ across 11 measurements, reflecting a gradual increase in variability as strain levels rise.

For the 5-layer serpentine sensor, the average resistance at 0% strain is 2.14 kΩ, with a standard deviation of 0.64 kΩ based on 15 measurements, indicating slightly greater variability compared to the 4x5 layer configuration but with a slight decrease in

resistance as well. At 5% strain, resistance increases to 5.57 kΩ, with a standard deviation of 2.10 kΩ over 14 measurements, showing a rise in both resistance and variability, however smaller compared to its 4x5 layered counterpart. At 10% strain, the resistance further rises to 10.60 kΩ, with a standard deviation of 5.39 kΩ across 11 measurements, indicating that variability continues to increase significantly with strain.

These findings suggest that while both configurations respond effectively to strain, the 4x5 layered configuration offers higher sensitivity, as evidenced by the larger increase in resistance with strain. However, the 4x5 layer sensors exhibit consistently low variability across all strain levels, indicating stable performance under repeated testing. In contrast, the 5-layer sensors show higher variability, particularly at elevated strain levels, suggesting that the additional layer may introduce structural factors affecting measurement consistency under strain.

Overall, these observations underscore the trade-off between sensitivity and stability in serpentine sensors with varying layer counts. Further studies, such as fatigue testing and SEM analysis, could provide deeper insights into the microstructural mechanisms behind the observed differences, enhancing our understanding of the durability and reliability of multi-layered serpentine sensors under prolonged cyclic strain.

3.4.2.3 Cyclic test analysis

Table 3.10 summarizes the GFs of 4x5 layer and 5x5 layer serpentine sensors under different strain conditions and strain alteration sequences. This table provides the mean GF values and their standard deviations for various testing scenarios, allowing for an assessment of how prior strain exposure impacts sensor sensitivity.

For the 4-layer configuration, the GF at 5% strain without prior pre-straining (bare condition) is 15.78, with a low standard deviation of 0.67, suggesting stable sensitivity. At 10% strain, the GF rises significantly to 49.59, with a higher standard deviation of 22.87, indicating increased variability likely due to structural adaptations within the sensor material under higher strain.

When the 4x5 layer sensor is subjected to a 5% strain test following a prior 10% strain (Post 10% Test), the GF at 5% strain increases to 37.88, suggesting a conditioning effect from the previous high strain. Similarly, after a prior 5% strain (Post 5% Test), the GF at 10% strain reaches 59.84 with an elevated standard deviation, reflecting an

adaptation to the pre-straining that may lead to greater sensitivity but also more variability.

Table 3.10 : GFs per different strain alterations measurements.

Sensor	Max Layer	Test	Strain Alteration	Mean GF	Std GF	#
Serpentine 	4	5%	Bare	15.78	0.67	3
		10%	Bare	49.59	22.87	3
		5%	Post 10% Test	37.88	7.58	3
		10%	Post 5% Test	59.84	30.51	3
	5	5%	Bare	16.92	7.92	2
		10%	Bare	27.98	18.16	2
		5%	Post 10% Test	28.18	7.39	2
		10%	Post 5% Test	57.49	22.65	2

For the 5x5 layer configuration, the bare 5% strain GF is 16.92, increasing to 27.98 at 10% strain, showing a similar trend of heightened sensitivity with increased strain. However, when subjected to a 5% strain test following a prior 10% strain (Post 10% Test), the GF at 5% strain becomes 28.18, indicating an enhancement in sensitivity from pre-straining. Likewise, after a prior 5% strain (Post 5% Test), the GF at 10% strain increases to 57.49, with a substantial rise in standard deviation, mirroring the pattern observed in the 4x5 layer configuration.

Overall, these results suggest that pre-straining has a conditioning effect on the sensor's GF, especially under higher strain levels. The variability introduced by pre-straining, as seen in the higher standard deviations, points to potential microstructural adjustments that may enhance sensitivity but compromise measurement consistency. This highlights the importance of considering strain history in applications that demand precise and consistent sensor responses, as pre-straining may alter the sensor's baseline characteristics. Further studies could involve SEM analysis to examine these microstructural changes and assess their implications for long-term stability and durability under cyclic loading.

Figure 3.14 presents the cyclic behavior of 4x5-layered serpentine sensors subjected to 100 cycles at 5% strain. The top row illustrates the baseline measurements taken at 5% strain, while the bottom row shows measurements taken at 5% strain following an initial exposure to 10% strain. Each row includes plots of resistance over time (left)

and percentage resistance change over a focused interval from 600 to 800 seconds (right).

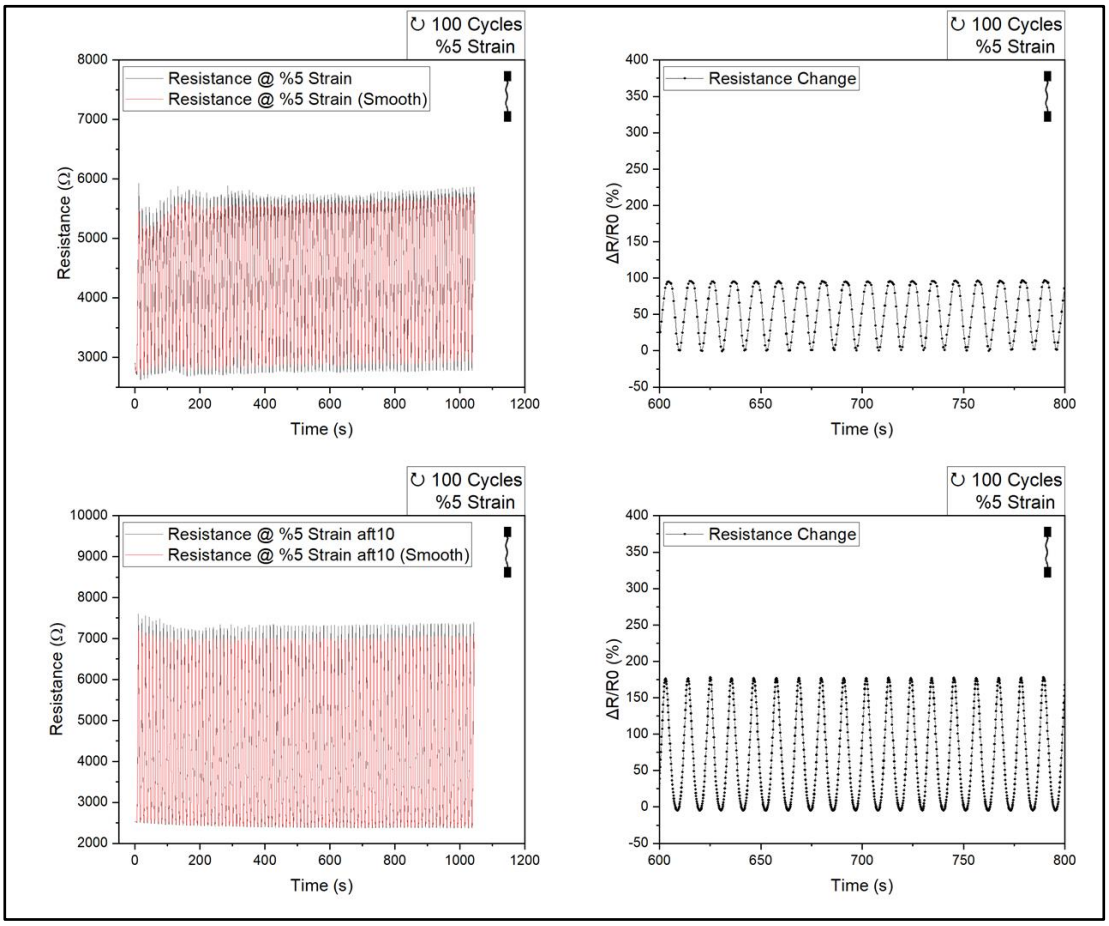

Figure 3.14 : Cyclic behaviors of serpentine sensors of 5% strain level, for 4x5 layers.

In the baseline 5% strain test (top row), the resistance data demonstrates cyclic fluctuations with a stable baseline. The raw data captures the detailed variations due to cyclic loading, while the smoothed data shows an overall consistent baseline with no significant drift, indicating that the sensor's response remains stable under repeated 5% strain cycles. This stability in baseline resistance suggests that the sensor maintains structural integrity without exhibiting notable fatigue-related changes.

The percentage resistance change during the baseline test oscillates between approximately 0% and 100%, indicating high sensitivity to cyclic loading at 5% strain. The regularity of the peaks and troughs in the response suggests a repeatable cyclic performance, a crucial feature for applications requiring stable sensor output under repetitive loading.

In the 5% strain test following an initial 10% strain exposure (bottom row), the resistance data exhibits similar cyclic fluctuations to the baseline test but with a slightly higher baseline resistance. The smoothed data reveals minimal drift, indicating that the previous 10% strain exposure may have marginally affected the sensor's structure, leading to a small increase in baseline resistance. However, the stability of this baseline after the 10% strain test suggests that the sensor's structural adaptations have minimized further drift under subsequent 5% strain cycles, reflecting resilience to accumulated strain history.

The percentage resistance change in the post-10% strain test oscillates between 0% and approximately 175% compared to the baseline test. This consistency in amplitude indicates that the sensor's sensitivity to 5% strain increased by prior exposure to a higher strain level. The regular pattern of response suggests that the internal structure of the sensor is settled, which is mostly seen in other examples as well.

The consistency in percentage resistance change between the baseline and post-10% strain tests suggests that the sensor's sensitivity to 5% strain remains stable, regardless of prior strain exposure. The repeatable response peaks at around 175%, which indicates that the sensor can reliably track cyclic strain, making it suitable for applications requiring dependable performance under repetitive loading.

Figure 3.15 shows the cyclic behavior of 4x5-layered serpentine sensors subjected to 100 cycles at 10% strain. The top row illustrates baseline measurements taken at 10% strain, while the bottom row displays measurements taken at 10% strain following an initial exposure to 5% strain. Each row includes plots of resistance over time on the left and percentage resistance change over a focused interval between 600 and 800 seconds on the right.

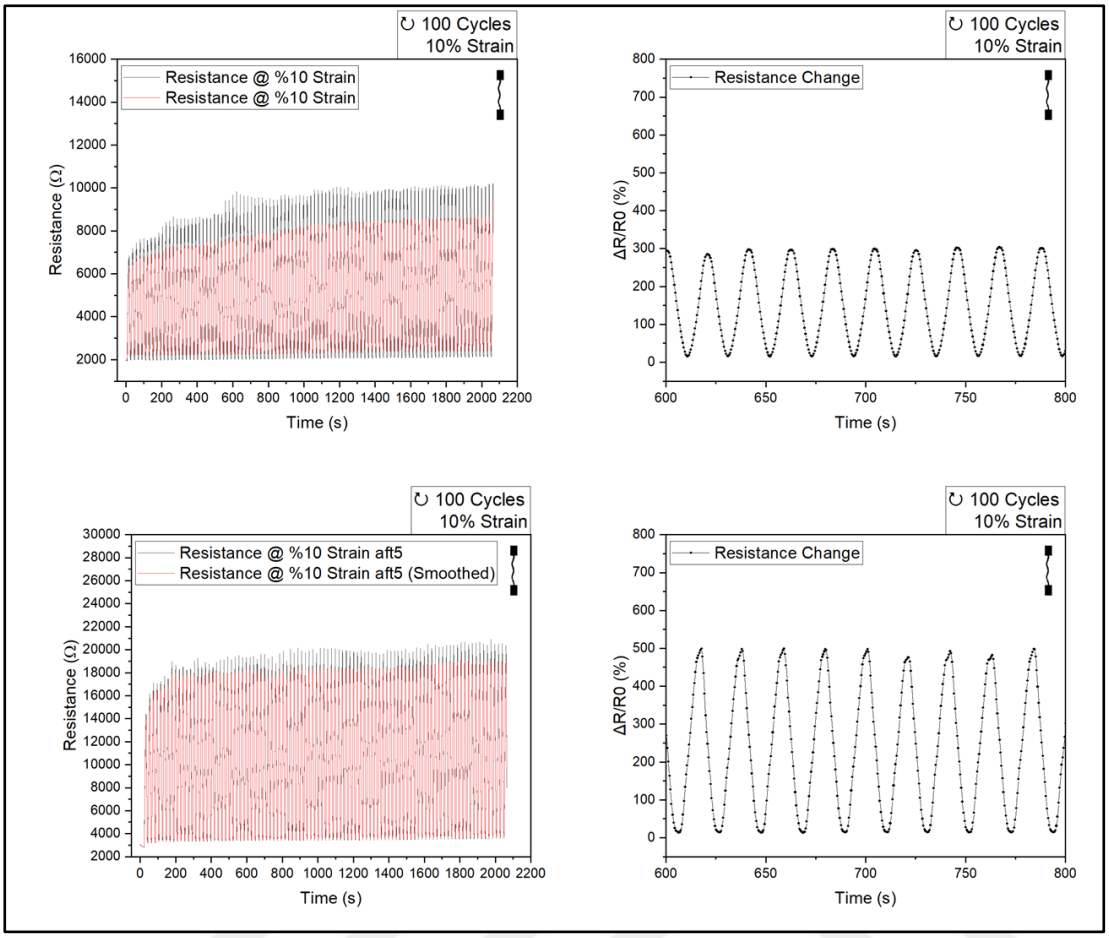

Figure 3.15 : Cyclic behaviors of 4x5 serpentine sensors of 10% strain level.

In the baseline 10% strain test presented in the top row, the resistance data shows cyclic fluctuations with a gradual increase in the baseline over time. The raw data highlights the detailed resistance variations due to cyclic loading, while the smoothed data reveals an upward drift in baseline resistance, suggesting a cumulative structural impact from repeated 10% strain cycles. The percentage resistance change oscillates between 0% and approximately 300%, indicating high sensitivity to the cyclic loading. The regularity of these fluctuations suggests that the sensor maintains a cyclic response, though the baseline drift implies potential structural changes over time.

In the test conducted at 10% strain following an initial 5% strain exposure, shown in the bottom row, the resistance data continues to exhibit cyclic behavior with a noticeable increase in baseline resistance compared to the baseline test. The smoothed data reveals that the baseline resistance is stabilized after prior 5% strain exposure, suggesting that the initial strain history may have induced structural adaptations. The percentage resistance increased, making the sensor more sensitive to loading.

The baseline and post-5% strain test results reveal consistent cyclic behavior with slight baseline drift, particularly more pronounced in the post-5% strain test. The consistent peaks in percentage resistance change across both conditions suggest that the sensor maintains stable sensitivity at 10% strain despite strain history. However, the gradual increase in baseline resistance indicates potential structural changes under sustained high-strain conditions, which may impact long-term stability.

Figure 3.16 illustrates the cyclic behavior of 5x5-layered serpentine sensors subjected to 100 cycles at 5% strain. The top row represents baseline measurements taken at 5% strain, while the bottom row shows measurements taken at 5% strain following an initial exposure to 10% strain. Each row includes plots of resistance over time on the left and percentage resistance change over a focused interval from 600 to 800 seconds on the right.

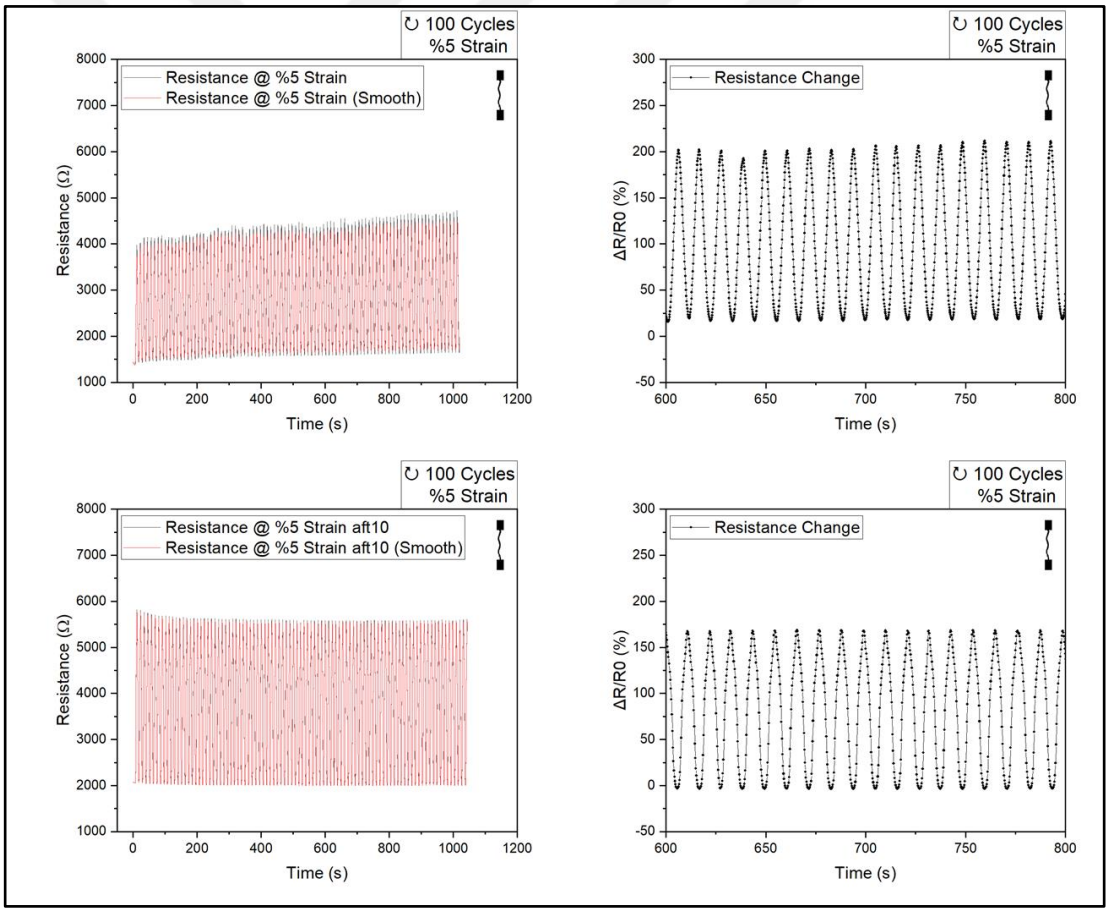

Figure 3.16 : Cyclic behaviors of serpentine sensors of 5% strain level, for 5x5 layers.

In the baseline 5% strain test shown in the top row, the resistance data exhibits cyclic fluctuations with a stable baseline. The raw data captures detailed variations resulting

from cyclic loading, while the smoothed data reveals an overall consistent baseline, indicating that the sensor maintains stability under repeated 5% strain cycles, albeit with a slightly increasing trend. The percentage resistance change oscillates between approximately 20% and 220%, demonstrating the sensor's sensitivity to cyclic loading at 5% strain. The regularity of peaks and troughs in the response suggests repeatable performance across cycles, an essential characteristic for applications that require consistent strain measurements.

In the test conducted at 5% strain following an initial 10% strain exposure, shown in the bottom row, the resistance data reveals a similar cyclic pattern to the baseline test, with minimal deviation in the baseline level. The flatness of the base resistance is typically observed in post-test modes. The percentage resistance change in this test also fluctuates consistently between 0% and 175%, matching the baseline test, which indicates that the sensor’s sensitivity to 5% strain remains stable despite the previous 10% strain exposure. The regular cyclic pattern suggests that the sensor maintains a reliable and consistent response under repeated strain cycles.

The baseline and post-10% strain test results demonstrate stable cyclic behavior with minimal baseline drift. The percentage resistance change is consistent between the two conditions, with peaks reaching approximately 200%, suggesting that prior strain exposure does not significantly affect the sensor's sensitivity at 5% strain. This consistency in performance indicates that the 5x5-layered serpentine sensor is resilient to the effects of strain history, maintaining reliability under repeated cyclic loading.

The observations in Figure 3.16 demonstrate that 5x5-layered serpentine sensors exhibit stable and repeatable cyclic behavior at 5% strain over 100 cycles, with minimal impact from prior 10% strain exposure. The sensor maintains consistent sensitivity, as evidenced by the uniform peaks in percentage resistance change, underscoring its suitability for applications requiring high repeatability and stability under cyclic loading conditions.

Figure 3.17 presents the cyclic behavior of 5x5-layered serpentine sensors subjected to 100 cycles at 10% strain. The top row shows baseline measurements taken at 10% strain, while the bottom row displays measurements at 10% strain following an initial exposure to 5% strain. Each row includes plots of resistance over time on the left and

percentage resistance change over a focused interval between 600 and 800 seconds on the right.

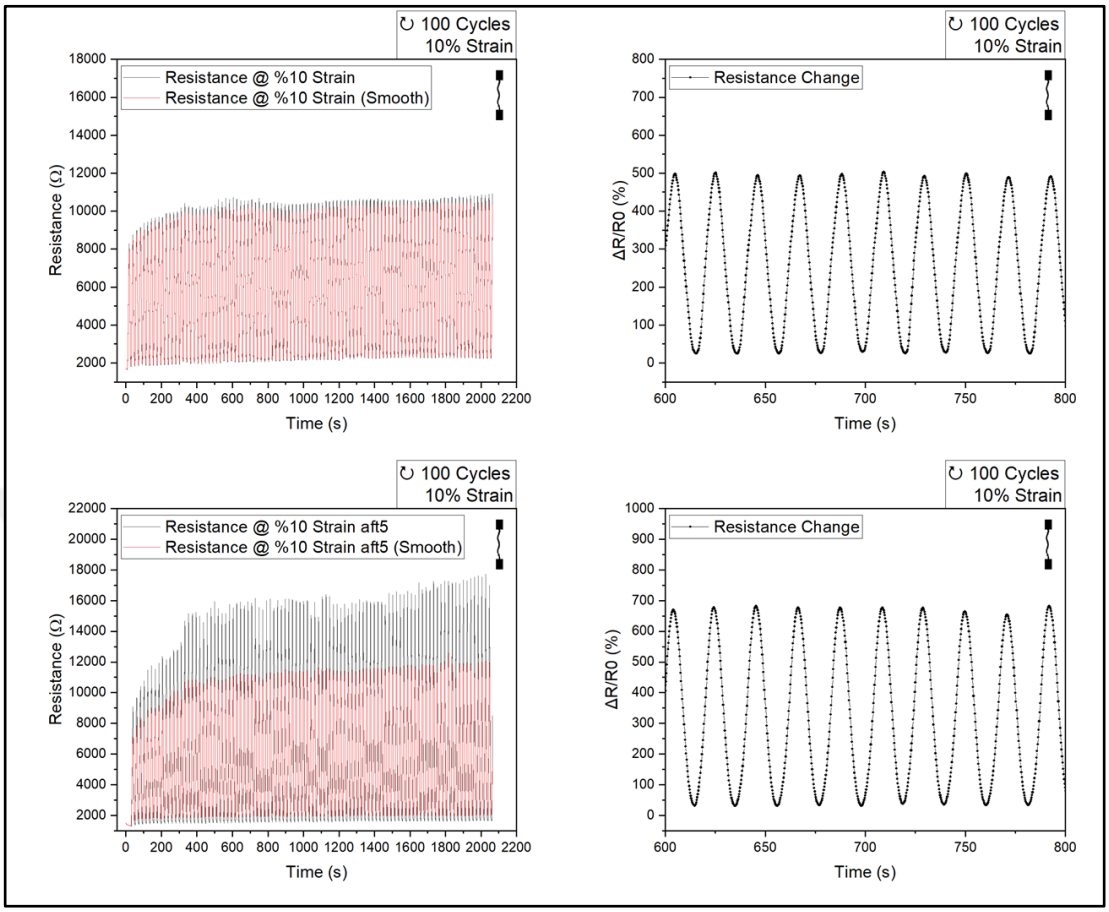

Figure 3.17 : Cyclic behaviors of serpentine sensors of 10% strain level, for 5x5 layers.

In the baseline 10% strain test, depicted in the top row, the resistance data reveals cyclic fluctuations with a gradual increase in the baseline over time. The raw data illustrates detailed resistance variations due to cyclic loading, while the smoothed data highlights a slight upward drift in baseline resistance. This drift suggests possible cumulative structural changes from repeated 10% strain cycles. The percentage resistance change oscillates consistently between 20% and approximately 500%, indicating the sensor's high sensitivity to cyclic loading at 10% strain.

In the test conducted at 10% strain following an initial 5% strain exposure, shown in the bottom row, the resistance data continues to exhibit cyclic behavior, with a flattened baseline resistance compared to the initial 10% strain test. An additional observation that may seem contrary to previous ones is that there is still an increasing trend in maximum resistance as the test continues. This highlights that the internal

structure is still not stabilized, possibly due to continuing microcrack generation. Thus, while pre-straining induces a stabilizing effect quite often, it cannot be generalized for all scenarios. The percentage resistance change remains consistent with the baseline test, fluctuating between 0% and approximately 700%, indicating the sensor's high sensitivity to 10% strain with previous exposure to 5% strain.

Table 3.11 provides the overall GFs for 4x5 layer and 5x5 layer serpentine sensors at strain levels of 5% and 10%. This summary includes the mean GF values, standard deviations, and the number of measurements taken for each configuration, offering insight into the sensitivity differences between the two sensor types across these strain conditions.

Table 3.11 : Overall GFs per different strain levels between 4x5 and 5x5 layers.

Sensor	Max Layer	Strain Level	Mean GF	Std GF	#
Serpentine 	4	5%	26.83	12.29	6
		10%	54.71	27.44	6
	5	5%	22.55	9.51	4
		10%	42.74	25.28	4

For the 4x5 layer configuration, the mean GF at 5% strain is 26.83, with a standard deviation of 12.29, indicating moderate sensitivity and variability. At 10% strain, the mean GF increases significantly to 54.71 with a higher standard deviation of 27.44. This increase in GF and variability suggests that the 4x5 layer configuration responds more sensitively to higher strain levels, likely due to greater deformation within the conductive pathways.

In comparison, the 5x5 layer configuration shows a lower mean GF of 22.55 at 5% strain, with a standard deviation of 9.51, implying a more stable but less sensitive response than the 4x5 layer configuration at the same strain level. At 10% strain, the mean GF rises to 42.74 with a standard deviation of 25.28, indicating increased sensitivity but with less variability than the 4x5 layer configuration at this strain level.

These results suggest that while both configurations exhibit increased sensitivity at higher strain levels, the 4x5 layer configuration demonstrates greater overall sensitivity but with higher variability. Conversely, the 5x5 layer configuration offers a more stable response with slightly lower sensitivity. This highlights a trade-off between sensitivity and stability based on layer count, with the 4x5 layer configuration

being suitable for applications requiring higher sensitivity and the 5x5 layer configuration for those needing more consistent readings. Further studies on strain level impacts and long-term stability under cyclic loading could deepen understanding of these configurations' suitability for different applications.

The study performed by E. Caffrey et al. highlights the relationship between network thickness versus gauge factor and other electrical and morphological properties depicted in Figure 3.18 and Figure 3.19 [113]. Under certain network thicknesses, GF is inversely related to percolation thickness. After a certain thickness, the study concludes that GF becomes independent of thickness. Amongst the measurements done, only serpentine sensor geometry fits this phenomenon. However, without advanced optical analysis, an increase in thickness – in this work, layer number - cannot be related to this conclusion. What is more, due to the screen printed ink amount being 30 mL for all geometries, where the line sensor has the lowest and strain gauge and omnidirectional sensors have higher surface areas, it can be assumed that the film thickness of the serpentine sensor is in between these geometries. Combined with the performance behavior of the other sensors, serpentine sensors, and other geometries are above the percolation network; hence, 4x5 and 5x5 layered sensors were not affected by network thickness based on the findings from the adapted study.

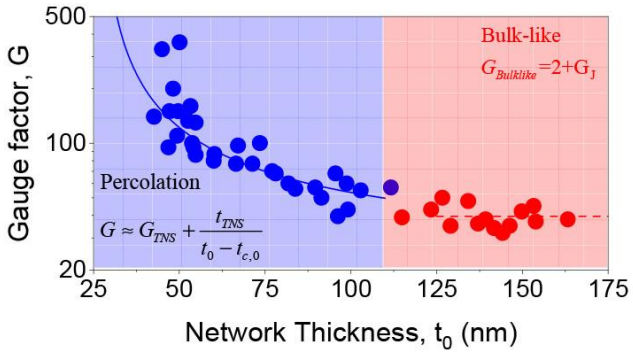

Figure 3.18 : GF vs network thickness (adapted from [113]).

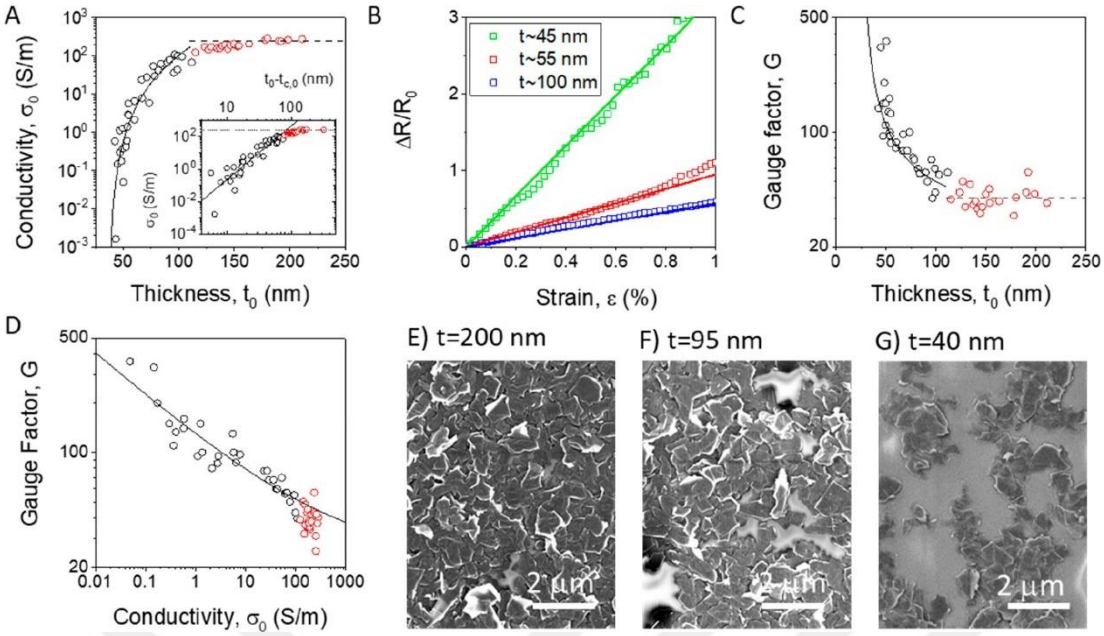

Figure 3.19 : Film thickness vs various quantitative and qualitative properties (adapted from [113]).

3.4.3 Strain Gauge

Strain gauge sensors are commonly used in various applications. The strain gauge design in this study consists of 12 lines, with the outermost lines being the longest. When the sensor is strained, all lines within the pattern are extended, resulting in a significant increase in the total conductive path length compared to other geometries. However, it should be noted that the length of each individual line is shorter than that of other sensor patterns.

The implementation of strain gauge sensors in specimen preparation presents challenges due to the higher likelihood of misalignment, which is attributed to the numerous lines that need to be precisely oriented in the direction of the applied force. Consequently, greater deviations between individual tests are anticipated.

3.4.3.1 The effect of printing quality on the sensor performance

The images in Figure 3.20 display the printing quality and consistency of graphene ink applied to a textile substrate for a strain gauge sensor. The left column shows the contact area, where the sensor interfaces with the external circuitry, while the right column presents the sensing area with the serpentine pattern responsible for strain detection. The images capture the progression from Layer 1 (L1) to Layer 5 (L5), illustrating how the printing quality evolves across successive layers.

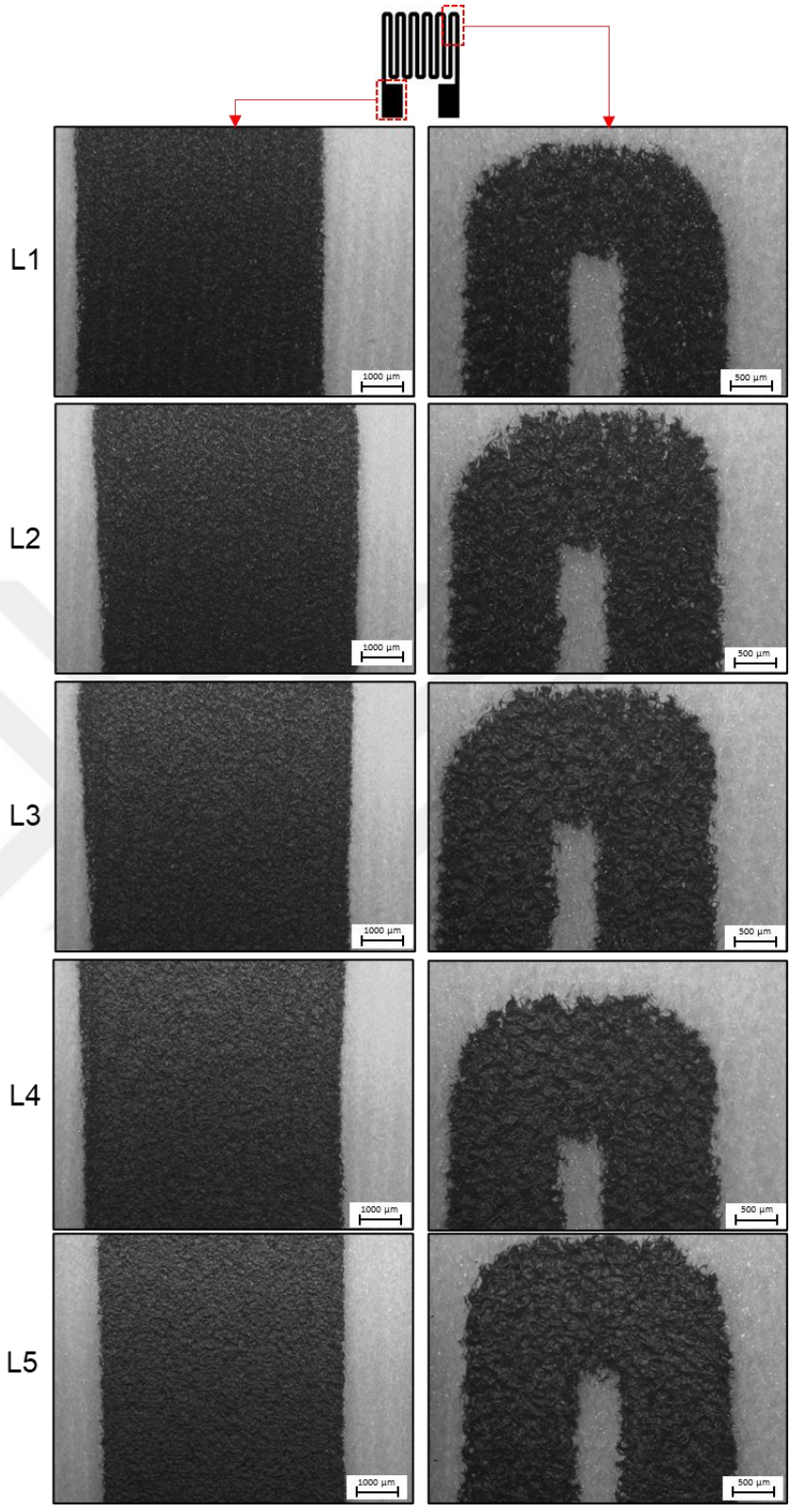

Figure 3.20 : Figures from strain gauge sensor. from layer 1 to layer 5 (randomly taken).

In the contact area (left column), the ink distribution appears dense and uniform across all layers, with minimal observable gaps or inconsistencies. This dense coverage is essential for establishing a stable electrical connection, ensuring that the contact area

maintains low resistance and reliable conductivity over time. The uniformity observed in these layers indicates effective adhesion of the graphene ink to the textile substrate, which is crucial in wearable applications where the sensor may be subjected to repeated stress and bending.

In the sensing area (right column), the serpentine pattern also shows relatively consistent ink coverage, though minor edge roughening and slight spreading are evident in the curved segments, particularly in the later layers (L4 and L5). This spreading effect may result from the interaction between the ink and the textile fibers, where capillary action encourages ink diffusion, especially in areas with tighter curves. Additionally, minor misalignments during successive layer applications may have contributed to a slight buildup of material along the edges, leading to the observed roughness. While these edge irregularities do not significantly compromise the structural integrity of the conductive path, they may introduce localized resistance variations, potentially affecting the precision of strain measurements.

The increased texture and roughness observed in the upper layers of both areas suggest that repeated applications may lead to cumulative effects in ink distribution, with each layer adding slight inconsistencies. For the sensing area, this could influence the sensor's sensitivity and stability under strain, as localized differences in conductivity might alter the intended electrical response. However, these irregularities are relatively minor, and the overall pattern retains its structural integrity across layers, which is encouraging for sensor durability.

In conclusion, the strain gauge sensor’s printing performance is generally consistent, with both the contact and sensing areas exhibiting good ink adhesion and boundary definition. The minor spreading in the sensing area highlights the importance of precise control over ink volume and alignment, particularly in applications where high sensitivity and stability are required.

3.4.3.2 Analysis of IV curves

Table 3.12 presents the resistance levels of 4x5-layered strain gauge sensors across different strain conditions and strain alteration histories. The table details the average resistance values, standard deviations, and the number of measurements for each scenario, providing insight into how strain levels and previous strain exposures influence sensor resistance.

Table 3.12 : Resistance levels of strain gauge sensor per IV curves (4x5).

Max Layer	Strain Level	Strain Alteration	Avg. Resistance (kΩ)	Std. Deviation (kΩ)	#
4	0%	Bare	12.13	2.98	5
	5%	Bare	15.64	5.29	5
	10%	Bare	21.00	5.25	2
	0%	Post 5%	11.96	3.24	3
	5%	Post 5%	15.15	5.05	3
	10%	Post 5%	22.15	9.44	3
	0%	Post 10%	14.51	1.31	2
	5%	Post 10%	20.69	4.05	2
	10%	Post 10%	26.17	8.13	2
	0%	Post 5% (Post 10%)	13.83	0.85	2
	5%	Post 5% (Post 10%)	19.26	2.60	2
	10%	Post 5% (Post 10%)	23.96	5.89	2
	0%	Post 10% (Post 5%)	12.80	3.89	3
	5%	Post 10% (Post 5%)	22.51	13.15	3
	10%	Post 10% (Post 5%)	35.00	24.15	3

In the baseline measurements (no prior strain), resistance values increase with strain. At 0% strain, the resistance is 12.13 kΩ with a standard deviation of 2.98 kΩ over five measurements. At 5% strain, resistance rises to 15.64 kΩ with a standard deviation of 5.29 kΩ, indicating higher variability. At 10% strain, resistance reaches 21.00 kΩ with a standard deviation of 5.25 kΩ, showing a steady increase in both resistance and variability with strain.

After a 5% strain test, subsequent measurements show similar patterns with slightly elevated resistance levels. For instance, at 0% strain after the 5% test, the resistance averages 11.96 kΩ with a standard deviation of 3.24 kΩ. At 5% strain following the 5% test, resistance is 15.15 kΩ with a standard deviation of 5.05 kΩ. At 10% strain after the 5% test, resistance reaches 22.15 kΩ with a high standard deviation of 9.44 kΩ, suggesting that previous strain exposure contributes to greater variability.

When sensors are tested following a 10% strain test, resistance increases significantly. For example, at 0% strain, the resistance is 13.83 kΩ with a low standard deviation of 0.85 kΩ. At 5% strain, resistance reaches 20.69 kΩ with a standard deviation of 4.05 kΩ, while at 10% strain, resistance increases to 26.17 kΩ with a standard deviation of

8.13 kΩ. These elevated values reflect the impact of the 10% strain history on the sensor's resistance, likely due to permanent structural changes.

Sequential testing, such as measurements taken at 5% strain after both 5% and 10% strain exposures, shows a continued increase in resistance. At 5% strain following both 5% and 10% tests, resistance averages 19.26 kΩ with a standard deviation of 2.60 kΩ. At 10% strain after these sequential exposures, resistance increases further to 23.96 kΩ with a standard deviation of 5.89 kΩ. Additional testing at 10% strain after both 5% and 10% strain tests yields a resistance of 35.00 kΩ with a high standard deviation of 24.15 kΩ, indicating substantial variability from accumulated strain effects.

Table 3.13 presents the resistance levels of 5x5-layered strain gauge sensors under various strain conditions and strain alteration sequences. The table reports the average resistance values, standard deviations, and the number of measurements for each condition, allowing analysis of how different strain levels and previous strain exposure influence sensor resistance.

Table 3.13 : Resistance levels per IV curves (5x5).

Max Layer	Strain Level	Strain Alteration	Avg. Resistance (kΩ)	Std. Deviation (kΩ)	#
5	0%	Bare	8.17	1.51	7
	5%	Bare	9.35	1.58	6
	10%	Bare	12.69	3.77	4
	0%	Post 5%	9.13	0.68	2
	5%	Post 5%	9.56	-	1
	10%	Post 5%	15.10	2.35	2
	0%	Post 10%	10.79	5.29	3
	5%	Post 10%	22.73	10.08	3
	10%	Post 10%	37.18	19.66	3
	0%	Post 5% (Post 10%)	11.20	5.79	3
	5%	Post 5% (Post 10%)	21.46	8.58	3
	10%	Post 5% (Post 10%)	32.22	17.30	3
	0%	Post 10% (Post 5%)	9.92	0.8	2
	5%	Post 10% (Post 5%)	14.69	1.42	2
	10%	Post 10% (Post 5%)	20.57	4.37	2

Under bare conditions, the resistance levels for this 5x5 configuration increase progressively with strain, from 8.17 kΩ at 0% strain to 12.69 kΩ at 10% strain, with a corresponding increase in standard deviation. This trend aligns with expected sensor behavior, where higher strain disrupts conductive pathways, leading to an increase in resistance. The increasing standard deviation at higher strain levels suggests that the variability of the sensor's response grows with deformation, possibly due to microstructural changes or wear in the material.

In the altered strain conditions (Post 5% and Post 10%), the resistance values and standard deviations provide evidence of structural adaptation within the sensor. For instance, after a 5% pre-strain, resistance at 5% strain (9.56 kΩ) remains relatively close to the bare condition at the same strain level, indicating minimal impact from prior loading. However, for the Post 10% condition, the resistance at 5% strain increases significantly to 22.73 kΩ, with a larger standard deviation (10.08 kΩ). This increase suggests that exposure to higher pre-strain levels induces a lasting structural effect that impacts the sensor's response to subsequent loading.

Notably, the highest resistance values and variability are observed under the cumulative condition of Post 5% (Post 10%) at 10% strain, reaching 20.57 kΩ with a standard deviation of 4.37 kΩ. This result indicates that multiple cycles of pre-strain introduce compounding effects on the sensor's structure, likely causing cumulative degradation or rearrangement of the conductive network. This sensitivity to strain history suggests that the 5x5 configuration may be particularly suited for applications where prior mechanical loading is relevant to sensor performance.

Overall, the data in Table 3.13 demonstrates the adaptability of the 5x5 strain gauge sensor to strain history and the increased variability under repeated or high strain. This configuration appears more sensitive to cumulative loading effects than the 4x5 configuration, which could make it advantageous for applications that require responsiveness to strain history but also suggest a potential trade-off in terms of consistency over time. Further studies, such as larger sample sizes and SEM imaging, could provide deeper insights into this sensor configuration's long-term durability and reliability under cyclic loading conditions.

Figure 3.21 displays the IV characteristics of strain gauge sensors configured in 4x5 layers (left column) and 5x5 layers (right column) under three conditions: at rest, 5% strain, and 10% strain.

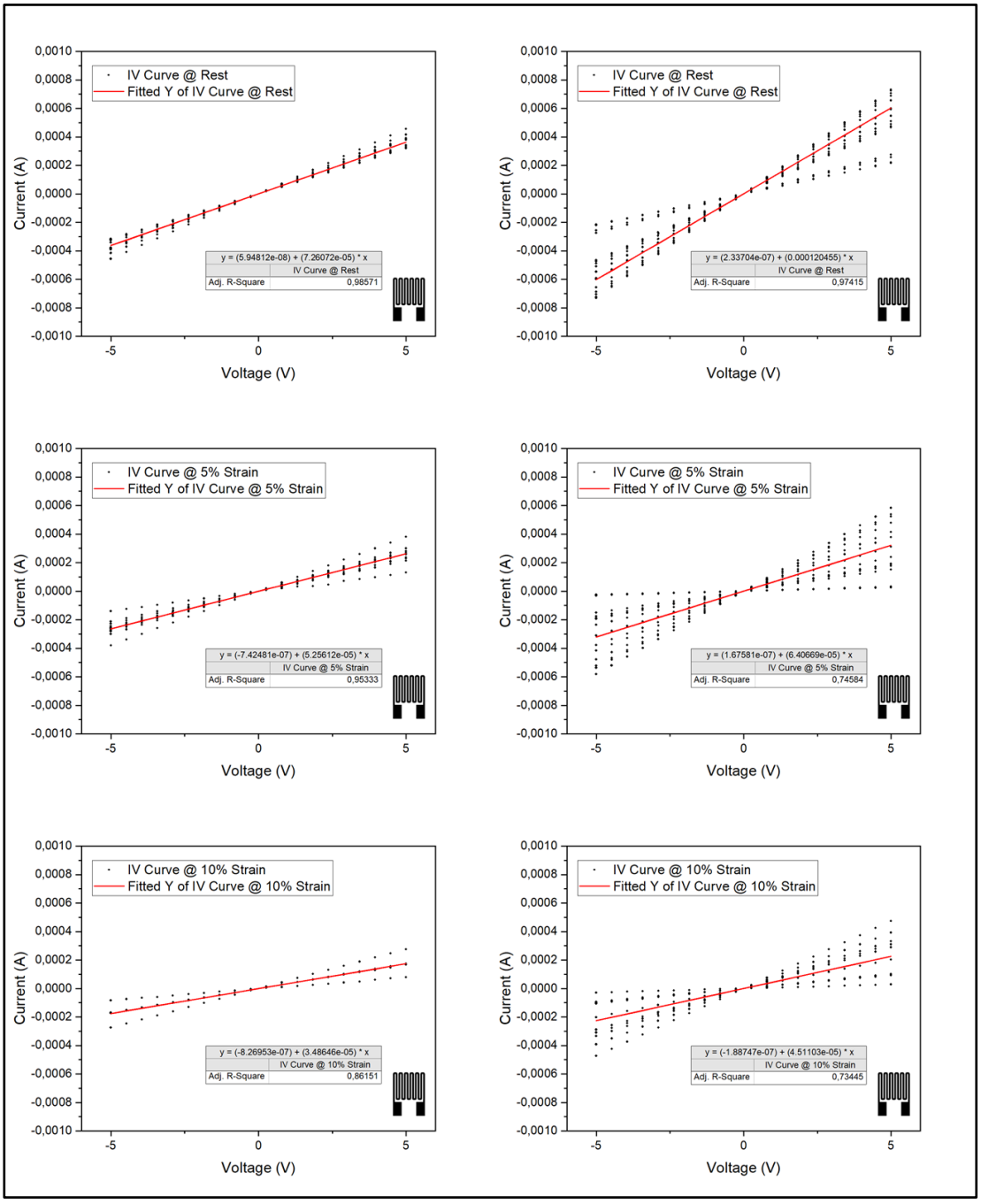

Figure 3.21 : IVs of strain gauge sensors 4x5 (left), 5x5 (right).

In the 4x5 configuration (left column), the IV curves at rest, 5% strain, and 10% strain all demonstrate a linear relationship between current and voltage, with each plot achieving a relatively high R-squared value, indicating good linearity. Specifically, the adjusted R-squared values are 0.99 at rest, 0.95 at 5% strain, and 0.86 at 10% strain.

These high R-squared values suggest that the 4x5 strain gauge configuration maintains a stable and predictable linear response across different strain levels. The slope of the IV curve, which represents resistance, increases with strain, indicating that resistance rises proportionally to strain.

For the 5x5 configuration (right column), the IV curves also exhibit linearity, although the R-squared values are lower than those in the 4x5 configuration. The adjusted R-squared values are 0.97 at rest, 0.75 at 5% strain, and 0.74 at 10% strain, showing a slight decrease in linearity as strain increases. The slope of the IV curves is also larger under strain conditions, suggesting an increase in resistance with strain, consistent with the behavior observed in the 4x5 configuration. However, the lower R-squared values under strain suggest that the 5x5 configuration may be more susceptible to variability or nonlinearity at higher strain levels.

In summary, the data presented in Table 3.12 and Table 3.13 illustrate that resistance levels in both 4x5-layered and 5x5-layered strain gauge sensors increase with applied strain and are further influenced by the history of previous strain. For the 4x5-layer configuration, initial resistance measurements exhibit moderate variability; however, both resistance and variability significantly increase as strain accumulates, particularly after exposure to high-strain conditions. This pattern indicates that prior strain exerts a lasting effect on resistance stability, likely attributable to microstructural changes within the sensor material, such as the formation of microcracks or the reconfiguration of conductive pathways.

Similarly, the 5x5-layer strain gauge sensors display an upward trend in both resistance and variability with increasing strain and cumulative strain history. Baseline measurements show moderate stability, but resistance levels and variability become more pronounced after repeated or high-strain exposures. This suggests that strain history plays a crucial role in shaping the sensor's structural and electrical characteristics, potentially due to cumulative microstructural adaptations that affect electron transport across the layers.

Both configurations exhibit a proportional increase in resistance with strain, aligning with typical strain gauge behavior. The 4x5 configuration demonstrates a more stable linear response across strain levels, as evidenced by high R-squared values. Conversely, the 5x5 configuration shows greater variability, particularly at 5% and

10% strain, suggesting that additional layers may introduce complexities that affect sensor stability under load. This variability implies that, while the 5x5 configuration may offer enhanced sensitivity, the 4x5 configuration could provide a more reliable linear response under varied strain conditions, making it potentially better suited for applications requiring consistent stability and predictability.

These findings emphasize the importance of considering strain history in applications requiring stable and predictable resistance measurements, especially under conditions of repeated or high strain. The observed sensitivity to cumulative strain indicates that structural changes within the sensor may impact long-term performance, underscoring the need to assess the durability and reliability of such sensors in applications involving cyclic or high-strain demands, such as wearable devices for continuous monitoring.

Table 3.14 presents resistance levels for strain gauge sensors with 4x5 layer and 5x5 layer configurations under different strain levels (0%, 5%, and 10%). The data highlights key observations related to the influence of both strain and layer configuration on resistance and variability.

Table 3.14 : Overall resistance levels per IV curves.

Sensor	Max Layer	Strain Level	Avg. Resistance (kΩ)	St. Deviation (kΩ)	#
Strain Gauge 	4	0%	12.77	3.14	15
		5%	18.08	8.08	15
		10%	26.14	15.43	12
	5	0%	9.49	3.79	17
		5%	15.17	8.74	15
		10%	22.07	17.24	14

For the 4x5 layer configuration, resistance values increase substantially with strain, from an average of 12.77 kΩ at 0% strain to 26.14 kΩ at 10% strain. This trend indicates a strong correlation between applied strain and resistance increase, likely due to structural changes in the sensor material under strain, such as microcracking or shifts in conductive pathways. Notably, the standard deviation also rises with strain, reaching 15.43 kΩ at 10% strain. This increase in variability suggests that higher strain introduces greater inconsistency in resistance values, which may be linked to uneven strain distribution or cumulative microstructural effects within the sensor.

The 5x5 layer configuration shows resistance increasing from 9.49 kΩ at 0% strain to 22.07 kΩ at 10% strain, with lower absolute values than the 4x5 sensor but a significant overall rise. Standard deviation also increases, reaching 17.24 kΩ at 10% strain, suggesting additional layers may amplify structural complexity and variability under strain.

The 4x5 layer sensor shows slightly higher resistance across all strain levels, likely due to differences in layer thickness or interlayer connectivity. Both configurations exhibit increased resistance and variability with strain, highlighting the impact of mechanical deformation on electrical properties. High standard deviation at 10% strain suggests structural factors like layer integrity and alignment are critical for consistent performance. These findings emphasize the need to optimize layer configuration and strain levels in applications requiring precise and stable resistance measurements, particularly in wearable strain sensors.

3.4.3.3 Cyclic test analysis

Table 3.15 provides data on GFs for strain gauge sensors with 4x5 and 5x5 layer configurations under different strain alterations. The table highlights how strain history and layer configuration influence the sensor's sensitivity to strain, as represented by the mean GF and its standard deviation.

Table 3.15 : GFs per different strain alterations measurements.

Sensor	Max Layer	Averaging	Strain Alteration	Mean GF	Std GF	#
Strain gauge 	4	5%	Bare	3.91	1.27	3
		10%	Bare	5.46	2.73	2
		5%	Post 10% Test	6.22	0.68	2
		10%	Post 5% Test	4.96	3.49	2
	5	5%	Bare	2.32	0.62	3
		10%	Bare	11.51	10.16	4
		5%	Post 10% Test	22.45	18.00	3
		10%	Post 5% Test	11.58	3.77	2

For the 4x5-layered configuration, the GF under bare conditions at 5% and 10% strain is relatively low, with mean values of 3.91 and 5.46, respectively, suggesting stable but moderate sensitivity to strain. When exposed to a prior 10% strain (Post 10% Test),

the GF at 5% strain increases to 6.22, indicating a slight enhancement in sensitivity, likely due to structural conditioning effects from the higher pre-strain. However, a decrease in GF is observed in the Post 5% Test condition at 10% strain, with a mean GF of 4.96, suggesting that prior lower strain exposure could potentially reduce the sensor's responsiveness to higher strain.

For the 5x5-layered configuration, bare conditions reveal a different trend. At 5% strain, the mean GF is 2.32, which is notably lower than the 4x5 configuration, while at 10% strain, it increases significantly to 11.51, with a high standard deviation of 10.16. This variability suggests that the 5x5 configuration may offer greater sensitivity under higher strain but at the cost of increased measurement variability. When subjected to pre-strain conditions, the GF values show substantial changes. Following a 10% strain (Post 10% Test), the mean GF at 5% strain increases markedly to 22.45, indicating a high sensitivity boost due to prior high-strain exposure. However, the GF drops to 11.58 at 10% strain in the post-5 % test condition, suggesting a reduction in sensitivity at higher strain levels after initial low-strain exposure.

In Figure 3.22, the cyclic behavior of a 4x5-layered strain gauge sensor subjected to 5% strain is illustrated. The top-left plot shows the resistance response over time for 100 cycles at a constant 5% strain, with both raw and smoothed resistance values. The resistance fluctuates within a range of approximately 13,000 Ω to 19,000 Ω, exhibiting relatively consistent oscillations throughout the duration of the test. This consistency suggests that the sensor maintains stable performance under repeated cyclic loading.

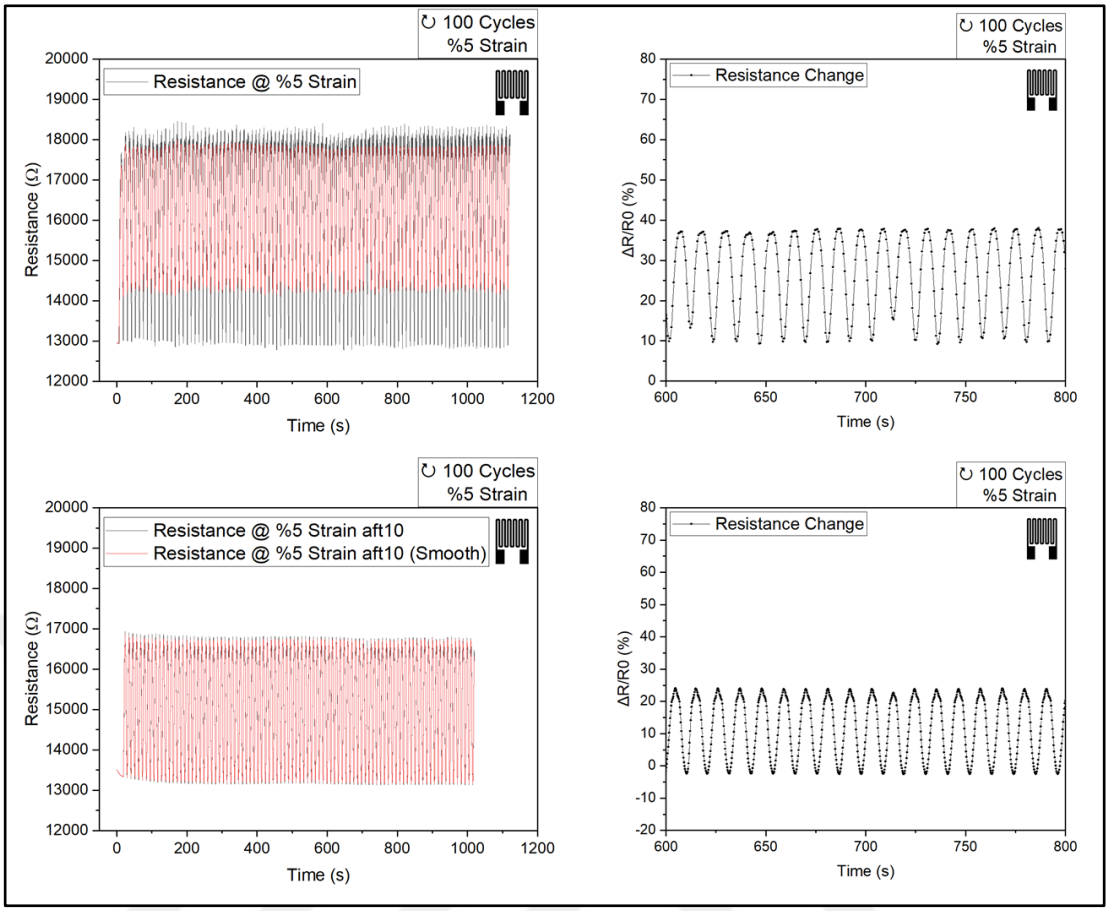

Figure 3.22 : Cyclic behaviors of 4x5 strain gauge sensors of 5% strain.

The top-right plot represents the percentage change in resistance ΔR/R during the same period, showing cyclic variations that peak around 40%. These variations indicate a predictable resistance response under 5% strain, with minor fluctuations in each cycle. The consistent peaks and troughs suggest that the strain gauge's sensitivity and response remain stable across cycles.

In the lower row, following an initial 10% strain test, the sensor is again subjected to 5% strain. The bottom-left plot presents the resistance data, with raw and smoothed lines indicating that the sensor's resistance range has narrowed slightly compared to the initial 5% strain test, suggesting potential structural adjustments in the material following higher strain exposure. The resistance now oscillates around a lower average range, indicating enhanced stability.

The bottom-right plot shows the percentage resistance change after the 10% strain pre-test. The observed ΔR/R continues to peak around 25%, displaying similar consistency in oscillations as before. This implies that the sensor, despite experiencing higher

initial strain, maintains its cyclic response predictability at 5% strain, underscoring the strain gauge's durability and potential resilience against cumulative strain effects.

Figure 3.23 presents the cyclic behavior of a 4x5-layered strain gauge sensor under 10% strain, observed over 100 cycles. The top-left graph shows the resistance response over time, with raw and smoothed data plotted together. The resistance fluctuates between approximately 15,000 Ω and 30,000 Ω, exhibiting regular oscillations throughout the test duration. This fluctuation range and consistent cyclic pattern suggest that the sensor maintains predictable performance under 10% strain.

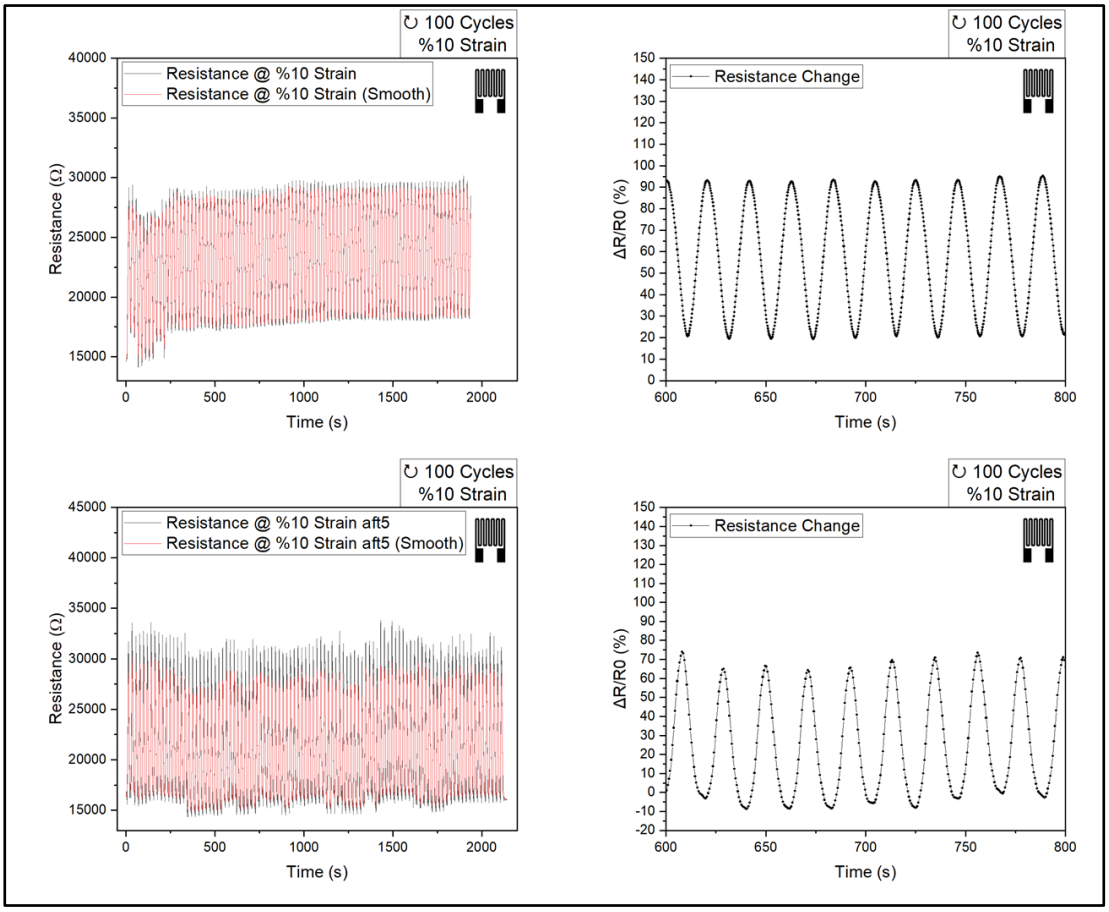

Figure 3.23 : Cyclic behavior of 4x5 strain gauge sensors of 10% strain.

The top-right graph illustrates the percentage change in resistance ΔR/R over time, with cyclic variations reaching approximately 95%. This periodic response indicates a stable resistance change pattern under the applied strain, showing that the sensor responds predictably across cycles, even under higher strain conditions.

Following an initial 5% strain test, the sensor is again subjected to 10% strain, and the resistance data is displayed in the bottom-left graph. Both raw and smoothed data reveal that the sensor continues to exhibit oscillatory behavior, though the resistance

range appears to increase slightly, suggesting potential adjustments in the sensor material due to previous strain exposure. Resistance oscillations are centered around a similar range, showing resilience in response to repeated higher strain.

The bottom-right graph shows the percentage resistance change following the 5% strain test and subsequent 10% strain application. The ΔR/R values again exhibit a periodic pattern peaking around 75%, maintaining similar oscillatory behavior. This consistent response implies that the strain gauge sensor retains its cyclic stability even after cumulative strain effects, demonstrating robustness and potential reliability in applications requiring repeated high-strain cycles.

In Figure 3.24, the cyclic behavior of a 5x5-layered strain gauge sensor under 5% strain across 100 cycles is shown. In the top-left graph, resistance is plotted against time, with both raw and smoothed data. The resistance fluctuates between approximately 8,500 Ω and 10,000 Ω, demonstrating consistent cyclic behavior. This pattern of resistance variation suggests stable performance of the sensor under repeated strain cycles.

The top-right graph presents the percentage resistance change ΔR/R over time. The resistance changes cycles steadily, peaking around 15%. This consistent cyclic response indicates that the sensor maintains a reliable performance under 5% strain without significant deviation.

In the bottom-left graph, resistance is measured after the sensor underwent an initial 10% strain test before returning to 5% strain for cyclic testing. The raw and smoothed data show a higher range of resistance, oscillating between 16,000 Ω and 32,000 Ω. This increase in resistance range may reflect permanent material changes due to the prior 10% strain, but the cyclic behavior remains stable, indicating robust performance even after higher strain exposure.

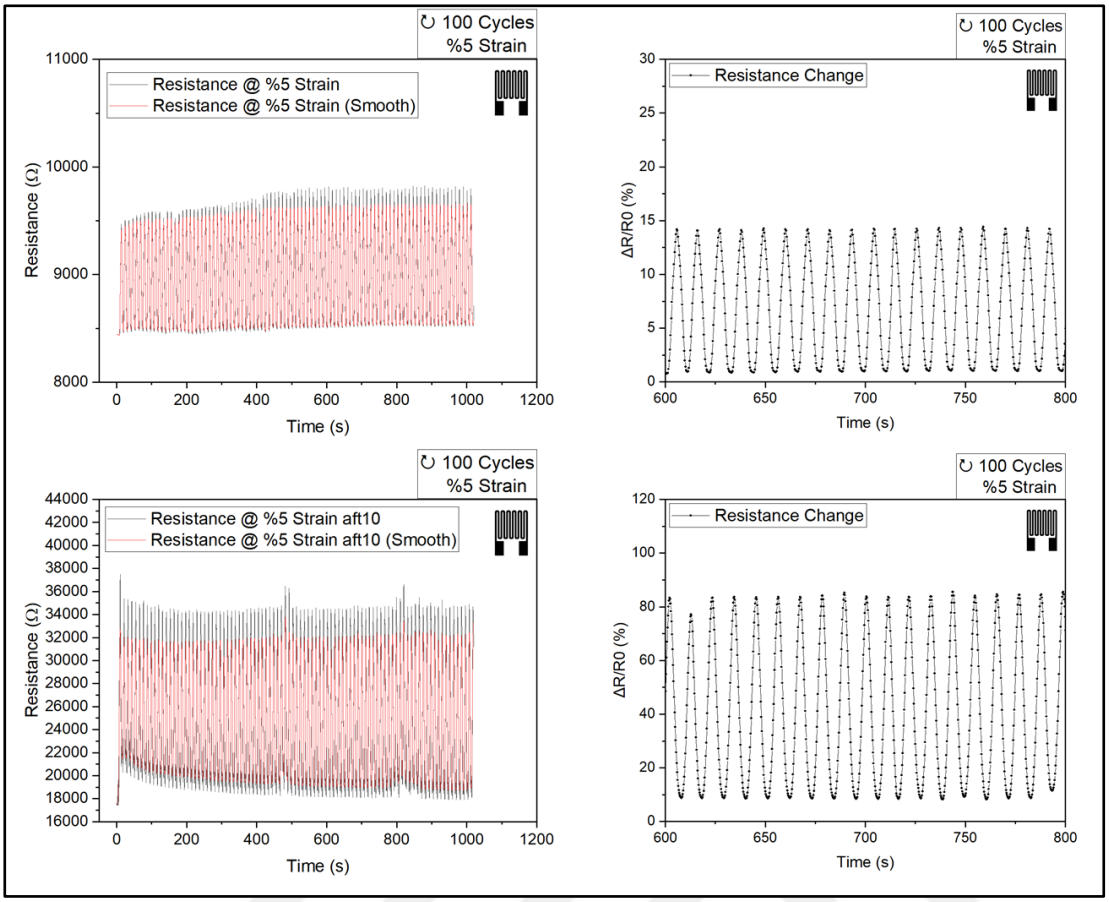

Figure 3.24 : Cyclic behaviors of strain gauge sensors of 5% strain level, for 5x5 layers.

The bottom-right graph shows the percentage resistance change following the 10% pre-strain. Here, ΔR/R displays consistent oscillations reaching approximately 85%. The sensor demonstrates stable cyclic performance despite the prior exposure to a higher strain level, suggesting resilience in accommodating repeated strain applications without significant degradation in cyclic stability.

In Figure 3.25, the cyclic behavior of a 5x5-layered strain gauge sensor under 10% strain across 100 cycles is displayed. In the top-left graph, resistance over time is shown with raw and smoothed data. The resistance oscillates between approximately 8,000 Ω and 12,000 Ω, with consistent cyclic fluctuations. This range and regularity of oscillation suggest the sensor maintains predictable performance even under repeated 10% strain.

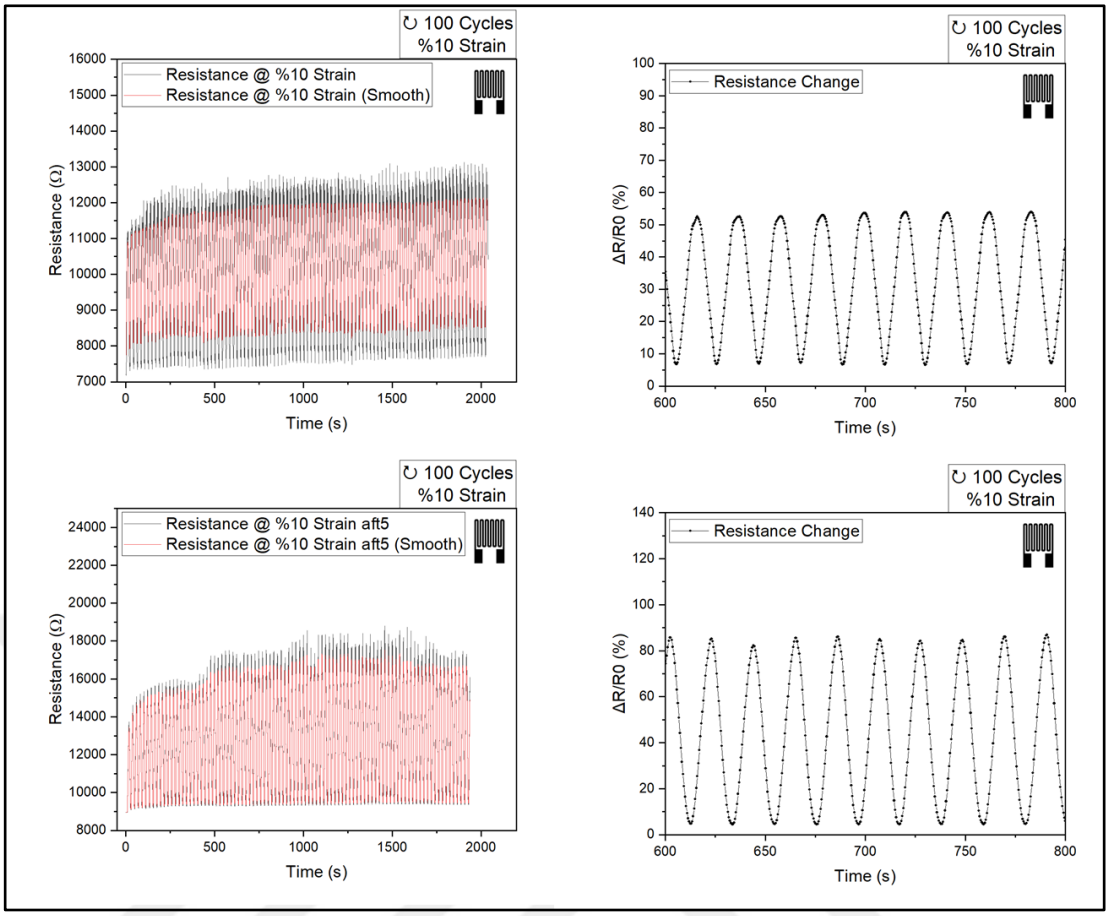

Figure 3.25 : Cyclic behavior of 5x5 strain gauge sensors of 10% strain level.

The top-right graph shows the percentage change in resistance ΔR/R over time, with periodic variations peaking around 55%. This steady cyclic response indicates stable sensor performance under the strain, demonstrating the sensor's resilience across cycles.

In the bottom-left graph, resistance measurements are shown after the sensor was initially subjected to a 5% strain test, followed by 10% strain application. Both raw and smoothed data indicate that the sensor continues to exhibit cyclic behavior, though with a broader resistance range compared to the top-left graph. This could suggest some adaptation in the sensor material due to previous strain, with oscillations remaining stable around a higher mean resistance level.

The bottom-right graph shows the percentage resistance change following the 5% and 10% strain tests. Here ΔR/R also exhibits consistent oscillations, reaching approximately 85%. This response implies that the strain gauge sensor maintains cyclic stability and robustness, demonstrating reliable performance under cumulative strain conditions and potentially high endurance for repeated strain applications.

Table 3.16 presents the GFs for strain gauge sensors with 4x5 and 5x5 layer configurations under different strain levels (5% and 10%). For the 4x5 layered strain gauge sensors, the mean GF at 5% strain 4.53 with a standard deviation of 1.82 across four samples, while at 10% strain, the mean GF increases slightly to 5.21 with a standard deviation of 2.23, also based on four samples. In contrast, the 5x5 layered sensors exhibit a significantly higher mean GF at 5% strain, recorded at 12.35 with a standard deviation of 16.23 across six samples, indicating considerable variability. At 10% strain, the mean GF for the 5x5 sensors is 11.55 with a standard deviation of 8.57, still displaying a relatively high variation but lower than at 5% strain. This data highlights the impact of layer configuration and strain level on the GF values, with the 5x5 layered sensors showing higher mean GFs and variability compared to the 4x5 layered sensors under the same conditions.

Table 3.16 : GFs per different strain levels between 4x5 and 5x5 layers.

Sensor	Max Layer	Strain Level	Mean GF	Std GF	#
Strain gauge 	4	5%	4.53	1.82	5
		10%	5.21	2.23	4
	5	5%	12.35	16.23	6
		10%	11.53	8.57	6

In the study performed by Shi et al. [111] it was observed that between 0% to 10% strain levels, graphene nanoplatelets (GnPs) with greater thickness exhibited lower sensitivity and smaller standard deviations. This was attributed to the higher stacking of graphene nanoplatelets, which enhances conductivity and thus reduces sensitivity. While there is similarity in non-pre-strained measurements at low strain levels (around 5%), the general results are contrary to the findings in this study. Compared to the IV results, increasing the thickness—and therefore the amount of graphene nanoplatelets—has a decreasing effect in resistance similarly. However, the GFs in this study increased significantly compared to those reported by Shi et al. In terms of material composition and geometry, the strain gauge in the mentioned study has two arms, whereas strain gauge here has ten arms. Additionally, GnPs are embedded in polydimethylsiloxane (PDMS) in mentioned study, here, they are embedded into textile. These two major differences might be the leading causes for the discrepancies in GFs, as the stress contribution and crack mechanisms might differ.

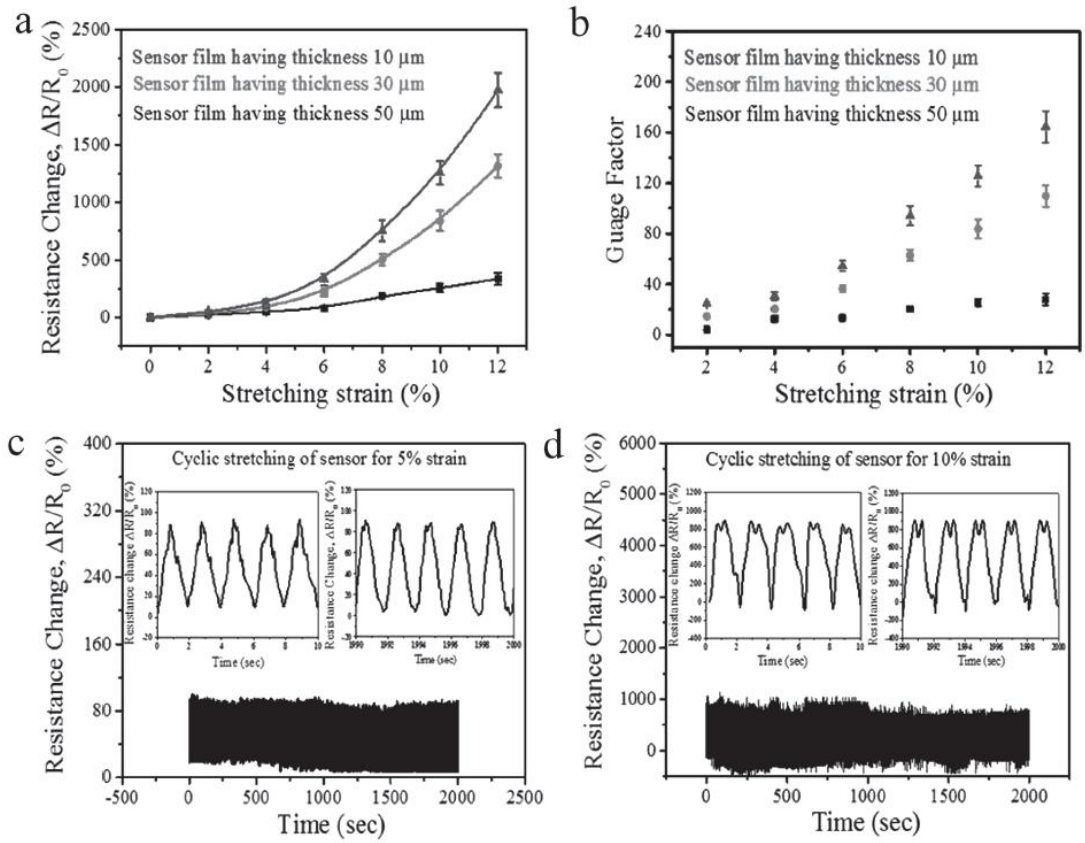

Figure 3.26 : Characterization of flexible GnP strain sensors (adapted from [111]).

3.4.4 Omnidirectional

This section analyzes the sensing performance of omnidirectional sensors with a central circle, two electrode lines, and five arms at 30-degree intervals. Challenges arise as the arms may deviate from the force direction, affecting measurement accuracy.

The omnidirectional design enhances measurement stability by providing multiple arms that mitigate electron blockage from cracks. Ideally, electrons follow the shortest central path, aligning with the principle of least action, minimizing the impact of additional arms.

Furthermore, considering the intended application of the sensor for monitoring respiration, any textile worn on the body will be subjected to forces in multiple directions. Therefore, the omnidirectional sensor geometry is advantageous for capturing such multidirectional strain, offering benefits in terms of both durability and sensitivity.

3.4.4.1 The effect of printing quality on the sensor performance

Figure 3.27 displays the printing quality and layer progression of a graphene-based omnidirectional sensor (L1–L5), with the left column showing the contact area and the right highlighting the sensing area for multidirectional strain detection.

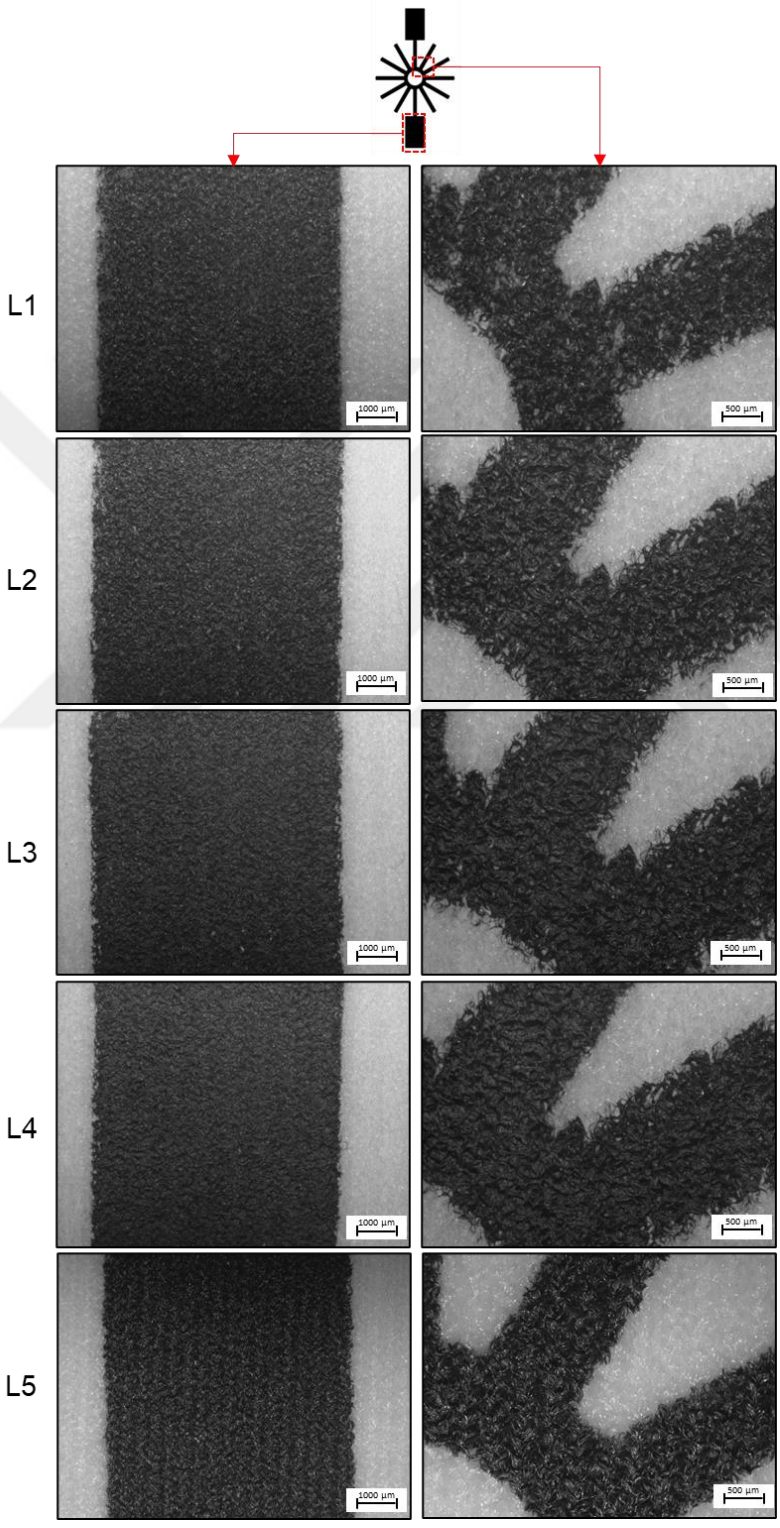

Figure 3.27 : Figures from omnidirectional sensor. From layer 1 to layer 5 (randomly taken).

From the left column, the contact area images demonstrate a relatively consistent deposition of graphene ink over the textile substrate. Across layers, the ink coverage appears dense and uniform, with minimal observable gaps or inconsistencies, which is essential for establishing a stable conductive pathway in the contact region. Maintaining uniformity in this area is crucial, as it ensures reliable electrical connectivity and minimizes variations in sensor output due to inconsistencies in ink distribution. The edges are well-defined, indicating effective control over the ink spreading within the intended boundaries in this simpler, more linear region.

In the right column, however, the sensing area images reveal challenges associated with the complex omnidirectional pattern. As additional layers are applied, there is a visible increase in texture and roughness, particularly at the edges and intersections of the branches. This roughening effect likely arises from cumulative material buildup in these intricate regions and from the inherent properties of the textile substrate, which can absorb and spread the ink unevenly at micro-intersections. The tendency for increased roughness with each successive layer may slightly impair the sensor's sensitivity by introducing localized resistance variations, although it may not significantly compromise overall performance given the design's focus on capturing strain from multiple directions.

Additionally, minor deviations from the intended pattern boundaries are noticeable at some branch intersections, potentially due to slight misalignments or the capillary effects of the textile fibers. These deviations could affect the precision of the sensor in applications where exact replication of the pattern geometry is critical. However, the observed minor deviations are unlikely to substantially impact the sensor’s omnidirectional functionality, given that the primary objective is multidirectional strain detection rather than unidirectional sensitivity.

In conclusion, the omnidirectional sensor displays consistent ink deposition in the contact area and reasonably well-controlled pattern boundaries in the sensing area, despite the inherent complexities of the design. The minor roughness and slight deviations observed in the sensing area with increased layering are manageable within the context of its intended application. Future improvements in the printing process might focus on refining alignment accuracy and reducing texture at intersection points to enhance the sensor’s consistency and sensitivity across cycles.

3.4.4.2 Analysis of IV curves

The data presented in Table 3.17 illustrates a discernible trend of increasing resistance with higher strain levels in 4x5 layered omnidirectional sensors. This pattern aligns with the anticipated behavior of strain sensors, where an increase in strain generally results in elevated resistance due to elongation and structural changes in the conductive pathways, reducing electron mobility and consequently increasing resistance.

In the baseline state, resistance rises linearly from 2.25 kΩ at 0% strain to 5.35 kΩ at 10% strain, offering predictable strain measurement. This unaltered response provides a valuable reference for the sensor's intrinsic behavior without prior loading effects.

Resistance deviates from the baseline after 5% and 10% strain tests, reaching 10.96 kΩ at 10% strain with a high standard deviation (8.12 kΩ). This variability indicates significant microstructural changes, such as crack formation or disruptions in conductive pathways, introducing randomness in resistance values.

Table 3.17 : Resistance levels per IV curves (4x5).

Max Layer	Strain Level	Strain Alteration	Avg. Resistance (kΩ)	St. Deviation (kΩ)	#
4	0%	Bare	2.25	1.17	5
	5%	Bare	3.25	1.32	4
	10%	Bare	5.35	2.12	3
	0%	Post 5%	1.44	-	1
	5%	Post 5%	2.96	-	1
	10%	Post 5%	10.96	8.12	2
	0%	Post 10%	1.84	0.03	2
	5%	Post 10%	3.63	0.04	2
	10%	Post 10%	5.02	0.06	2
	0%	Post 5% (Post 10%)	3.54	2.50	2
	5%	Post 5% (Post 10%)	5.95	2.94	2
	10%	Post 5% (Post 10%)	7.71	3.75	2
	0%	Post 10% (Post 5%)	1.93	-	1
	5%	Post 10% (Post 5%)	4.18	-	1
	10%	Post 10% (Post 5%)	10.67	-	1

Post-10% strain testing, the measurements exhibit greater stability, with lower standard deviations across all strain levels. For example, at 10% strain, the resistance is measured at 5.02 kΩ with a minimal deviation of 0.06 kΩ, indicating that the sensor structure may have adapted to the applied strain, reaching a new equilibrium state. This stabilization implies that, although the initial application of higher strain may have caused some irreversible microstructural changes, subsequent measurements reflect a more consistent structural configuration.

The results following combined strain tests (5% and 10%) reveal a further increase in resistance and variability, especially at higher strain levels. For instance, the resistance at 10% strain after combined tests reaches 7.71 kΩ, accompanied by a standard deviation of 3.75 kΩ. This suggests that repeated loading and unloading cycles, particularly at higher strains, exacerbate the formation and expansion of microstructural changes within the sensor. Such changes may include the propagation and connection of microcracks, reorganization of conductive pathways, and potential fatigue effects, all contributing to an increase in resistance and variability.

Lastly, the results from sequential 10% and 5% strain tests suggest residual strain effects. Specifically, the resistance reaches its highest value of 10.67 kΩ at 10% strain after sequential testing, with negligible variability across measurements. This finding implies that, after sufficient cycling at elevated strain levels, the sensor structure may reach a threshold of irreversible deformation, beyond which further loading cycles do not significantly impact resistance.

These findings highlight the sensor's sensitivity to both strain magnitude and strain history. The observed irreversible structural changes following cyclic loading indicate that omnidirectional sensors may experience cumulative fatigue under repeated strain applications, potentially impacting their long-term reliability and accuracy in strain measurements. These results underscore the importance of understanding sensor hysteresis and resistance drift due to accumulated microstructural changes under cyclic strain, factors which may necessitate recalibration to maintain consistent sensor performance over prolonged use.

The data presented in Table 3.18 demonstrates a clear trend in resistance levels for 5x5 layered omnidirectional sensors under varying strain conditions, both in bare and post-test states. Initially, in the bare state, the resistance shows an expected increase with

the strain level, from 2.17 kΩ at 0% strain to 6.22 kΩ at 10% strain, indicating a standard response where increased strain induces structural changes that hinder conductivity, leading to higher resistance. This progressive rise aligns with anticipated material behavior, where elongation under strain disrupts conductive pathways.

After subjecting the sensors to a 5% strain test, the resistance values show varied changes. At 0% strain following the test, the resistance slightly reduces to 1.20 kΩ, suggesting a structural adjustment or partial recovery post-strain. However, a notable gap in data at 5% strain limits the ability to determine a consistent trend for post-5% test values. The 10% strain level after the 5% test reaches 5.44 kΩ, suggesting that residual effects from previous strain cycles may lead to an increase, though limited data points hinder a robust interpretation.

Table 3.18 : Resistance levels per IV curves (5x5)

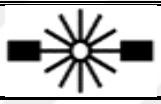

Max Layer	Strain Level	Strain Alteration	Avg. Resistance (kΩ)	St. Deviation (kΩ)	#
	0%	Bare	2.17	0.55	6
	5%	Bare	3.42	0.62	4
	10%	Bare	6.22	0.83	3
	0%	Post 5%	1.20	-	1
	5%	Post 5%	-	-	-
	10%	Post 5%	5.44	-	1
	0%	Post 10%	2.09	0.27	2
5	5%	Post 10%	7.62	1.22	2
	10%	Post 10%	11.60	5.65	2
	0%	Post 5% (Post 10%)	2.22	0.27	2
	5%	Post 5% (Post 10%)	7.56	0.88	2
	10%	Post 5% (Post 10%)	11.24	5.42	2
	0%	Post 10% (Post 5%)	-	-	-
	5%	Post 10% (Post 5%)	-	-	-
	10%	Post 10% (Post 5%)	-	-	-

In the condition after a 10% test, the resistance levels appear relatively stable with minimal deviation at lower strains. For instance, the resistance at 0% strain post-10%

test is 2.09 kΩ with a low standard deviation of 0.27 kΩ, implying consistent sensor performance. However, at higher strains, particularly at 10%, the resistance reaches 11.60 kΩ, showing a significant standard deviation (5.65 kΩ), which indicates potential variability due to microstructural fatigue or irreversible changes incurred during previous strain cycles.

The data after sequential strain applications (5% and 10%) further highlight the impact of strain history. After subjecting the sensor to both 5% and 10% tests, resistance at 10% strain reaches 11.24 kΩ, with high variability (standard deviation of 5.42 kΩ). This elevated resistance and deviation underscore the cumulative effect of strain, potentially resulting in microcrack propagation, delamination, or fatigue effects that introduce structural inconsistencies within the sensor matrix.

Overall, the results suggest that the omnidirectional sensor's resistance is highly influenced by its strain history, with higher strain levels introducing variability and indicating possible fatigue effects. This variability may necessitate calibration or adaptation in practical applications to account for changes in sensor performance over repeated strain cycles.

Figure 3.28 illustrates the IV characteristics of omnidirectional sensors under different strain levels for 4x5 and 5x5 layer configurations. Each subplot shows the IV curve at a specific strain level (0%, 5%, and 10%) with corresponding linear fits. For the 4x5 configuration on the left, the IV curve at rest (0% strain) demonstrates a high degree of linearity with an adjusted R-squared value of 0.88, indicating a consistent conductive pathway when unstrained. At 5% strain, the IV response remains linear with a slight decrease in slope, achieving an R-squared of 0.92, suggesting that minor strain does not significantly disrupt the current-voltage relationship. However, at 10% strain, the curve's linearity diminishes, with an R-squared of 0.87, reflecting the increasing impact of strain on resistance, potentially due to microstructural adjustments within the sensor.

For the 5x5 configuration on the right, the IV curve at 0% strain also exhibits linear behavior with a higher R-squared value of 0.95, indicating stable conductivity in the initial state. When subjected to 5% strain, the IV curve slightly loses its linearity with an R-squared of 0.84, showing that moderate strain impair linearity. At 10% strain, however, the linearity increases again, with an R-squared of 0.90.

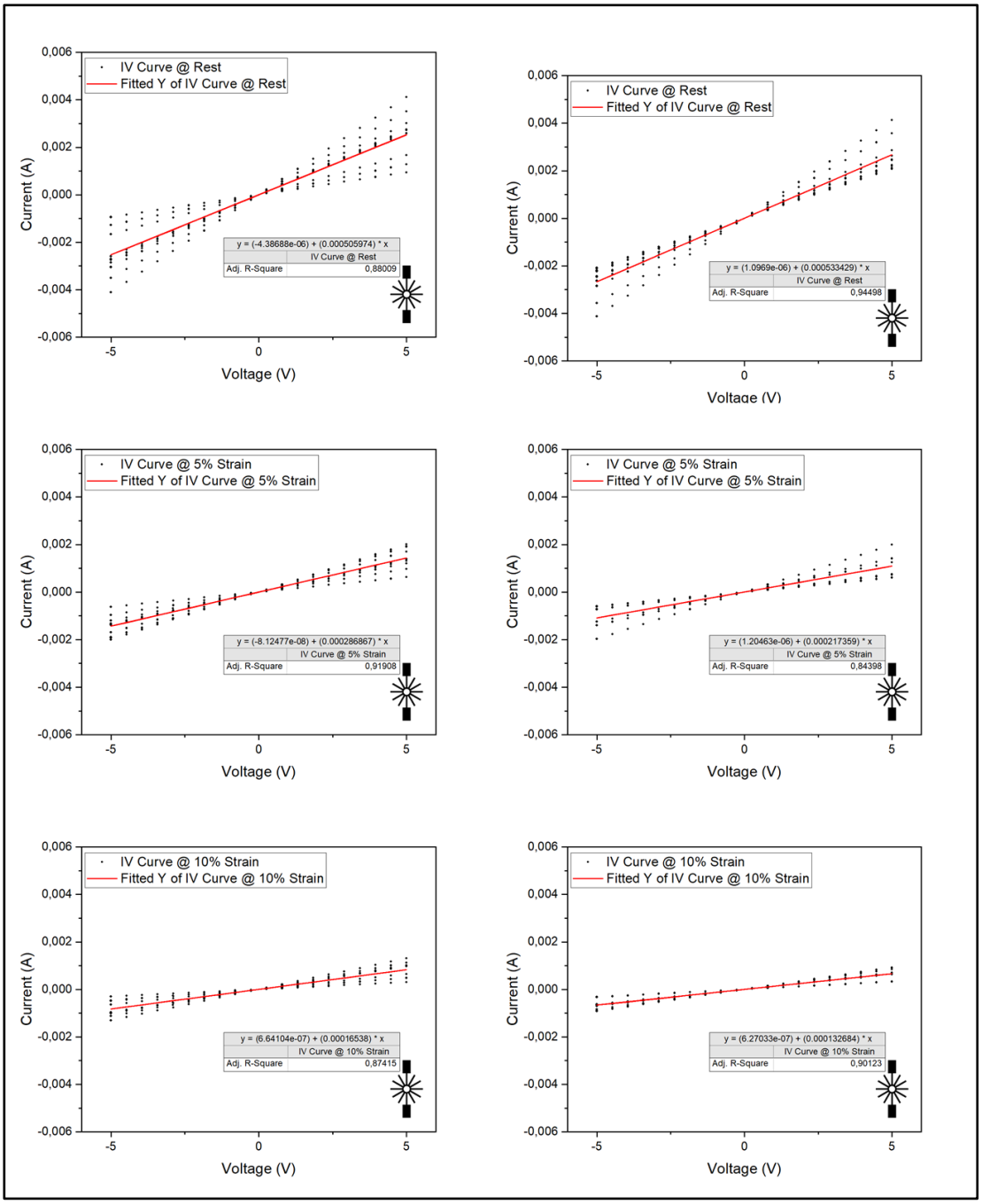

Figure 3.28 : IVs of omnidirectional sensors 4x5 (left), 5x5 (right).

The data suggest that both configurations maintain a degree of linearity. However, it remains inconclusive whether 4x5 or 5x5 layer configuration is superior to higher strain levels as 4x5 layered configuration is more linear at 5% compared to 5x5 layered configuration, but at 10 %, 5x5 layered configuration is better. An extra layer in an omnidirectional sensor appears to affect the conductivity slightly more due to stiffness.

Table 3.19 presents the resistance levels for omnidirectional sensors with 4x5 and 5x5 layering configurations under different strain conditions. The data reveal a systematic

increase in resistance as strain levels escalate, consistent with the expected behavior of conductive materials under mechanical stress. For the 4x5 layer configuration, resistance begins at 2.31 kΩ under 0% strain and rises progressively to 3.93 kΩ at 5% strain and 7.41 kΩ at 10% strain. This trend indicates that the strain disrupts conductive pathways, thereby elevating resistance. The standard deviation also increases with strain, from 1.27 kΩ at 0% strain to 4.07 kΩ at 10%, suggesting a growing variability in resistance as strain induces microstructural changes within the sensor.

Table 3.19 : Overall resistance levels per IV curves.

Sensor	Max Layer	Strain Level	Avg. Resistance (kΩ)	St. Deviation (kΩ)	#
Omnidirectional 	4	0%	2.31	1.27	11
		5%	3.93	1.67	10
		10%	7.41	4.07	10
	5	0%	2.08	0.50	11
		5%	5.50	2.33	8
		10%	8.72	4.16	8

For the 5-layer configuration, resistance values follow a similar pattern, beginning at 2.08 kΩ at 0% strain, increasing to 5.50 kΩ at 5% strain, and reaching 8.72 kΩ at 10% strain. The standard deviation also reflects this upward trend, starting at 0.50 kΩ at 0% strain and rising to 4.16 kΩ at 10% strain, indicating that higher strain levels introduce greater variability in resistance measurements. The 5x5 layer configuration shows a higher resistance at each strain level compared to the 4x5 layer configuration, which is likely due to the added layer creating additional pathways and interfaces that are susceptible to deformation under strain, thereby increasing overall resistance.

This data supports the understanding that both the number of layers and the level of strain significantly impact the resistance levels in these sensors. The increased variability at higher strain levels in both configurations suggests potential microstructural damage or reconfiguration, which could affect long-term sensor reliability. Thus, careful calibration and consideration of strain history are essential when employing these sensors in practical applications. The observed resistance behaviors underscore the cumulative effects of mechanical strain on the conductive pathways, with a pronounced impact on multi-layer configurations, which may require

additional stabilization or reinforcement for consistent performance under cyclic loading conditions.

3.4.4.3 Cyclic test analysis

Table 3.20 presents the GFs for omnidirectional sensors with different layer configurations (4x5 and 5x5) across various strain levels and testing conditions. For the 4x5 configuration, the mean GF at a 5% strain level under bare conditions is 33.66, with a standard deviation of 10.25, based on two samples. At a 10% strain level under bare conditions, the mean GF decreases to 12.38, with a standard deviation of 2.54 across three samples. After subjecting the sensor to a 10% strain pre-test, the 5% strain level shows a reduced mean GF of 10.67 with a standard deviation of 1.56, suggesting a moderate impact from pre-testing. The 10% strain level, after a 5% strain pre-test, records a higher mean GF of 23.93, with a considerable standard deviation of 11.14 across two samples, indicating variability likely due to microstructural changes.

Table 3.20 : GFs per different strain alteration measurements.

Sensor	Max Layer	Strain Level	Strain Alteration	Mean GF	Std GF	#
Omnidirectional 	4	5%	Bare	33.66	10.25	2
		10%	Bare	12.38	2.54	3
		5%	Post 10% Test	10.67	1.56	2
		10%	Post 5% Test	23.93	11.14	2
	5	5%	Bare	12.80	8.36	2
		10%	Bare	14.17	7.04	4
		5%	Post 10% Test	32.92	17.83	3
		10%	Post 5% Test	39.41	-	1

For the 5x5 configuration, the GF at a 5% strain level in bare conditions is 12.80, with a standard deviation of 8.36 across two samples. At 10% strain, the mean GF increases to 14.17, with a lower standard deviation of 7.04, reflecting increased strain sensitivity in this configuration. After a 10% strain pre-test, the 5% strain level exhibits a significantly increased mean GF of 32.92, with a standard deviation of 17.27 based on 3 samples, indicating a substantial impact from pre-testing on strain sensitivity. The 10% strain level following a 5% strain pre-test has a mean GF of 39.41, based on a single sample, suggesting a continued high sensitivity to strain in this condition.

The data underscore that pre-testing strain levels influence the GF values in both configurations, with the 5x5 layer configuration exhibiting a more pronounced response to prior strain application. This enhanced sensitivity in the 5x5 layer configuration may stem from the additional conductive pathways, which are more susceptible to strain-induced alterations. The variability in GF values, particularly after pre-testing, highlights the complex interplay between layer composition and strain history, impacting the sensor's performance. These findings indicate that the omnidirectional sensor's GF can be modulated by strain history, which may be relevant in applications where strain sensitivity and measurement stability are critical.

Figure 3.29 illustrates the cyclic behavior of omnidirectional sensors with 4x5 layers under 5% strain over 100 cycles. In the top left plot, the raw and smoothed resistance values over time show an increasing trend with periodic fluctuations, likely corresponding to strain cycles. This increase in resistance suggests the accumulation of microstructural changes due to repeated loading, while the smoothing curve reduces noise, emphasizing the general trend.

The top right plot represents the relative resistance change $\Delta R/R$ as a percentage. The graph shows a consistent cyclic pattern with a peak amplitude close to 125%, reflecting the sensitivity of the sensor to the applied cyclic strain. The regularity in peak values indicates repeatable performance across cycles.

In the lower-left plot, the sensor's resistance behavior is depicted after undergoing 10 cycles of initial conditioning strain, then further tested under 5% strain for 100 cycles. The resistance curve demonstrates an elevated baseline compared to the initial cycle plot, which may indicate permanent microstructural alterations or additional crack formation due to the initial 10% cycle strain conditioning. The smoothed data curve provides a clearer trend of this elevated resistance over time.

Finally, the lower right plot shows the relative resistance change $\Delta R/R$ after the initial conditioning cycles. The consistent cyclic response with an amplitude around 90% demonstrates a maintained but slightly reduced sensitivity relative to the initial, unconditioned state. This reduction in peak amplitude could be due to a stabilization of microstructural changes post-conditioning.

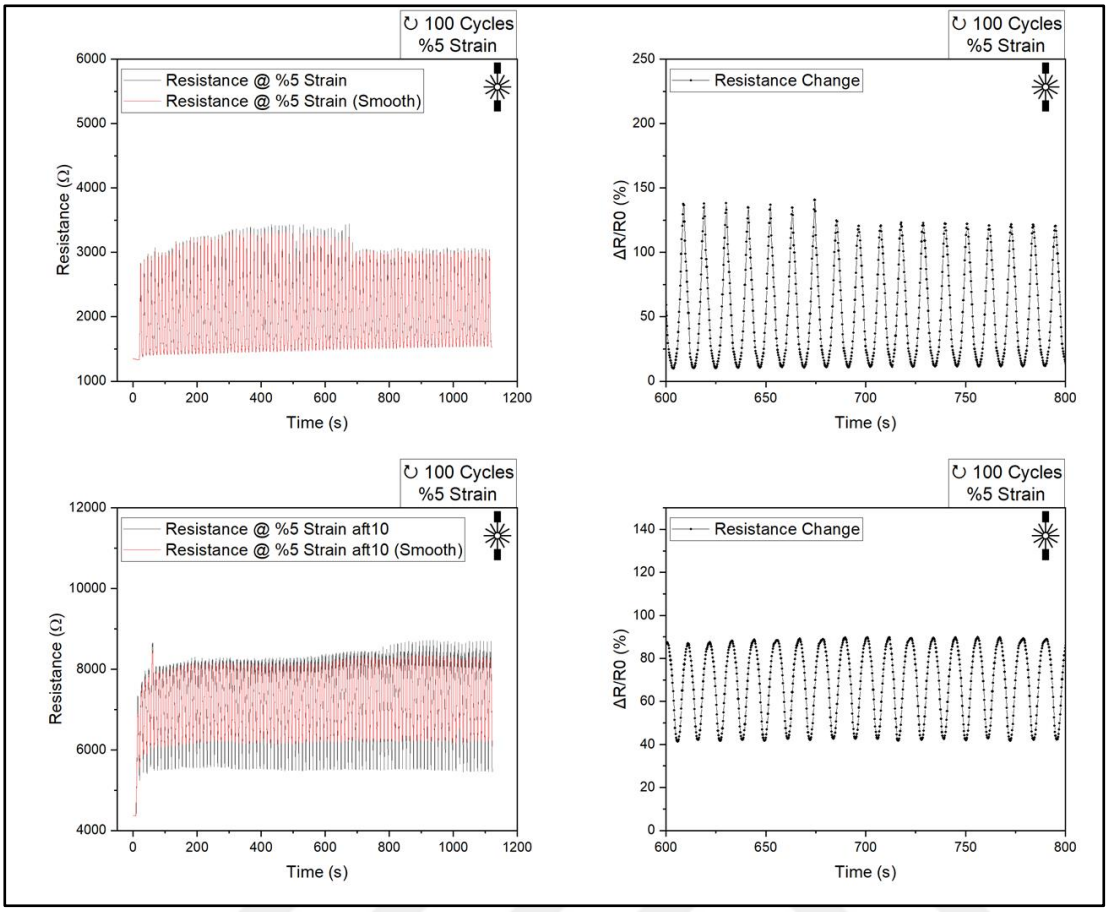

Figure 3.29 : Cyclic behaviors of 4x5 omnidirectional sensors of 5% strain level.

Overall, these observations highlight the resilience and repeatability of the omnidirectional 4x5 layer sensor under cyclic loading. The consistent resistance response across cycles and the impact of conditioning suggest that while initial conditioning may slightly reduce sensitivity, the sensor remains reliable and responsive to repeated strain. This behavior is valuable for applications requiring durability and stable performance under cyclic mechanical loading.

Figure 3.30 presents the cyclic behavior of omnidirectional sensors with 4x5 layers under 10% strain across 100 cycles. In the upper left plot, the raw and smoothed resistance data over time reveal a generally increasing trend with cyclic fluctuations. The resistance increases progressively, likely due to cumulative microstructural changes within the sensor under sustained cyclic loading, while the smoothed curve captures the overarching trend with reduced noise.

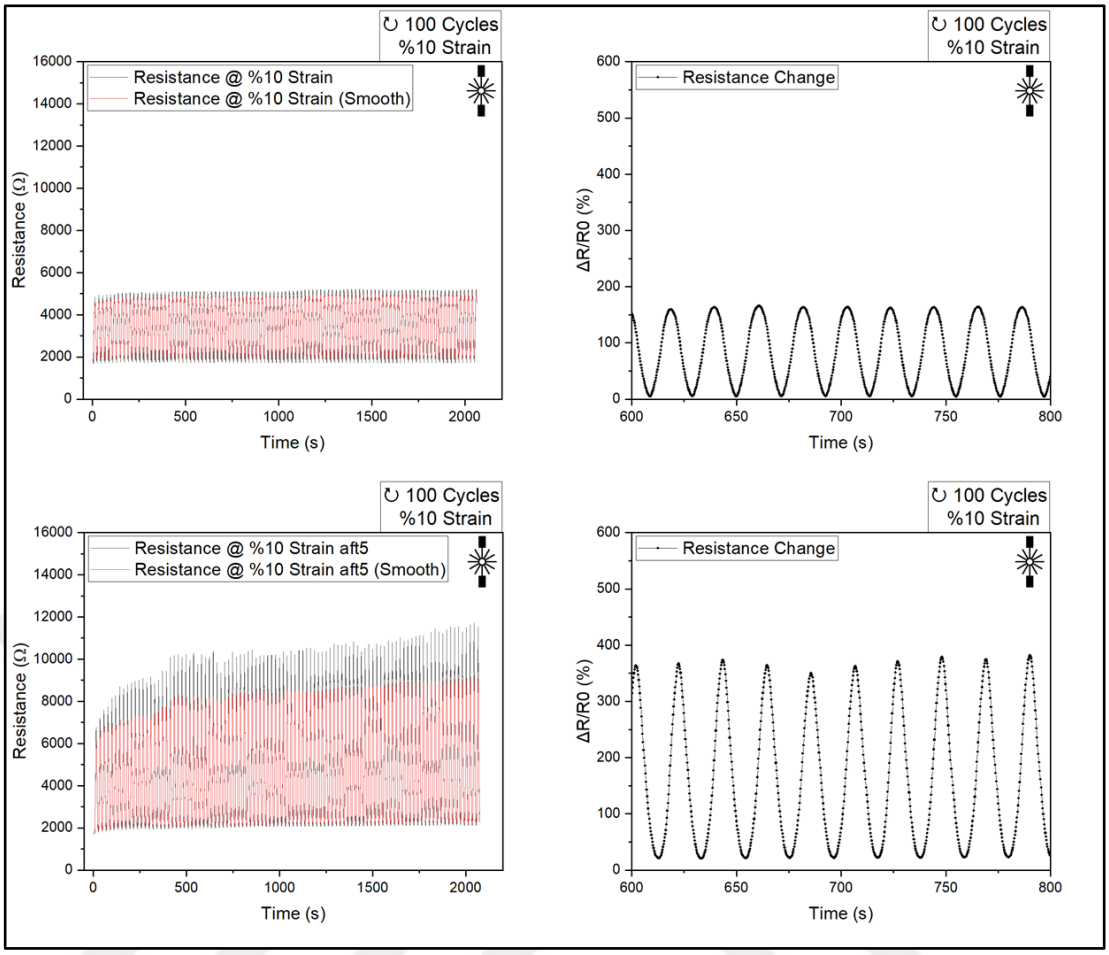

Figure 3.30 : Cyclic behaviors of 4x5 omnidirectional sensors of 10% strain level.

The upper-right plot shows the relative resistance change $\Delta R/R$ reaching 150%, indicating high sensitivity and stable, repeatable performance over 100 cycles. In the lower-left plot, resistance behavior after 5 cycles at 10% strain followed by 100 cycles reveals a higher baseline, suggesting structural changes from initial conditioning. The smoothed curve indicates a gradual resistance increase, reflecting ongoing adjustments under repeated loading.

The lower right plot provides the relative resistance change ΔR/R following the initial 5-cycle conditioning. The peak amplitude, now reaching approximately 400%, reflects a significantly enhanced sensitivity, potentially due to accumulated microcracks or other microstructural modifications caused by the preconditioning cycles. This heightened response implies that initial conditioning amplifies the sensor's sensitivity to subsequent cyclic strain.

Overall, the data in Figure 3.30 underline the robust cyclic response of the omnidirectional 4x5 layer sensor under high strain levels, with an observable impact

of preconditioning on sensitivity. The consistency in cyclic response and the increased resistance changes post-conditioning suggest that the sensor maintains reliability while exhibiting a heightened sensitivity to strain cycles, which could be advantageous in applications requiring both durability and high sensitivity under repeated mechanical stress.

Figure 3.31 illustrates the cyclic behavior of omnidirectional sensors with a 5x5 layer configuration under 5% strain over 100 cycles. In the top left plot, the resistance response, represented by both raw and smoothed data, shows a relatively stable trend with minor fluctuations. The smoothed curve reveals a consistent baseline with minimal drift, indicating stable performance and minimal cumulative damage or adaptation under the applied cyclic loading at this moderate strain level.

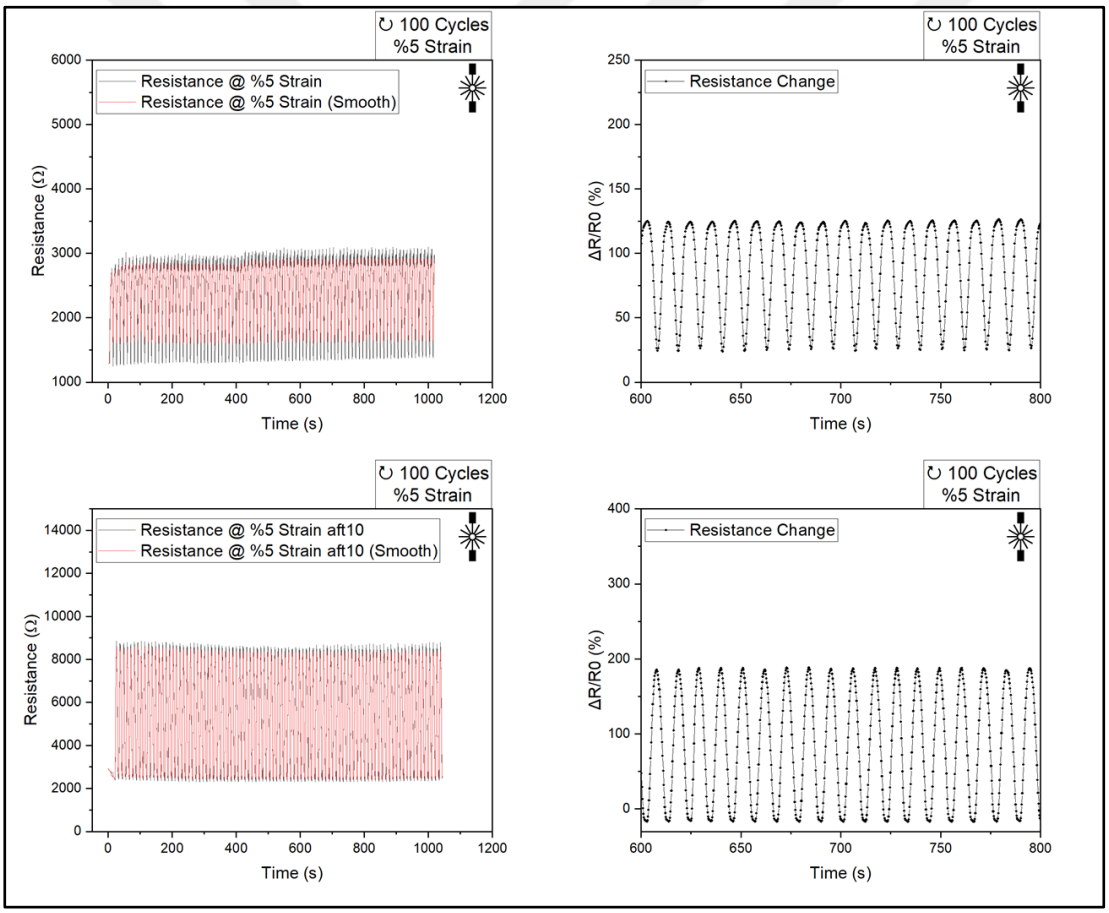

Figure 3.31 : Cyclic behaviors of omnidirectional sensors of 5% strain level, for 5x5 layers.

The top right plot displays the relative resistance change as a percentage, showing a regular cyclic pattern with peaks reaching approximately 125%. This pattern suggests

a steady and repeatable sensor response to cyclic strain, maintaining a reliable sensitivity without significant variation between cycles.

In the lower-left plot, the resistance data for the sensor following initial 10-cycle conditioning at 5% strain is depicted. After this preconditioning, the baseline resistance increases, likely due to slight structural changes in the material induced by the initial conditioning. The smoothed curve further highlights this baseline shift, but the overall response remains stable over the 100 cycles, indicating the sensor's durability even after initial conditioning.

The lower right plot presents the relative resistance change ΔR/R following the 10-cycle preconditioning. The peak amplitude has increased to around 200%, demonstrating an enhanced sensitivity as a result of the initial cycles. This heightened response implies that the sensor structure may have developed microcracks or other microstructural changes during conditioning, which increases sensitivity to subsequent cyclic loading.

Overall, the data in Figure 3.31 suggest that the omnidirectional 5x5 layer sensor exhibits stable cyclic behavior under moderate strain, with an observable increase in sensitivity following initial conditioning cycles. The results underline the sensor’s resilience and suggest that preconditioning can enhance sensitivity, potentially benefiting applications where consistent and heightened responsiveness to cyclic strain is required.

Figure 3.32 presents the cyclic behavior of omnidirectional sensors with a 5x5 layer configuration under 10% strain over 100 cycles. In the top left plot, the resistance values, both in raw and smoothed data, exhibit an increasing trend over time, indicating a potential progressive adaptation or microstructural changes in the sensor material under the higher strain level. The smoothed data line highlights this trend, revealing a gradual increase in baseline resistance throughout the cyclic loading.

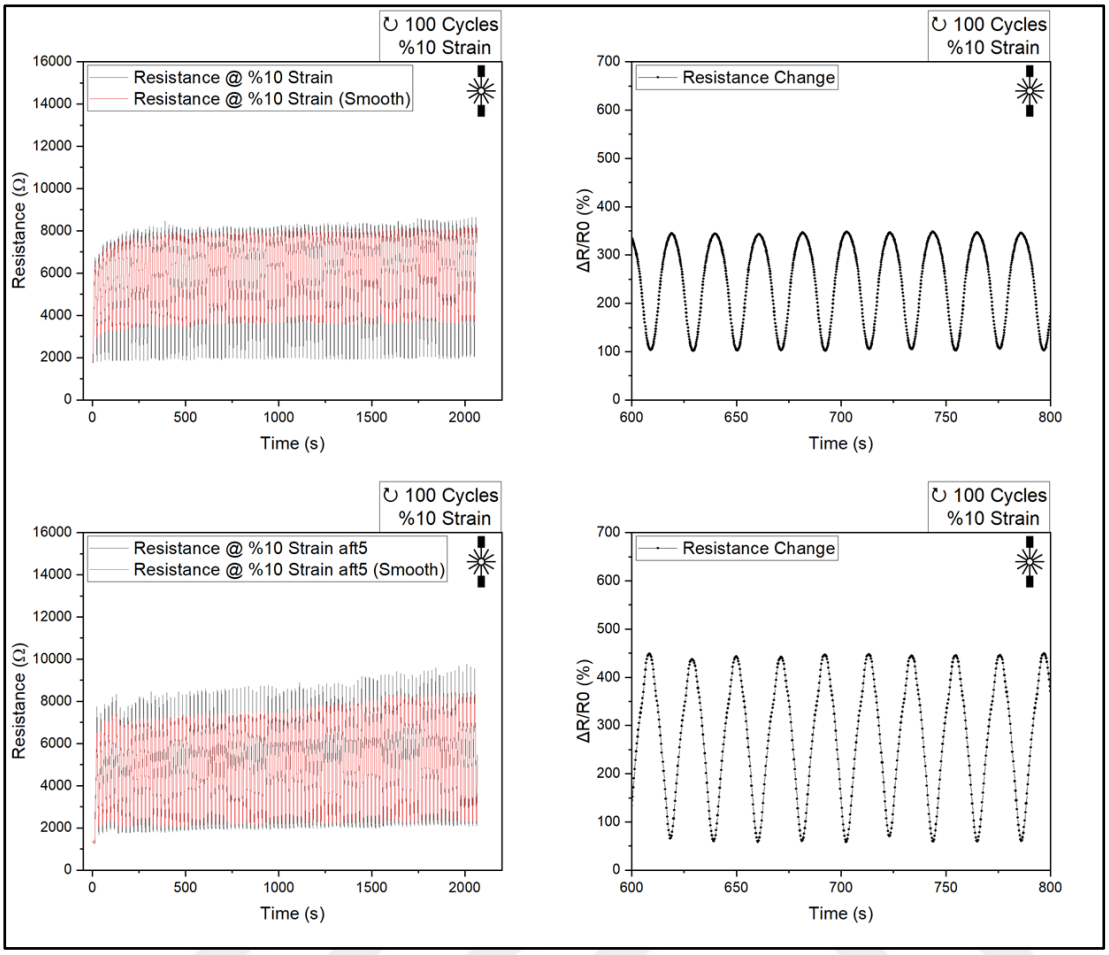

Figure 3.32 : Cyclic behaviors of 5x5 omnidirectional sensors of 10% strain level.

The top right plot illustrates the relative resistance change ΔR/R in percentage terms, showing a pronounced cyclic pattern with peak values reaching approximately 350%. This high level of resistance change suggests an elevated sensitivity of the sensor to the applied strain, with a consistent response across cycles, implying structural integrity despite the high strain level.

In the lower-left plot, the resistance behavior following initial 5-cycle conditioning at 10% strain is shown. Post-conditioning, the resistance values demonstrate an altered baseline with a slightly reduced amplitude, as indicated by the smoothed line. This suggests that the initial conditioning phase may have induced microstructural adjustments, stabilizing the sensor's response to subsequent cycles.

The lower right plot displays the relative resistance change after the initial conditioning. The cyclic response is consistent, with peaks reaching up to 400%, indicating enhanced sensitivity post-conditioning. This increased responsiveness

could be attributed to structural alterations from the initial cycles, enhancing the material's sensitivity to cyclic strain at high strain levels.

In summary, Figure 3.32 indicates that the omnidirectional 5x5 layer sensor demonstrates a robust cyclic response under a high strain level (10%), with a marked increase in sensitivity post-conditioning. The progressive increase in resistance during the cycles suggests structural adjustments within the sensor, contributing to its heightened sensitivity, which could be advantageous in applications requiring reliable detection of high strain levels.

Table 3.21 summarizes the GFs for omnidirectional sensors with both 4x5 and 5x5 layer configurations under different strain levels of 5% and 10%. For the 4x5 layer configuration, the mean GF at 5% strain is 22.16, with a standard deviation of 13.63, based on four measurements. When the strain level is increased to 10%, the mean GF decreases to 17.00, with a slightly lower standard deviation of 9.25 across five measurements. This reduction in mean GF at higher strain levels suggests a diminishing sensitivity with increased strain for the 4x5 layer configuration.

Table 3.21 : GFs per different strain levels between 4x5 and 5x5 Layers.

Sensor	Max Layer	Strain Level	Mean GF	Std GF	#
Omnidirectional 	4	5%	22.16	13.63	4
		10%	17.00	9.25	5
	5	5%	24.87	17.37	5
		10%	19.21	11.90	5

In the 5x5 layer configuration, the mean GF at 5% strain is slightly higher at 24.87 with a standard deviation of 17.37, indicating increased sensitivity compared to the 4x5 layer configuration at the same strain level. At 10% strain, the mean GF for the 5x5 layer configuration slightly decreases to 21.04, with a standard deviation of 13.70, measured across 5 instances. This trend mirrors the 4x5 layer configuration, with a reduction in GF as strain levels increase, though the 5x5 layer configuration maintains higher sensitivity overall at both strain levels compared to the 4x5 layer counterpart.

The results in Table 3.21 highlight that the 5x5 layer omnidirectional sensor consistently demonstrates higher GF values, indicative of enhanced sensitivity relative to the 4x5 layer configuration. The observed decrease in GF at higher strain levels for

both configurations suggests that increased strain may affect the material properties, possibly leading to a plateau or decline in sensitivity. This data provides insight into the influence of layer composition and strain intensity on the sensitivity of omnidirectional sensors, which is critical for optimizing sensor performance in applications requiring precise strain detection.

3.4.5 Destructive testing

To gain insights into the dispersion of ink within the textile, specimens were carefully dissected using scissors. Subsequently, optical microscopy was employed to capture images of the specimens positioned between two microscope slides. It is important to note that the measurements obtained during this preliminary phase were not standardized, as the specimens were manually manipulated and positioned closer to the microscope lens than is typically the case in controlled measurement environments. This non-standard handling and positioning may have introduced variability and potential inaccuracies into the measurements. Consequently, the primary focus of this stage was observational rather than the acquisition of precise quantitative data.

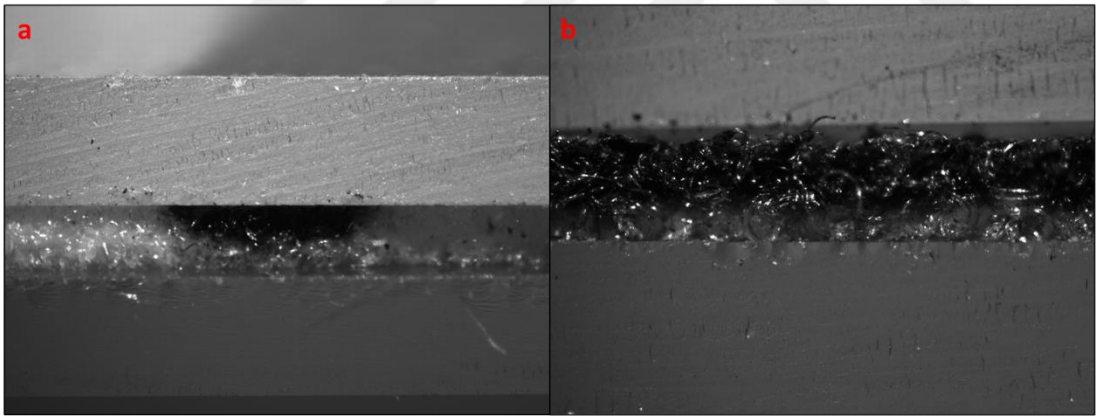

Figure 3.33 : a) Strain gauge arm, dissected in perpendicular to force direction. b) contact area section. dissected parallel to force direction.

As depicted in Figure 3.33 a, the ink within the textile specimens exhibits a parabolic distribution. This phenomenon can be attributed to a combination of misalignment during the layer printing process and the influence of capillary forces within the textile fibers. Figure 3.33 b highlights that the ink is distributed uniformly in textiles with no specific defects inside the boundary.

4. CONCLUSION

This study investigates the performance of graphene ink-based sensor patterns applied to textiles, specifically for use in respiration monitoring applications. The patterns evaluated include line, serpentine, strain gauge, and omnidirectional designs, each in two-layer configurations: 4x5 and 5x5. Through cyclic loading tests at 5% and 10% strain levels, key performance metrics, such as resistance change and GF, were analyzed to assess each pattern's sensitivity and stability.

With the results obtained, the selected ink composition and screen-printing method are suitable for the purpose of strain sensing. No significant deviations from the intended patterns were observed. However, especially with complex geometries like omnidirectional or strain gauges, it proved difficult to precisely align the patterns for each successive layer. This condition may affect the results adversely for measuring the sensing performance of these patterns. Likewise, especially integrating the strain gauge sensor into the testing system has some areas to improve. Because a slight misalignment from the fiber direction would affect all arms extending from the sensor, significantly resulting in performance loss, thus evaluating this geometry.

90T mesh is verified via optical imaging, and the obtained stencil aligns with theoretical calculations. This mesh size is optimal with no significant difficulties for the ink to pass through the mesh and disperse into the textile.

Compared to the pre-studies, using 4 layers compared to 5 and 30 mL of ink instead of 50 mL still yields reasonable results, which might save time and material. It was also observed that excessive ink still remains after usage. Therefore, even 20 mL of ink can be tested.

A Summary of average resistance is given in Figure 3.34 for geometry, layer composition, and strain level.

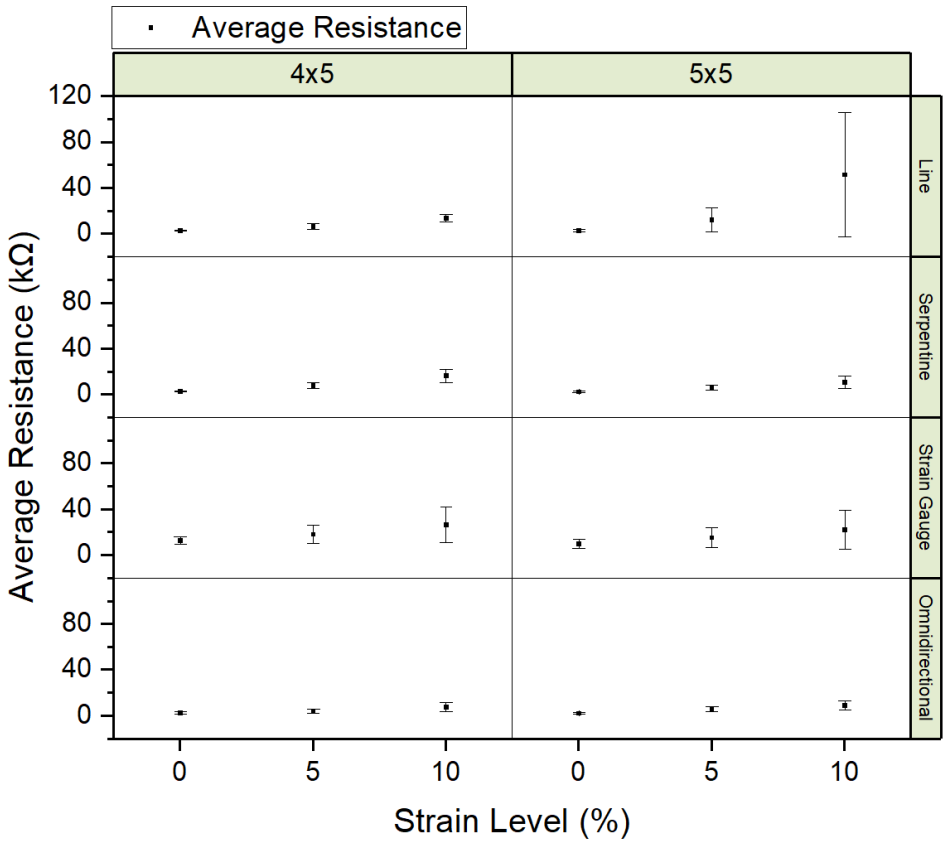

Figure 3.34 : Comparison of average resistances across the patterns.

In all geometries and layer compositions, resistance is increased along with strain level. All geometries show increased variability except the strain gauge – which shows a similar response - in both layer composition and strain levels. Increased resistance is expected with strain level, as generated microcracks hinder electron transport. In addition, the 5th layer contributes to the stiffness of the material, making it more brittle, hence giving way to crack generation during stretching. However, microcracks over the pattern for each specimen differ leading to increased variability in results.

Figure 3.35 shows the GF over layer composition and geometry for different strain levels. A conclusion can be drawn from resistance change that the addition of another layer may contribute to variability due to crack formation differences across the specimens. Increased GF is rather an expected result along with increased strain level as long as the material does not break down; since the microcrack generation is evident, it is expected that these cracks would widen as the strain increased. However, to safely assess this phenomenon would require advanced image techniques such as SEM.

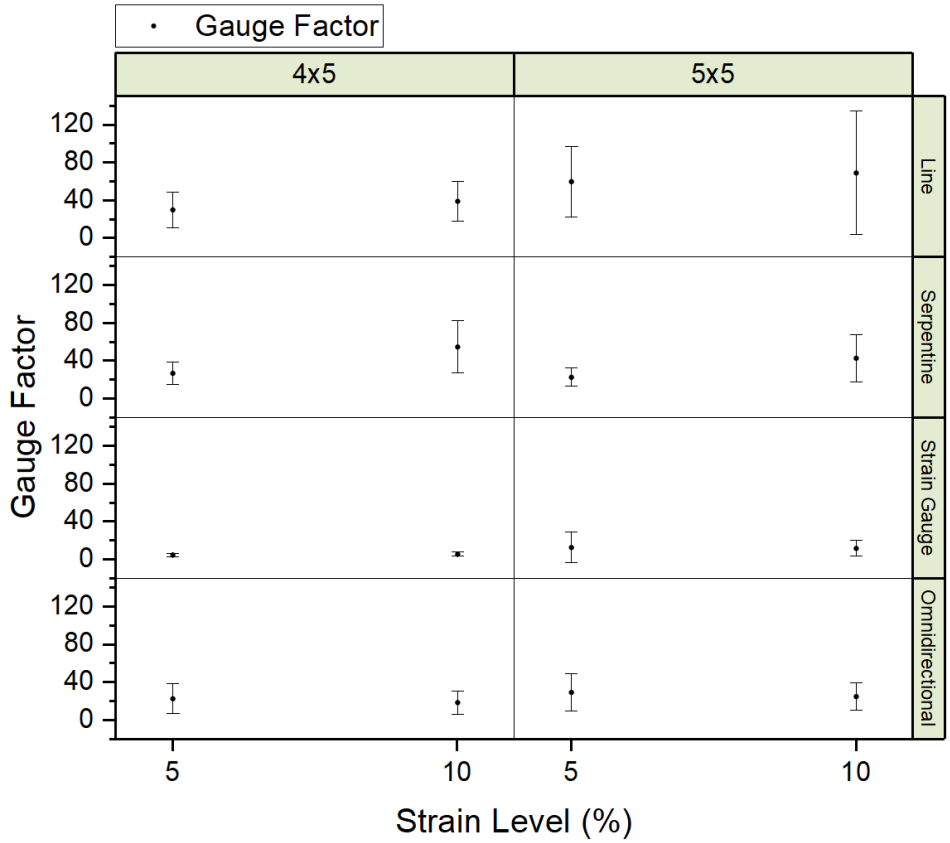

Figure 3.35 : Comparison of GFs across the patterns.

From all observations, it can be concluded that geometry is the main factor for the overall performance of the sensors. The line pattern exhibited stable cyclic behavior across both configurations (4x5 and 5x5), progressively increasing resistance as cyclic loading and strain levels increased. The GF for this pattern was generally consistent, though variations were observed with changes in layer configuration and strain levels. While this pattern demonstrated reliable sensitivity, its increased standard deviation in resistance and GF values at 10% strain suggests it may be less robust under higher strain conditions. Consequently, the line pattern may be suited for respiration monitoring where moderate sensitivity and stability are prioritized over high strain tolerance.

The serpentine pattern demonstrated slightly less sensitivity than the line pattern, especially in the 5x5 configuration. Mean resistance values increased notably with strain, and the GFs were also substantially higher compared to other geometries, particularly at 5% strain. However, this heightened sensitivity was associated with greater variability, as indicated by the elevated standard deviations in both resistance and GFs, particularly under cyclic loading at higher strain levels. This suggests that

while the serpentine pattern could detect subtle strain variations, potentially capturing finer respiratory movements, it may introduce inconsistencies when subjected to higher strain intensities or extended cyclic loading, possibly impacting long-term monitoring accuracy. Regardless, compared to line geometry, serpentine captures both sensitivity and stability.

Strain gauge pattern sensors exhibited a balanced response in terms of sensitivity and stability. The 5x5 layer configuration showed increased resistance and GFs compared to the 4x5 configuration, indicating enhanced sensitivity. However, the standard deviation of the GF at 10% strain increased, suggesting decreased consistency at higher strain levels. The strain gauge pattern thus appears appropriate for respiration monitoring applications that require a compromise between sensitivity and stability, particularly at lower strain levels where reliability is crucial (e.g infants, children of small age etc.)

The omnidirectional pattern demonstrated the moderate GFs among all sensor designs. This pattern showed similar results across both strain levels and layer configurations with similar and moderate variability. This suggests that an omnidirectional pattern is a suitable geometry that combines stability and sensitivity. Thus, the omnidirectional pattern could be valuable for applications where high sensitivity and reliability is required.

GF and resistance changes are studied over geometry, layer composition and strain levels. To assess the effect of these variables with better accuracy, analysis of variance (ANOVA) is a recommended method. Running ANOVA for one, two, and three factors revealed that geometry is the most significant factor influencing both GF and resistance change, establishing it as the key design parameter in the performance of graphene ink-based textile sensors. This insight is essential for practical applications such as wearable sensors and flexible electronics, where performance must meet specific sensitivity, stability, and durability criteria.

The serpentine geometry, with its inherent flexibility, proves particularly advantageous in wearables where the sensor needs to conform to the body's natural movements. This geometry allows the sensor to stretch and adapt to complex shapes while maintaining stable electrical properties, minimizing crack formation and providing stable resistance even under cyclic loading. Due to these attributes, the

serpentine pattern is best suited for applications requiring high sensitivity to deformation, such as wearable respiration or motion sensors, where it can accurately track subtle movements without compromising stability.

The omnidirectional geometry is another recommended pattern, offering balanced sensitivity and stability by evenly distributing strain across multiple directions. This characteristic makes it especially useful for detecting complex, multidirectional movements, such as those encountered in wearable devices used for joint monitoring or flexible electronics integrated into fabrics. By accommodating strain from various angles, the omnidirectional geometry is ideal for applications in real-time health monitoring where multidirectional strain sensing is required.

In contrast, while less adaptable than serpentine or omnidirectional configurations, line geometry is beneficial in applications requiring straightforward strain measurement along a single axis. This pattern provides reliable directional sensitivity and is advantageous in environments with predictable, linear strain, such as structural health monitoring applications, where strain is typically uniaxial. Its simplicity and stability in linear applications make the line geometry well-suited for straightforward monitoring tasks where reliability is prioritized over flexibility.

In summary, serpentine and omnidirectional geometries are recommended for wearable sensors where high sensitivity and flexibility are paramount due to their adaptability to body movement and reliable performance across various strain conditions. The line geometry, however, remains ideal for applications involving linear strain measurement, where the predictable directional response is beneficial.

Based on the results, there is still a potential to be realized especially with the geometrical shapes of the sensors. As an argument, adopting Murray's Law to geometrical shapes could be a path for achieving higher GFs. Murray's Law is derived from the Hagen–Poiseuille equation, where effective transport in nature follows a specific pattern. A similar concept can be found in the literature; one example in line with this work's interest is done by Kang et al. where a spider sensory system was studied for crack-based sensor [114]. Example geometries following the below equation are given in Figure 4.1.

$$r_i^3 = r_{i+1}^3 + r_{i+2}^3 \tag{4.1}$$

Where $i = 1$ refers to main branch radius and subsequent values refer the child branches.

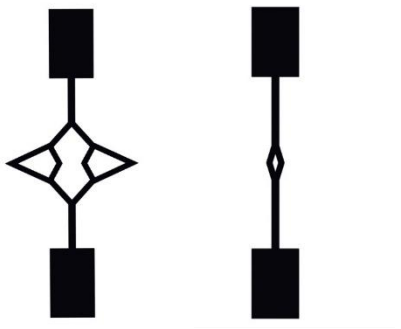

Figure 4.1 : Patterns where line thicknesses follow Murray's Law.

Given that brittleness and crack generation are related, geometries like cross-serpentine can be generated solely by changing the direction of the stencil as depicted in Figure 4.2. This might aid different thicknesses over the conducting path, controlling the stress concentration. This approach can give control over the crack mechanism as suggested by other studies such as done by Yong et al. [115]

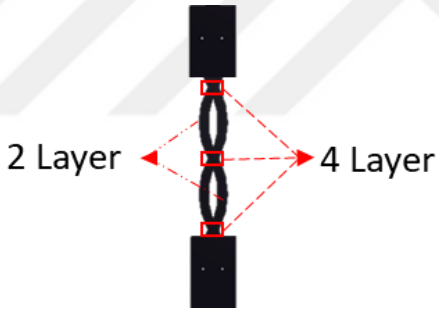

Figure 4.2 : Crosserpentine pattern of 4x5 layers.

In addition, the flake size of the graphene is an important parameter for conductivity. Current flake size is roughly around 1000 nm; a larger flake size might aid in improving the conductivity and keeping the structural integrity making layers less brittle.

Since the main purpose of this study is to capture respiratory movements, the testing system can be easily modified via a bevel gear or with a hydraulic apparatus to translate the movements from the x-axis to the z-axis with similar precision. This way, chest movement can be studied without expensive mannequins or respiratory simulators.

REFERENCES

[1] **M. Hollett and D. Bell,** "COVID-19," *Radiopaedia.org*, Jan. 2020, doi: 10.53347/RID-73913.

[2] **A. Hafeez, S. Ahmad, S. A. Siddqui, M. Ahmad, and S. Mishra,** "A Review of COVID-19 (Coronavirus Disease-2019) Diagnosis, Treatments and Prevention," *Eurasian J Med Oncol*, vol. 4, no. 2, pp. 116–125, 2020, doi: 10.14744/EJMO.2020.90853/PDF/.

[3] **R. Gopaul, J. Davis, L. Gangai, and L. Goetz,** "Practical Diagnostic Accuracy of Nasopharyngeal Swab Testing for Novel Coronavirus Disease 2019 (COVID-19)," *Western Journal of Emergency Medicine*, vol. 21, no. 6, p. 1, Sep. 2020, doi: 10.5811/WESTJEM.2020.8.48420.

[4] **M. L. Ranney, V. Griffeth, and A. K. Jha,** "Critical Supply Shortages — The Need for Ventilators and Personal Protective Equipment during the Covid-19 Pandemic," *New England Journal of Medicine*, vol. 382, no. 18, Apr. 2020, doi: 10.1056/NEJMP2006141/SUPPL_FILE/NEJMP2006141_DISCLOSURES.PDF.

[5] **A. S. Vohra, D. Khullar, R. Kaushal, and W. L. Schpero,** "Many Intensive Care Units Were Overloaded While Nearby Hospitals Had Excess Capacity During The COVID-19 Pandemic," *Health Aff (Millwood)*, vol. 42, no. 7, pp. 937–945, Jul. 2023, doi: 10.1377/HLTHAFF.2022.01657.

[6] **C. P. Hor *et al.*,** "MORBIDITY AND MORTALITY OUTCOMES FOR PATIENTS WITH MODERATE-TO-SEVERE COVID-19 DISEASES: A POST-HOSPITALIZATION FOLLOW-UP STUDY," *International Journal of Infectious Diseases*, vol. 130, pp. S152–S153, May 2023, doi: 10.1016/J.IJID.2023.04.376.

[7] **A. Kumar, B. Jatteppanvar, P. K. Panda, P. Dhangar, and Y. A. Bahurupi**, "Predictors of Mortality Among Post-COVID-19 Discharged Patients in Northern India: A Case-Control Study," *Cureus*, vol. 15, no. 3, Mar. 2023, doi: 10.7759/CUREUS.36883.

[8] **D. K. Rai and N. Sahay,** "Six-month Morbidity and Mortality in Patients after Recovery from COVID-19," *Indian J Crit Care Med*, vol. 26, no. 11, p. 1179, Nov. 2022, doi: 10.5005/JP-JOURNALS-10071-24347.

[9] **J. R. Camargo *et al.*,** "Development of conductive inks for electrochemical sensors and biosensors," *Microchemical Journal*, vol. 164, p. 105998, May 2021, doi: 10.1016/J.MICROC.2021.105998.

[10] **A. Beniwal, P. Ganguly, A. K. Aliyana, G. Khandelwal, and R. Dahiya,** "Screen-printed graphene-carbon ink based disposable humidity sensor with wireless communication," *Sens Actuators B Chem*, vol. 374, p. 132731, Jan. 2023, doi: 10.1016/J.SNB.2022.132731.

[11] **"Human Body-on-Chip platform enables in vitro prediction of drug behaviors in humans."** Accessed: Oct. 08, 2023. [Online]. Available: https://wyss.harvard.edu/news/human-body-on-chip-platform-enables-in-vitro-prediction-of-drug-behaviors-in-humans/

[12] **M. Sher, R. Zhuang, U. Demirci, and W. Asghar,** "Paper-based analytical devices for clinical diagnosis: recent advances in the fabrication techniques and sensing mechanisms," *Expert Rev Mol Diagn*, vol. 17, no. 4, pp. 351–366, Apr. 2017, doi: 10.1080/14737159.2017.1285228.

[13] **C. M. Leung *et al.*,** "A guide to the organ-on-a-chip," *Nature Reviews Methods Primers 2022 2:1*, vol. 2, no. 1, pp. 1–29, May 2022, doi: 10.1038/s43586-022-00118-6.

[14] **T. Loncar-Turukalo, E. Zdravevski, J. M. da Silva, I. Chouvarda, and V. Trajkovik,** "Literature on wearable technology for connected health: Scoping review of research trends, advances, and barriers," *J Med Internet Res*, vol. 21, no. 9, p. e14017, Sep. 2019, doi: 10.2196/14017.

[15] **L. A. Pradela-Filho *et al.*,** "Paper-based analytical devices for point-of-need applications," vol. 1, p. 3, doi: 10.1007/s00604-023-05764-5.

[16] **M. Sher, R. Zhuang, U. Demirci, and W. Asghar,** "Paper-based analytical devices for clinical diagnosis: recent advances in the fabrication techniques and sensing mechanisms," *Expert Rev Mol Diagn*, vol. 17, no. 4, pp. 351–366, Apr. 2017, doi: 10.1080/14737159.2017.1285228.

[17] **Y. Hou *et al.*,** "Recent Advances and Applications in Paper-Based Devices for Point-of-Care Testing," vol. 6, pp. 247–273, 2022, doi: 10.1007/s41664-021-00204-w.

[18] **X. Yang *et al.*,** "Textile fiber optic microbend sensor used for heartbeat and respiration monitoring," *IEEE Sens J*, vol. 15, no. 2, pp. 757–761, Feb. 2015, doi: 10.1109/JSEN.2014.2353640.

[19] **H. Chen *et al.*,** "A Wearable Daily Respiration Monitoring System Using PDMS-graphene Compound Tensile Sensor for Adult," *Proceedings of the Annual International Conference of the IEEE Engineering in Medicine and Biology Society, EMBS*, pp. 1269–1273, Jul. 2019, doi: 10.1109/EMBC.2019.8857144.

[20] **C. Sodini, L. Paglialonga, G. Antoniol, S. Perrone, N. Principi, and S. Esposito,** "Home Cardiorespiratory Monitoring in Infants at Risk for Sudden Infant Death Syndrome (SIDS), Apparent Life-Threatening Event (ALTE) or Brief Resolved Unexplained Event (BRUE)," *Life*, vol. 12, no. 6, Jun. 2022, doi: 10.3390/LIFE12060883.

[21] **C. Massaroni *et al.*,** "Respiratory Monitoring during Physical Activities with a Multi-Sensor Smart Garment and Related Algorithms," *IEEE Sens J*, vol. 20, no. 4, pp. 2173–2180, Feb. 2020, doi: 10.1109/JSEN.2019.2949608.

[22] **R. A. Chaudhry, L. Zarmer, K. West, and F. Chung,** "Obstructive Sleep Apnea and Risk of Postoperative Complications after Non-Cardiac Surgery," *J Clin Med*, vol. 13, no. 9, p. 2538, May 2024, doi: 10.3390/JCM13092538.

[23] **R. Ravichandran, E. Saba, K. Y. Chen, M. Goel, S. Gupta, and S. N. Patel,** "WiBreathe: Estimating respiration rate using wireless signals in natural settings in the home," *2015 IEEE International Conference on Pervasive Computing and Communications, PerCom 2015*, pp. 131–139, Jul. 2015, doi: 10.1109/PERCOM.2015.7146519.

[24] **G. Z. Liu, B. Y. Huang, and L. Wang,** "A Wearable Respiratory Biofeedback System Based on Generalized Body Sensor Network," *Telemedicine Journal and e-Health*, vol. 17, no. 5, p. 348, Jun. 2011, doi: 10.1089/TMJ.2010.0182.

[25] **C. Orphanidou,** "Derivation of respiration rate from ambulatory ECG and PPG using Ensemble Empirical Mode Decomposition: Comparison and fusion," *Comput Biol Med*, vol. 81, pp. 45–54, Feb. 2017, doi: 10.1016/J.COMPBIOMED.2016.12.005.

[26] **G. A, B. S, M. E, M. JE, C. WL, and S. P,** "Impedance pneumography. Comparison between chest impedance changes and respiratory volumines in 11 healthy volunteers," *Chest*, vol. 62, no. 4, p. 62, Jan. 1972, doi: 10.1378/CHEST.62.4.439.

[27] **K. S. Tan, R. Saatchi, H. Elphick, and D. Burke,** "Real-time vision based respiration monitoring system," *2010 7th International Symposium on Communication Systems, Networks and Digital Signal Processing, CSNDSP 2010*, pp. 770–774, 2010, doi: 10.1109/CSNDSP16145.2010.5580316.

[28] **A. Umeda *et al.*,** "Recent Insights into the Measurement of Carbon Dioxide Concentrations for Clinical Practice in Respiratory Medicine," *Sensors (Basel)*, vol. 21, no. 16, Aug. 2021, doi: 10.3390/S21165636.

[29] **K. Pan *et al.*,** "Sustainable production of highly conductive multilayer graphene ink for wireless connectivity and IoT applications", doi: 10.1038/s41467-018-07632-w.

[30] **M. Franco *et al.*,** "Environmentally Friendly Graphene-Based Conductive Inks for Multitouch Capacitive Sensing Surfaces," 2021, doi: 10.1002/admi.202100578.

[31] **G. Chen, Y. Li, M. Bick, and J. Chen,** "Smart Textiles for Electricity Generation," 2020, doi: 10.1021/acs.chemrev.9b00821.

[32] **X. Liao *et al.*,** "Flexible and highly sensitive strain sensors fabricated by pencil drawn for wearable monitor," *Adv Funct Mater*, vol. 25, no. 16, pp. 2395–2401, Apr. 2015, doi: 10.1002/ADFM.201500094.

[33] **M. Stoppa and A. Chiolerio,** "Wearable Electronics and Smart Textiles: A Critical Review," *Sensors*, vol. 14, pp. 11957–11992, 2014, doi: 10.3390/s140711957.

[34] **H. Jin, Y. S. Abu-Raya, and H. Haick,** "Advanced Materials for Health Monitoring with Skin-Based Wearable Devices," *Adv Healthc Mater*, vol. 6, no. 11, p. 1700024, Jun. 2017, doi: 10.1002/ADHM.201700024.

[35] **"GPUs Continue to Dominate the AI Accelerator Market for Now | InformationWeek."** Accessed: Aug. 12, 2024. [Online]. Available: https://www.informationweek.com/machine-learning-ai/gpus-continue-to-dominate-the-ai-accelerator-market-for-now

[36] **G. Hinton *et al.,*** "Deep neural networks for acoustic modeling in speech recognition: The shared views of four research groups," *IEEE Signal Process Mag*, vol. 29, no. 6, pp. 82–97, 2012, doi: 10.1109/MSP.2012.2205597.

[37] **S. Wang and R. M. Summers**, "Machine learning and radiology," *Med Image Anal*, vol. 16, no. 5, pp. 933–951, Jul. 2012, doi: 10.1016/J.MEDIA.2012.02.005.

[38] **Z. Zhang and E. Sejdić,** "Radiological images and machine learning: Trends, perspectives, and prospects," *Comput Biol Med*, vol. 108, pp. 354–370, May 2019, doi: 10.1016/J.COMPBIOMED.2019.02.017.

[39] **C. Tang *et al.,*** "Ultrasensitive textile strain sensors redefine wearable silent speech interfaces with high machine learning efficiency," *npj Flexible Electronics 2024 8:1*, vol. 8, no. 1, pp. 1–11, May 2024, doi: 10.1038/s41528-024-00315-1.

[40] **J. Andreu-Perez, D. R. Leff, H. M. D. Ip, and G. Z. Yang**, "From Wearable Sensors to Smart Implants-Toward Pervasive and Personalized Healthcare," *IEEE Trans Biomed Eng*, vol. 62, no. 12, pp. 2750–2762, Dec. 2015, doi: 10.1109/TBME.2015.2422751.

[41] **Y. Gao, L. Yu, J. C. Yeo, and C. T. Lim,** "Flexible Hybrid Sensors for Health Monitoring: Materials and Mechanisms to Render Wearability," *Advanced Materials*, vol. 32, no. 15, p. 1902133, Apr. 2020, doi: 10.1002/ADMA.201902133.

[42] **T. Q. Trung and N. E. Lee,** "Flexible and Stretchable Physical Sensor Integrated Platforms for Wearable Human-Activity Monitoringand Personal Healthcare," *Advanced Materials*, vol. 28, no. 22, pp. 4338–4372, Jun. 2016, doi: 10.1002/ADMA.201504244.

[43] **Y. J. Hong, H. Jeong, K. W. Cho, N. Lu, and D. H. Kim,** "Wearable and Implantable Devices for Cardiovascular Healthcare: from Monitoring to Therapy Based on Flexible and Stretchable Electronics," *Adv Funct Mater*, vol. 29, no. 19, p. 1808247, May 2019, doi: 10.1002/ADFM.201808247.

[44] **N. Lu, C. Lu, S. Yang, and J. Rogers,** "Highly Sensitive Skin-Mountable Strain Gauges Based Entirely on Elastomers," *Adv Funct Mater*, vol. 22, no. 19, pp. 4044–4050, Oct. 2012, doi: 10.1002/ADFM.201200498.

[45] **Y. Cotur, M. Kasimatis, M. Kaisti, S. Olenik, C. Georgiou, and F. Güder,** "Stretchable Composite Acoustic Transducer for Wearable Monitoring of Vital Signs," *Adv Funct Mater*, vol. 30, no. 16, Apr. 2020, doi: 10.1002/ADFM.201910288.

[46] **S. Chatterjee,** "Sustainable Electronic Waste Management and Recycling Process," *Am J Environ Engineer*, vol. 2, no. 1, pp. 23–33, Aug. 2012, doi: 10.5923/J.AJEE.20120201.05.

[47] **X. Zeng *et al.*,** "Current Status and Future Perspective of Waste Printed Circuit Boards Recycling," *Procedia Environ Sci*, vol. 16, pp. 590–597, Jan. 2012, doi: 10.1016/J.PROENV.2012.10.081.

[48] **X. Zhang, C. Jiang, J. Liang, and W. Wu,** "Electrode materials and device architecture strategies for flexible supercapacitors in wearable energy storage," 2021, doi: 10.1039/d0ta12299h.

[49] **D. Mabey, R. W. Peeling, A. Ustianowski, and M. D. Perkins,** "Diagnostics for the developing world," *Nature Reviews Microbiology 2004 2:3*, vol. 2, no. 3, pp. 231–240, Mar. 2004, doi: 10.1038/nrmicro841.

[50] **K. J. Land, D. I. Boeras, X.-S. Chen, A. R. Ramsay, and R. W. Peeling,** "REASSURED diagnostics to inform disease control strategies, strengthen health systems and improve patient outcomes", doi: 10.1038/s41564-018-0295-3.

[51] **N. Karim, S. Afroj, K. S. Novoselov, and S. G. Yeates,** "All Inkjet-printed Graphene-silver Composite Ink on textiles for Highly Conductive Wearable electronics Applications", doi: 10.1038/s41598-019-44420-y.

[52] **Y. Z. N. Htwe and M. Mariatti,** "Printed graphene and hybrid conductive inks for flexible, stretchable, and wearable electronics: Progress, opportunities, and challenges," 2022, doi: 10.1016/j.jsamd.2022.100435.

[53] **R. Islam, S. Afroj, C. Beach, A. J. Casson, K. S. Novoselov, and N. Karim,** "Fully printed and multifunctional graphene-based wearable e-textiles for personalized healthcare applications", doi: 10.1016/j.isci.2022.103945.

[54] **P. He *et al.*,** "Screen-Printing of a Highly Conductive Graphene Ink for Flexible Printed Electronics," 2019, doi: 10.1021/acsami.9b04589.

[55] **H. Chen *et al.*,** "Advances in graphene-based flexible and wearable strain sensors," *Chemical Engineering Journal*, vol. 464, p. 142576, May 2023, doi: 10.1016/J.CEJ.2023.142576.

[56] **A. L. . Window,** *Strain gauge technology*. Elsevier Applied Science, 1992. Accessed: Aug. 05, 2024. [Online]. Available: https://link.springer.com/book/9781851668649

[57] **C. Luo, B. Tian, Q. Liu, Y. Feng, and W. Wu,** "One-Step-Printed, Highly Sensitive, Textile-Based, Tunable Performance Strain Sensors for Human Motion Detection," *Adv Mater Technol*, vol. 5, no. 2, Feb. 2020, doi: 10.1002/ADMT.201900925.

[58] **T. Q. Trung and N. E. Lee,** "Flexible and Stretchable Physical Sensor Integrated Platforms for Wearable Human-Activity Monitoringand Personal Healthcare," *Advanced Materials*, vol. 28, no. 22, pp. 4338–4372, Jun. 2016, doi: 10.1002/ADMA.201504244.

[59] **S. Y. Kim *et al.*,** "Piezoresistive characteristics of nanocarbon composite strain sensor by its longitudinal pattern design," *Applied Sciences (Switzerland)*, vol. 11, no. 13, 2021, doi: 10.3390/app11135760.

[60] **P. J. de Pablo, C. Gómez-Navarro, J. Colchero, J. Gómez-Herrero, A. M. Baró, and P. A. Serena,** "Nonlinear Resistance versus Length in Single-Walled Carbon Nanotubes," *Phys Rev Lett*, vol. 88, no. 3, p. 036804, Jan. 2002, doi: 10.1103/PhysRevLett.88.036804.

[61] **C. S. Smith,** "Piezoresistance Effect in Germanium and Silicon," *Physical Review*, vol. 94, no. 1, p. 42, Apr. 1954, doi: 10.1103/PhysRev.94.42.

[62] **"Introduction to micro mechanical transducers,"** *Handbook of Sensors and Actuators*, vol. 8, pp. 1–21, Jan. 2000, doi: 10.1016/S1386-2766(00)80015-8.

[63] **J. Zhou *et al.*,** "Multiscale and hierarchical wrinkle enhanced graphene/Ecoflex sensors integrated with human-machine interfaces and cloud-platform," *npj Flexible Electronics 2022 6:1*, vol. 6, no. 1, pp. 1–11, Jul. 2022, doi: 10.1038/s41528-022-00189-1.

[64] **X. Li *et al.*,** "Stretchable and highly sensitive graphene-on-polymer strain sensors," *Sci Rep*, vol. 2, 2012, doi: 10.1038/srep00870.

[65] **X. Li, T. Hua, and B. Xu,** "Electromechanical properties of a yarn strain sensor with graphene-sheath/polyurethane-core," *Carbon N Y*, vol. 118, pp. 686–698, Jul. 2017, doi: 10.1016/J.CARBON.2017.04.002.

[66] **M. Amjadi, A. Pichitpajongkit, S. Lee, S. Ryu, and I. Park,** "Highly stretchable and sensitive strain sensor based on silver nanowire-elastomer nanocomposite," *ACS Nano*, vol. 8, no. 5, pp. 5154–5163, May 2014, doi: 10.1021/NN501204T/SUPPL_FILE/NN501204T_SI_003.AVI.

[67] **J. Hicks, A. Behnam, and A. Ural,** "A computational study of tunneling-percolation electrical transport in graphene-based nanocomposites," *Appl Phys Lett*, vol. 95, no. 21, p. 213103, Nov. 2009, doi: 10.1063/1.3267079/118159.

[68] **A. B. Oskouyi, U. Sundararaj, and P. Mertiny,** "Tunneling Conductivity and Piezoresistivity of Composites Containing Randomly Dispersed Conductive Nano-Platelets," *Materials 2014, Vol. 7, Pages 2501-2521*, vol. 7, no. 4, pp. 2501–2521, Mar. 2014, doi: 10.3390/MA7042501.

[69] **I. J. Fernandes *et al.*,** "Silver nanoparticle conductive inks: synthesis, characterization, and fabrication of inkjet-printed flexible electrodes," *Scientific Reports 2020 10:1*, vol. 10, no. 1, pp. 1–11, Jun. 2020, doi: 10.1038/s41598-020-65698-3.

[70] **H. M. Ren *et al.*,** "One-Step Preparation of Silver Hexagonal Microsheets as Electrically Conductive Adhesive Fillers for Printed Electronics," *ACS Appl Mater Interfaces*, vol. 7, no. 24, pp. 13685–13692, Jun. 2015, doi: 10.1021/ACSAMI.5B03571/SUPPL_FILE/AM5B03571_SI_001.PDF.

[71] **Y. Li, K. S. Moon, and C. P. Wong,** "Electronics without lead," *Science (1979)*, vol. 308, no. 5727, pp. 1419–1420, Jun. 2005, doi: 10.1126/SCIENCE.1110168/ASSET/B01346F3-AD74-40E5-9C97-F11FBB138BE5/ASSETS/SCIENCE.1110168.FP.PNG.

[72] **Y. Z. N. Htwe and M. Mariatti,** "Printed graphene and hybrid conductive inks for flexible, stretchable, and wearable electronics: Progress, opportunities, and challenges," *Journal of Science: Advanced Materials and Devices*, vol. 7, no. 2, p. 100435, Jun. 2022, doi: 10.1016/J.JSAMD.2022.100435.

[73] **C. Yang, C. P. Wong, and M. M. F. Yuen,** "Printed electrically conductive composites: conductive filler designs and surface engineering," *J Mater Chem C Mater*, vol. 1, no. 26, pp. 4052–4069, Jun. 2013, doi: 10.1039/C3TC00572K.

[74] **S. M. F. Cruz, L. A. Rocha, J. C. Viana, S. M. F. Cruz, L. A. Rocha, and J. C. Viana,** "Printing Technologies on Flexible Substrates for Printed Electronics," *Flexible Electronics*, Jul. 2018, doi: 10.5772/INTECHOPEN.76161.

[75] **F. Torrisi *et al.*,** "Inkjet-printed graphene electronics," *ACS Nano*, vol. 6, no. 4, pp. 2992–3006, Apr. 2012, doi: 10.1021/NN2044609/ASSET/IMAGES/LARGE/NN-2011-044609_0015.JPEG.

[76] **S. Zhao, Z. Zhao, Z. Yang, L. L. Ke, S. Kitipornchai, and J. Yang,** "Functionally graded graphene reinforced composite structures: A review," *Eng Struct*, vol. 210, p. 110339, May 2020, doi: 10.1016/J.ENGSTRUCT.2020.110339.

[77] **V. Abhinav K, V. K. Rao R, P. S. Karthik, and S. P. Singh,** "Copper conductive inks: synthesis and utilization in flexible electronics," *RSC Adv*, vol. 5, no. 79, pp. 63985–64030, Jul. 2015, doi: 10.1039/C5RA08205F.

[78] **I. E. Stewart, M. Jun Kim, and B. J. Wiley,** "Effect of morphology on the electrical resistivity of silver nanostructure films," *ACS Appl Mater Interfaces*, vol. 9, no. 2, pp. 1870–1879, Jan. 2017, doi: 10.1021/ACSAMI.6B12289/ASSET/IMAGES/LARGE/AM-2016-12289J_0007.JPEG.

[79] **P. R. Wallace,** "The Band Theory of Graphite," *Physical Review*, vol. 71, no. 9, p. 622, May 1947, doi: 10.1103/PhysRev.71.622.

[80] **K. S. Novoselov *et al.*,** "Electric field in atomically thin carbon films," *Science (1979)*, vol. 306, no. 5696, pp. 666–669, Oct. 2004, doi: 10.1126/SCIENCE.1102896/SUPPL_FILE/NOVOSELOV.SOM.PDF.

[81] **N. Roussel, G. Ovarlez, S. Garrault, and C. Brumaud,** "The origins of thixotropy of fresh cement pastes," *Cem Concr Res*, vol. 42, no. 1, pp. 148–157, Jan. 2012, doi: 10.1016/J.CEMCONRES.2011.09.004.

[82] **N. Roussel,** "A thixotropy model for fresh fluid concretes: Theory, validation and applications," *Cem Concr Res*, vol. 36, no. 10, pp. 1797–1806, Oct. 2006, doi: 10.1016/J.CEMCONRES.2006.05.025.

[83] **H. A. Barnes,** "Thixotropy—a review," *J Nonnewton Fluid Mech*, vol. 70, no. 1–2, pp. 1–33, May 1997, doi: 10.1016/S0377-0257(97)00004-9.

[84] **Y. Liu, H. Zhu, L. Xing, Q. Bu, D. Ren, and B. Sun,** "Recent advances in inkjet-printing technologies for flexible/wearable electronics," *Nanoscale*, vol. 15, no. 13, pp. 6025–6051, Mar. 2023, doi: 10.1039/D2NR05649F.

[85] **Y. Chu *et al.*,** "Printed Diodes: Materials Processing, Fabrication, and Applications," *Advanced Science*, vol. 6, no. 6, p. 1801653, Mar. 2019, doi: 10.1002/ADVS.201801653.

[86] **W. Wu,** "Inorganic nanomaterials for printed electronics: A review," Jun. 14, 2017, *Royal Society of Chemistry*. doi: 10.1039/c7nr01604b.

[87] **G. Grau, J. Cen, H. Kang, R. Kitsomboonloha, W. J. Scheideler, and V. Subramanian,** "Gravure-printed electronics: recent progress in tooling development, understanding of printing physics, and realization of printed devices," *Flexible and Printed Electronics*, vol. 1, no. 2, p. 023002, Jun. 2016, doi: 10.1088/2058-8585/1/2/023002.

[88] **H. Li and J. Liang,** "Recent Development of Printed Micro-Supercapacitors: Printable Materials, Printing Technologies, and Perspectives," *Advanced Materials*, vol. 32, no. 3, Jan. 2020, doi: 10.1002/ADMA.201805864.

[89] **O. A. Basaran, H. Gao, and P. P. Bhat,** "Nonstandard inkjets," *Annu Rev Fluid Mech*, vol. 45, no. Volume 45, 2013, pp. 85–113, Jan. 2013, doi: 10.1146/ANNUREV-FLUID-120710-101148/CITE/REFWORKS.

[90] **K. Yan, J. Li, L. Pan, and Y. Shi,** "Inkjet printing for flexible and wearable electronics," Dec. 01, 2020, *American Institute of Physics Inc.* doi: 10.1063/5.0031669.

[91] **T. H. J. Van Osch, J. Perelaer, A. W. M. De Laat, and U. S. Schubert,** "Inkjet Printing of Narrow Conductive Tracks on Untreated Polymeric Substrates," *Advanced Materials*, vol. 20, no. 2, pp. 343–345, Jan. 2008, doi: 10.1002/ADMA.200701876.

[92] **J. Z. Wang, Z. H. Zheng, H. W. Li, W. T. S. Huck, and H. Sirringhaus,** "Dewetting of conducting polymer inkjet droplets on patterned surfaces," *Nat Mater*, vol. 3, no. 3, pp. 171–176, 2004, doi: 10.1038/NMAT1073.

[93] **T. M. Lee *et al.*,** "Drop-on-demand solder droplet jetting system for fabricating microstructure," *IEEE Transactions on Electronics Packaging Manufacturing*, vol. 31, no. 3, pp. 202–210, Jul. 2008, doi: 10.1109/TEPM.2008.926285.

[94] **T. Kawase, H. Sirringhaus, R. H. Friend, and T. Shimoda,** "Inkjet Printed Via-Hole Interconnections and Resistors for All-Polymer Transistor Circuits", doi: 10.1002/1521-4095.

[95] **A. Rida, L. Yang, R. Vyas, and M. M. Tentzeris,** "Conductive inkjet-printed antennas on flexible low-cost paper-based substrates for RFID and WSN applications," *IEEE Antennas Propag Mag*, vol. 51, no. 3, pp. 13–23, 2009, doi: 10.1109/MAP.2009.5251188.

[96] **F. C. Krebs,** "Fabrication and processing of polymer solar cells: A review of printing and coating techniques," *Solar Energy Materials and Solar Cells*, vol. 93, no. 4, pp. 394–412, Apr. 2009, doi: 10.1016/J.SOLMAT.2008.10.004.

[97] **L. Gonzalez-Macia and A. J. Killard,** "Screen printing and other scalable point of care (POC) biosensor processing technologies," *Medical Biosensors for Point of Care (POC) Applications*, pp. 69–98, Jan. 2017, doi: 10.1016/B978-0-08-100072-4.00004-6.

[98] **R. R. Søndergaard, M. Hösel, and F. C. Krebs,** "Roll-to-Roll fabrication of large area functional organic materials," *J Polym Sci B Polym Phys*, vol. 51, no. 1, pp. 16–34, Jan. 2013, doi: 10.1002/POLB.23192.

[99] **"Handbook of Print Media,"** *Print and Paper Europe*, vol. 13, no. 6, p. 35, Sep. 2001, doi: 10.1007/978-3-540-29900-4/COVER.

[100] **F. Chen, D. Varghese, S. T. Mcdermott, I. George, L. Geng, and D. H. Adamson,** "Interface-exfoliated graphene-based conductive screen-printing inks: low-loading, low-cost, and additive-free," 2020, doi: 10.1038/s41598-020-74821-3.

[101] **F. Zhao *et al.*,** "Watered-Based Graphene Dispersion Stabilized by a Graft Co-Polymer for Electrically Conductive Screen Printing," *Polymers (Basel)*, vol. 15, no. 2, p. 356, Jan. 2023, doi: 10.3390/POLYM15020356/S1.

[102] **L. Liu, Z. Shen, X. Zhang, and H. Ma,** "Highly conductive graphene/carbon black screen printing inks for flexible electronics," *J Colloid Interface Sci*, vol. 582, pp. 12–21, 2021, doi: 10.1016/j.jcis.2020.07.106.

[103] **J. H. Lee, P. A. Dzagbletey, M. Jang, J.-Y. Chung, and J.-H. So,** "Flat Yarn Fabric Substrates for Screen-Printed Conductive Textiles," 2020, doi: 10.1002/adem.202000722.

[104] **W. Yin, D.-H. Lee, J. Choi, C. Park, and S. M. Cho,** "Screen printing of silver nanoparticle suspension for metal interconnects," *Korean J. Chem. Eng*, vol. 25, no. 6, pp. 1358–1361, 2008.

[105] **H. Hong, L. Jiang, H. Tu, J. Hu, and X. Yan,** "Formulation of UV curable nano-silver conductive ink for direct screen-printing on common fabric substrates for wearable electronic applications," *Smart Mater Struct*, vol. 30, no. 4, p. 045001, Feb. 2021, doi: 10.1088/1361-665X/ABE4B3.

[106] **I. Ibanez Labiano, D. Arslan, E. Ozden Yenigun, A. Asadi, H. Cebeci, and A. Alomainy**, "Screen Printing Carbon Nanotubes Textiles Antennas for Smart Wearables," *Sensors (Basel)*, vol. 21, no. 14, p. 4934, Jul. 2021, doi: 10.3390/S21144934/S1.

[107] **J. Ferri, R. Llinares Llopis, J. Moreno, J. Vicente Lidón-Roger, and E. Garcia-Breijo,** "An investigation into the fabrication parameters of screen-printed capacitive sensors on e-textiles," *Textile Research Journal*, vol. 90, no. 15–16, pp. 1749–1769, Aug. 2020, doi: 10.1177/0040517519901016/FORMAT/EPUB.

[108] **N. Zavanelli and W.-H. Yeo,** "Advances in Screen Printing of Conductive Nanomaterials for Stretchable Electronics," 2021, doi: 10.1021/acsomega.1c00638.

[109] **N. Karim, S. Afroj, S. Tan, K. S. Novoselov, and S. G. Yeates,** "All Inkjet-Printed Graphene-Silver Composite Ink on Textiles for Highly Conductive Wearable Electronics Applications," *Scientific Reports 2019 9:1*, vol. 9, no. 1, pp. 1–10, May 2019, doi: 10.1038/s41598-019-44420-y.

[110] **Y. Zhou *et al.*,** "Significant stretchability enhancement of a crack-based strain sensor combined with high sensitivity and superior durability for motion monitoring," *ACS Appl Mater Interfaces*, vol. 11, no. 7, pp. 7405–7414, Feb. 2019, doi: 10.1021/ACSAMI.8B20768/SUPPL_FILE/ AM8B207 68_SI_006.AVI.

[111] **G. Shi *et al.*,** "Highly Sensitive, Wearable, Durable Strain Sensors and Stretchable Conductors Using Graphene/Silicon Rubber Composites," *Adv Funct Mater*, vol. 26, no. 42, pp. 7614–7625, Nov. 2016, doi: 10.1002/ADFM.201602619.

[112] **X. Chen *et al.*,** "A Single-material-printed, Low-cost design for a Carbon-based fabric strain sensor," *Mater Des*, vol. 221, p. 110926, Sep. 2022, doi: 10.1016/J.MATDES.2022.110926.

[113] **X. Cheng, J. Cai, J. Xu, and D. Gong,** "High-Performance Strain Sensors Based on Au/Graphene Composite Films with Hierarchical Cracks for Wide Linear-Range Motion Monitoring," *ACS Applied Materials and Interfaces* , vol. 14, no. 34, pp. 39230–39239, Aug. 2022, doi: 10.1021/ACSAMI.2C10226/SUPPL_FILE/AM2C10226_SI_004.MP4.

[114] **D. Kang *et al.*,** "Ultrasensitive mechanical crack-based sensor inspired by the spider sensory system," *Nature 2014 516:7530*, vol. 516, no. 7530, pp. 222–226, Dec. 2014, doi: 10.1038/nature14002.

[115] **Y. W. Choi *et al.*,** "Ultra-sensitive Pressure sensor based on guided straight mechanical cracks," *Scientific Reports 2017 7:1*, vol. 7, no. 1, pp. 1–8, Jan. 2017, doi: 10.1038/srep40116.

APPENDICES

APPENDIX A: Overall View of Important Figures

APPENDIX B: REASSURED Concept

APPENDIX C: MATLAB Code

APPENDIX A: Overall View of Important Figures

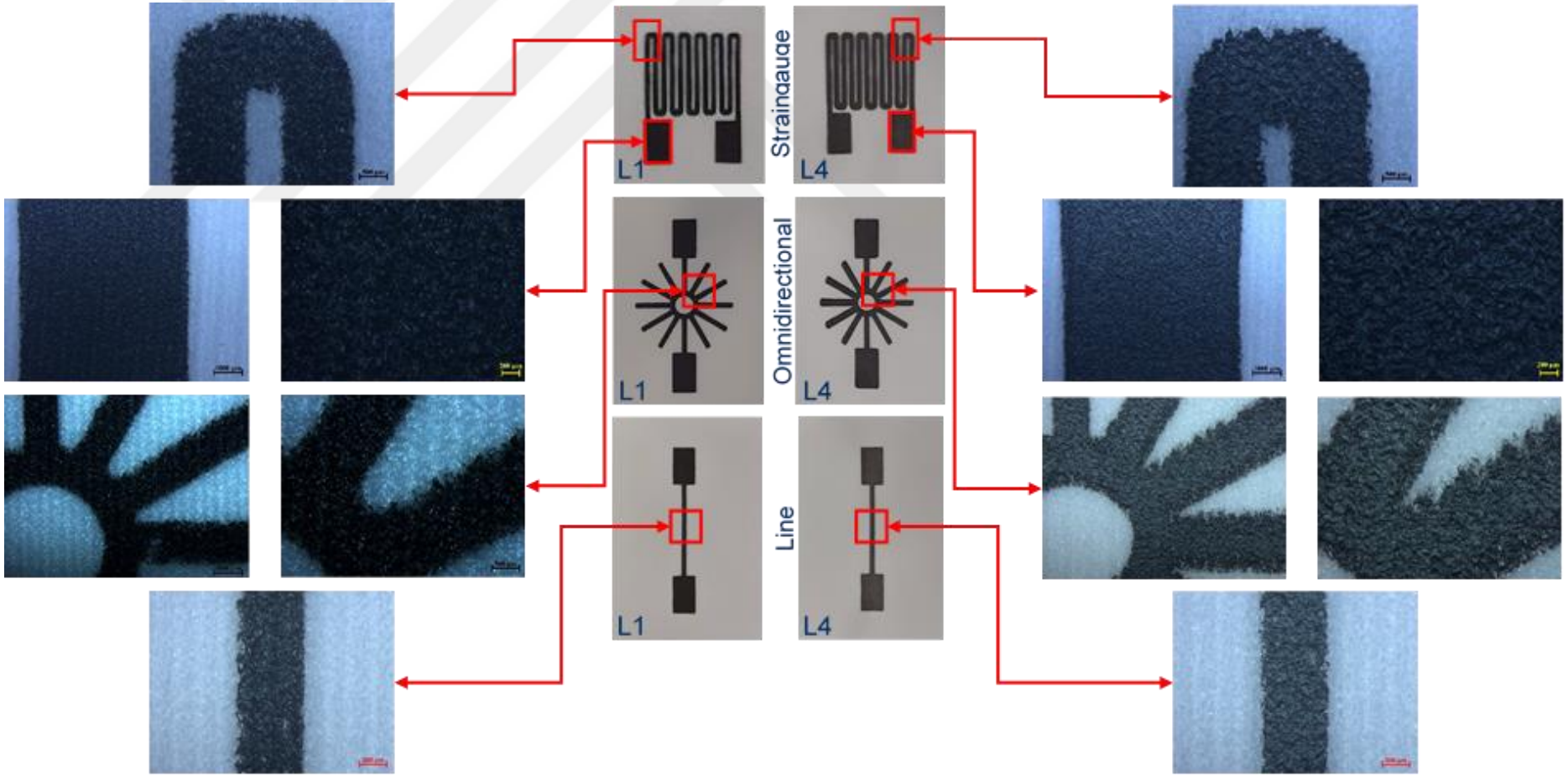

Figure A.1 : Overall view of important figures.

APPENDIX B: REASSURED Concept

Table B.1 : REASSURED Concept.

Criteria		Description
R	Real-time connectivity	Tests are connected and/or a reader or mobile phone is used to power the reaction and/or read test results to provide required data to decision makers
E	Ease of specimen collection	Tests should be designed for use with non-invasive specimens
A	Affordable	Tests are affordable to end-users and the health system.
S	Sensitive	Avoid false negatives.
S	Specific	Avoid false positives.
U	User-friendly	Procedure of testing is simple — can be performed in a few steps, requiring minimum training.
R	Rapid and robust	Results are available to ensure treatment of patient at first visit (typically, this means results within 15 min to 2 hours); the tests can survive the supply chain without requiring additional transport and storage conditions such as refrigeration.
E	Equipment free or simple. Environmentally friendly	Ideally the test does not require any special equipment or can be operated in very simple devices that use solar or battery power. Completed tests are easy to dispose and manufactured from recyclable materials.
D	Deliverable to end-users	Accessible to those who need the tests the most.

APPENDIX C: MATLAB Code

```
clc; clear; % Temizle

% Dosyaları kontrol edip var olanları sil
outputFiles = {'Xlist.txt', 'Ylist.txt', 'X_avg.txt', 'Y_avg.txt',
'GaugeFactor.txt', 'Best_Results.txt'};
for i = 1:length(outputFiles)
    if isfile(outputFiles{i})
        delete(outputFiles{i});
    end
end

% TXT dosyalarını listele
files = dir('*.txt');
pcname = "cysnx"; % Bilgisayar adı
strain = 0.1; % Gerilme (Strain)
smoothFactor_range = 0.001:0.002:0.6; % SmoothFactor değer aralığı
avgnumber_range = 2:1:4; % avgnumber değer aralığı
ratio_threshold = 0.1; % GFSTD / GFMEAN oranı eşiği

% Zaman ve dosya isimlerini depolamak için boş diziler oluştur
totaltimes = [];
names = {};

% Zaman hesaplama ve veri yükleme
for id = 1:length(files)
    % Dosya adını parçala
    [~, f, ~] = fileparts(files(id).name);
    R = strsplit(f, '_');
    R_time = strsplit(R{end}, '-');
    timeParts = strsplit(R_time{3}, ' ');

    % Bilgisayar adına göre tarih formatı ayarlaması
    if pcname == "cysnx"
        R_date = strsplit(R{end-1}, '-'); % Ay-gün-yıl
        totalsec = timeToSeconds(R_time, timeParts, R_date, 'PM/AM');
    else
        R_date = strsplit(R{end-1}, '.'); % Gün-ay-yıl
        totalsec = timeToSeconds(R_time, timeParts, R_date);
    end

    % Zaman ve isimleri kaydet
    names{id} = f;
    totaltimes = [totaltimes totalsec];
end

% Zaman sırasına göre dosya isimlerini sırala
[sortedTimes, idx] = sort(totaltimes);
sortedFiles = names(idx);

% Verileri sırayla yükle ve birleştir
[Xlist, Ylist] = loadData(files, sortedFiles);

% En iyi GFMEAN ve GFSTD için arama (GFSTD / GFMEAN <= ratio_threshold)
bestGFSTD = Inf;
bestGFMEAN = -Inf;
bestSmoothFactor = 0;
bestAvgnumber = 0;
```

```
bestRatio = Inf;
bestGaugeFactor = [];

for smoothFactor = smoothFactor_range
    for avgnumber = avgnumber_range
        % Verileri yumuşatma ve ortalama alma
        Ysmooth = smoothdata(Ylist, 'SmoothingFactor', smoothFactor);
        Y_avg = movingAverage(Ysmooth, avgnumber);

        % Tepe ve dip noktalarını bul
        [maxlist, minlist] = findPeaksAndTroughs(Y_avg);

        % Gauge faktörünü hesapla
        gaugeFactor = calculateGaugeFactor(maxlist, minlist, Ylist(1),
strain);

        % GFSTD ve GFMEAN hesapla
        GFSTD = std(gaugeFactor);
        GFMEAN = mean(gaugeFactor);

        % GFSTD / GFMEAN oranını hesapla
        ratio = GFSTD / GFMEAN;

        % Oran ratio_threshold'ün altında kalacak şekilde en iyi sonucu
bul
        if ratio <= ratio_threshold && GFMEAN >= bestGFMEAN
            bestGFSTD = GFSTD;
            bestGFMEAN = GFMEAN;
            bestSmoothFactor = smoothFactor;
            bestAvgnumber = avgnumber;
            bestRatio = ratio;
            bestGaugeFactor = gaugeFactor; % En iyi gaugeFactor'u sakla
        end
    end
end

% En iyi değerlerle tekrar gaugeFactor hesapla
Ysmooth = smoothdata(Ylist, 'SmoothingFactor', bestSmoothFactor);
Y_avg = movingAverage(Ysmooth, bestAvgnumber);

% X_avg değerini Y_avg ile uyumlu hale getirmek için Xlist'in de
ortalamasını al
X_avg = movingAverage(Xlist, bestAvgnumber); % X ortalama verileri

% Xlist, Ylist, X_avg ve Y_avg verilerini virgülle ayrılmış olarak txt
dosyalara yazma

% Xlist.txt ve Ylist.txt dosyalarına ham verileri yazma
fid_xlist = fopen('Xlist.txt', 'w');
fid_ylist = fopen('Ylist.txt', 'w');
fprintf(fid_xlist, '%s\n', strrep(sprintf('%.4f\n', Xlist), '.', ',')); %
Xlist verileri virgül ile
fprintf(fid_ylist, '%s\n', strrep(sprintf('%.4f\n', Ylist), '.', ',')); %
Ylist verileri virgül ile
fclose(fid_xlist);
fclose(fid_ylist);

% X_avg.txt ve Y_avg.txt dosyalarına ortalama verileri yazma
fid_x_avg = fopen('X_avg.txt', 'w');
```

```
fid_y_avg = fopen('Y_avg.txt', 'w');
fprintf(fid_x_avg, '%s\n', strrep(sprintf('%.4f\n', X_avg), '.', ',')); %
X_avg verileri virgül ile
fprintf(fid_y_avg, '%s\n', strrep(sprintf('%.4f\n', Y_avg), '.', ',')); %
Y_avg verileri virgül ile
fclose(fid_x_avg);
fclose(fid_y_avg);

% En iyi gaugeFactor'ları virgülle ayrılmış ve ondalık ayırıcı olarak
virgül kullanarak gaugeFactor.txt dosyasına yazma
fid = fopen('GaugeFactor.txt', 'w');
fprintf(fid, '%s\n', strrep(sprintf('%.4f\n', bestGaugeFactor), '.',
','')); % En iyi gaugeFactor verileri virgül ile
fclose(fid);

% Sonuçları yazdır
fprintf('En iyi Avgnumber: %d\n', bestAvgnumber);
fprintf('En iyi SmoothFactor: %.2f\n', bestSmoothFactor);
fprintf('En iyi GFMEAN: %.4f\n', bestGFMEAN);
fprintf('En iyi GFSTD: %.4f\n', bestGFSTD);
fprintf('GFSTD / GFMEAN oranı: %.4f\n', bestRatio);

% Sonuçları görselleştir ve yüksek çözünürlükte kaydet

% Ham ve ortalama verilerin olduğu grafik
figure;
plot(Xlist, Ylist, '-ok', 'MarkerSize', 3, 'MarkerFaceColor', 'k'); % Ham
veriler (siyah çizgi ve dolu nokta)
hold on;
plot(X_avg, Y_avg, '-or', 'MarkerSize', 3, 'MarkerFaceColor', 'r'); %
Ortalama veriler (kırmızı çizgi ve dolu nokta)
legend('Ham Veri', 'Ortalama Veri');
title('Ham vs Ortalama');
xlabel('Zaman (s)');
ylabel('Direnç');
box on; % Üst ve sağ barlar
exportgraphics(gcf, 'En_iyi_olcum_sonuclari.png', 'Resolution', 600); %
Yüksek çözünürlükte PNG formatında kaydedin

% Sadece yumuşatılmış verilerin olduğu grafik
figure;
plot(Xlist, Ysmooth, '-og', 'MarkerSize', 3, 'MarkerFaceColor', 'r'); %
Yumuşatılmış veriler (kırmızı çizgi ve dolu nokta)
legend('Yumuşatılmış');
title('Yumuşatılmış Veriler');
xlabel('Zaman (s)');
ylabel('Direnç');
box on; % Üst ve sağ barlar
exportgraphics(gcf, 'Yumusatilmis_olcum_sonuclari.png', 'Resolution',
600); % Yüksek çözünürlükte PNG formatında kaydedin

% 600-800 saniyeler arasındaki verilerin seçilmesi
index_range = Xlist >= 600 & Xlist <= 800;
index_range_avg = X_avg >= 600 & X_avg <= 800;

% 600-800 saniyeler arası ham ve ortalama verilerin olduğu grafik
figure;
plot(Xlist(index_range), Ylist(index_range), '-ok', 'MarkerSize', 3,
'MarkerFaceColor', 'k'); % Ham veriler (siyah çizgi ve dolu nokta)
```

```
hold on;
plot(X_avg(index_range_avg), Y_avg(index_range_avg), '-or', 'MarkerSize',
3, 'MarkerFaceColor', 'r'); % Ortalama veriler (kırmızı çizgi ve dolu
nokta)
legend('Ham Veri (600-800 s)', 'Ortalama Veri (600-800 s)');
title('600-800 Saniyeler Arası Direnç');
xlabel('Zaman (s)');
ylabel('Direnç');
box on; % Üst ve sağ barlar
exportgraphics(gcf, '600_800_saniyeler_arasi_olcum_sonuclari.png',
'Resolution', 600); % Yüksek çözünürlükte PNG formatında kaydedin

% 600-800 saniyeler arası sadece yumuşatılmış verilerin olduğu grafik
figure;
plot(Xlist(index_range), Ysmooth(index_range), '-og', 'MarkerSize', 3,
'MarkerFaceColor', 'r'); % Yumuşatılmış veriler (kırmızı çizgi ve dolu
nokta)
legend('Yumuşatılmış (600-800 s)');
title('600-800 Saniyeler Arası Yumuşatılmış Direnç');
xlabel('Zaman (s)');
ylabel('Direnç');
box on; % Üst ve sağ barlar
exportgraphics(gcf,
'600_800_saniyeler_arasi_yumusatilmis_olcum_sonuclari.png', 'Resolution',
600); % Yüksek çözünürlükte PNG formatında kaydedin

% En iyi sonuçları Best_Results.txt dosyasına yazma
fid_best_results = fopen('Best_Results.txt', 'w');
fprintf(fid_best_results, 'En iyi Avgnumber: %d\n', bestAvgnumber);
fprintf(fid_best_results, 'En iyi SmoothFactor: %.2f\n',
bestSmoothFactor);
fprintf(fid_best_results, 'En iyi GFMEAN: %.4f\n', bestGFMEAN);
fprintf(fid_best_results, 'En iyi GFSTD: %.4f\n', bestGFSTD);
fprintf(fid_best_results, 'GFSTD / GFMEAN oranı: %.4f\n', bestRatio);
fclose(fid_best_results);

% Yardımcı fonksiyonlar
function totalsec = timeToSeconds(R_time, timeParts, R_date, ampmFormat)
    % Zamanı saniye cinsine çevirme
    hour = str2double(R_time{1});
    minute = str2double(R_time{2});
    second = str2double(timeParts{1});
    day = str2double(R_date{2});

    if nargin > 3 && strcmp(ampmFormat, 'PM/AM') && strcmp(timeParts{2},
'PM') && hour < 12
        hour = hour + 12;
    elseif strcmp(timeParts{2}, 'AM') && hour == 12
        hour = 0;
    end

    totalsec = hour*3600 + minute*60 + second + day*86400;
end

function [Xlist, Ylist] = loadData(files, sortedFiles)
    % Verileri sırayla yükler ve birleştirir
    Xlist = [];
    Ylist = [];
    for i = 1:length(sortedFiles)
```

```
        fid = fopen([sortedFiles{i}, '.txt']);
        data = textscan(fid, '%f %f', 'Delimiter', '\n',
'MultipleDelimsAsOne', true);
        fclose(fid);

        if i == 1
            Xlist = data{1};
            Ylist = data{2};
        else
            deltaTime = Xlist(end) + (Xlist(end) - Xlist(end-1));
            Xlist = [Xlist; data{1} + deltaTime];
            Ylist = [Ylist; data{2}];
        end
    end
end

function avg = movingAverage(data, window)
    % Verilen pencere boyutuna göre hareketli ortalama hesaplar
    avg = arrayfun(@(i) mean(data(i:i+window-1)), 1:window:length(data)-
window+1);
end

function [maxlist, minlist] = findPeaksAndTroughs(data)
    % Tepe ve dip noktalarını bulma
    signChange = sign(diff(data));
    maxlist = data(find(signChange(1:end-1) == 1 & signChange(2:end) == -
1));
    minlist = data(find(signChange(1:end-1) == -1 & signChange(2:end) ==
1));
end

function gaugeFactor = calculateGaugeFactor(maxlist, minlist,
initialValue, strain)
    % Gauge faktörünü hesaplar
    numPeaks = min(length(maxlist), length(minlist));
    gaugeFactor = (maxlist(1:numPeaks) - minlist(1:numPeaks)) /
(initialValue * strain);
end
```

CURRICULUM VITAE

Name Surname **:** Kıvanç ÖZIŞIK

EDUCATION **:**

- **B.Sc.** **:** 2008 – 2010, Istanbul Technical University, Faculty of Aeronautics and Astronautics, Meteorology Engineering

  (Continued via Internal Transfer)

- **B.Sc.** **:** 2016, Istanbul Technical University, Faculty of Aeronautics and Astronautics, Aeronautical Engineering

PROFESSIONAL EXPERIENCE AND REWARDS:

- 12/2023 – 05/2024 : Customer Support Project Leader Aero Norway AS, Sola/Norway
- 10/2022 – 11/2023: Powerplant Senior Engineer Pegasus Airlines, İstanbul/Türkiye
- 10/2019 – 10/2022: Powerplant Engineer Pegasus Airlines, İstanbul/Türkiye
- 10/2017 – 10/2019: Powerplant Supply Engineer Nordwind Airlines, Antalya/Türkiye
- 01/2016 – 05/2017: Research Scholar ITU Aerospace Research Center, Istanbul/Türkiye

PUBLICATIONS, PRESENTATIONS AND PATENTS ON THE THESIS:

- **Ozisik, K.,** Arslan, D., Yildiz, K., Guner, H., Ozden-Yenigun, E., Cebeci, H. 2023: Graphene conductive inks for an effective textile based respiratory sensor system. 2nd International Graduate Research Symposium- IGRS'23, May 16-18, 2023, Istanbul, Turkiye.